Microglia change at the micro- and nano-scopic scales in response to therapeutic focused ultrasound blood-brain barrier modulation

by

Elisa Gonçalves de Andrade
B.Sc., Universidade Federal de Minas Gerais, 2020

A Thesis Submitted in Partial Fulfillment
of the Requirements for the Degree of

MASTER OF SCIENCE

in the Division of Medical Sciences (Neuroscience)

©Elisa Gonçalves de Andrade 2023
University of Victoria

All rights reserved. This dissertation may not be reproduced in whole or in part,
by photocopy or other means, without the permission of the author.

We acknowledge and respect the lək̓ʷəŋən peoples on whose traditional territory the university stands and the Songhees, Esquimalt and W̱SÁNEĆ peoples whose historical relationships with the land continue to this day.

Supervisory Committee

Microglia change at the micro- and nano-scopic scales in response to therapeutic focused ultrasound blood-brain barrier modulation

by

Elisa Gonçalves de Andrade
B.Sc., Universidade Federal de Minas Gerais, 2020

Supervisory Committee

Dr. Marie-Ève Tremblay, Supervisor
Division of Medical Sciences

Dr. Leigh Anne Swayne, Departmental Member
Division of Medical Sciences

Dr. Isabelle Aubert, Outside Member
University of Toronto

Abstract

Transcranial focused ultrasound sonication in combination with intravenously injected microbubbles (FUS+MB) has the unique ability to modulate blood-brain barrier (BBB) permeability with high spatial precision and in a minimally invasive manner. This process induces endothelial mechanical stress and the transient infiltration of blood-derived molecules, collectively triggering an acute inflammation in the targeted region. As the resident immune cells of the central nervous system (CNS), microglia are at the forefront of the acute inflammatory response triggered by FUS+MB BBB modulation. Notably, in inflammatory and non-inflammatory contexts, microglia are highly dynamic and continuously survey the brain parenchyma by extending their processes and interacting with surrounding elements, such as synapses and blood vessels. In response to stressors, microglia rapidly alter their cellular and molecular profile to help facilitate the return to homeostasis. While the underlying mechanisms by which FUS+MB alters microglial function remain largely unknown, several studies in adult mouse models of Alzheimer's disease pathology have reported changes in the gene expression of microglia, e.g. ionized calcium binding adaptor molecule 1 (Iba1), and in their phagocytic activity, e.g. increased uptake of the toxic protein amyloid beta, in several CNS areas, including the hippocampus where emotional, cognitive and memory processing takes place. Characterizing the baseline responses of microglia to FUS+MB in healthy models is, however, still required to understand possible outcomes of this technology in physiological processes such as microglial parenchymal surveillance, maintenance of the BBB and synaptic plasticity. To address this need, I provide the first cellular (i.e., density, distribution, and morphology) and subcellular (i.e., ultrastructure) description of microglial changes at 1 hour and 24 hours after magnetic resonance imaging-guided focused ultrasound sonication with microbubbles (MRIgFUS) targeting the

ipsilateral (ipsi-) ventral hippocampus of adult male mice. Using brightfield imaging of a double immunoperoxidase staining for immunoglobulin G and Iba1, I show that MRIgFUS causes the entering of IgG into the ipsi- *Cornu ammonis 1* (*CA1*) parenchyma at 1 hour and 24 hours, where it correlates with the proximity between Iba1 positive (+) cells. Moreover, I found that specific states within the ipsi- microglial *CA1 stratum lacunosum moleculare* (*LMol*) population are more responsive to MRIgFUS compared to the contra- *LMol*, adjusting their soma, cell body and arborization parameters to a rod-like shape, while collectively, most *LMol* microglia adopt an elongated soma shape after MRIgFUS. Notably, I observed that the *LMol* nanoscale structure of microglia changes at 1 hour and 24 hours after MRIgFUS, increasing their interactions with the BBB in vessels with bigger areas and presenting swollen astrocytic endfeet. By contrast, MRIgFUS induces less frequent interactions between microglia, pre-synaptic elements and extracellular space, associated with trogocytosis or nibbling of synaptic elements. Collectively, my research suggests that, at 1 hour and 24 hours after MRIgFUS, ventral hippocampal modifications are mostly restricted to a microglia subset, warranting further mechanistic investigations but simultaneously supporting the overall application of this technology.

Table of Contents

List of Figures

List of Tables

List of Abbreviations

+: Positive

3DEM: Three-dimensional electron microscopy

a.u.: Arbitrary unit

Aß: Amyloid beta

AD: Alzheimer's disease

AQP4: Aquaporin 4

ATP: Adenosine triphosphate

BBB: Blood-brain barrier

BM: Basement membrane

CA: Cornu ammonis

CCL: Chemokine (C-C motif) ligand

CCR2: Chemokine (C-C motif) receptor

CD11B: Integrin alpha M

CD68: CD68 antigen

CNS: Central nervous system

CLDN5: Claudin 5

CX3CR1: Chemokine (C-X3-C motif) receptor 1

CXCL: Chemokine (C-X-C motif) ligand

Contra-: Contralateral

Da: Daltons

DAB: 3-3′-Diaminobenzidine

DAMPs: Damage-associated molecular pattern

DPX: Distyrene, plasticizer, and xylene

EC: Endothelial cells

ER: Endoplasmic reticulum

FDA: Food and drug administration

FUS: Focused ultrasound sonication

FUS+MB: Focused ultrasound sonication with microbubbles

h: Hours

HRP: Horseradish peroxidase

Iba1: Ionized calcium-binding adaptor molecule 1

IL: Interleukin

Igs: Immunoglobulin

IgG: Immunoglobulin G

IgM: Immunoglobulin M

Ipsi-: Ipsilateral

LMol: *Lacunosum moleculare*

LPS: Lipopolysaccharide

MRIgFUS: Magnetic resonance imaging-guided focused ultrasound sonication with microbbules

MB: Microbubbles

Milli-Q: Milli-Q water

MR: Magnetic resonance

MRI: Magnetic resonance imaging

NND: Nearest neighbour density

Or: *Oriens*

SSP1: Phosphoprotein 1

P2RY12: Purinergic receptor P2Y, G-protein coupled 12

PB: Phosphate buffer

PBS: Phosphate-buffered saline

PC: Principal component

PCA: Principal component analysis

PD: Parkinson's disease

Py: *Pyramidale*

PIEZO1: Activating piezo-type mechanosensitive ion channel component 1

PIEZO2: Activating piezo-type mechanosensitive ion channel component 2

Rad: *Radiatum*

ROI: Region of interest

RT: Room temperature

SEM: Scanning electron microscopy

S.E.M.: Standard error of the mean

TBS: Tris-buffered saline

TGFβ1: Transforming growth factor, beta 1

TNF: Tumor necrosis factor

TPSO: Translocator protein

TREM2: Triggering receptor expressed on myeloid cells

Vs: Versus

Acknowledgements

Back in December 2019, Dr. Marie-Ève Tremblay decided to give a chance to a cold email from a random Brazilian student. I am eternally grateful for this opportunity and for my peers in the Tremblay lab, who have helped me grow so much as a scientist. I am equally grateful to our collaborators, Dr. Kofoed and Dr. Aubert, without whom this project would not have been possible.

Completing this degree represents a milestone for my family and I am so proud to stand on the shoulders of fierce women like my mother, Vânia, my great-aunt Bibia and my aunt Cássia, who have taught me everything I know about perseverance and commitment. Similarly, I am beyond privileged to have the most brilliant and loving friends, Ded, Isa, Bel, Paty, Dani, Lorena, Gama, Liz, who shown me what it is like to feel unwavering support.

A lot of introspection and personal growth can happen in the chaos of research. To my therapist, Giselle, I am beyond grateful for the company along the way.

In these foreign lands, I have been extremely fortunate to find a community of incredible individuals such as Katherine, Eva, Miri, Irene, Charlotte, Ale, Jenessa, Abu, who have helped me feel welcomed and cared for.

To Lili and Michael, thank you for never letting me forget what life is really about.

Dedication

LOVE AFTER LOVE

by Derek Walcott

The time will come
when, with elation
you will greet yourself arriving
at your own door, in your own mirror
and each will smile at the other's welcome,

and say, sit here. Eat.
You will love again the stranger who was your self.
Give wine. Give bread. Give back your heart
to itself, to the stranger who has loved you

all your life, whom you ignored
for another, who knows you by heart.
Take down the love letters from the bookshelf,

the photographs, the desperate notes,
peel your own image from the mirror.
Sit. Feast on your life.

I dedicate this work to a little girl I once knew,
to the girl I see in the mirror.

CHAPTER 1: GENERAL INTRODUCTION

I acknowledge that the following sections have been adapted from a Review manuscript which will be submitted to the journal Frontiers in Integrative Neuroscience, with consent from all co-authors: Sarina Grewal, Dr. Sophie V. Morse, Dr. Paul M. Matthews, Dr. Rikke Hahn Kofoed, Dr. Isabelle Aubert and Dr. Marie-Ève Tremblay.

1.1. Drug delivery to the brain: a longstanding challenge

Central nervous system (CNS) disorders include a wide spectrum of debilitating conditions that affect the brain and spinal cord, such as brain tumors, ischemic stroke, epilepsy, and neurodegenerative diseases (Feigin et al., 2020). The latter are characterized notably by a progressive degeneration of neurons, which leads to impairment in movement and cognitive functions (Wilson et al., 2023). The most prevalent of these neurodegenerative conditions is Alzheimer's disease (AD), a common form of dementia caused by an accumulation of toxic misfolded proteins, resulting in inflammation and degeneration of neuronal networks (Lane et al., 2018). The incidence of AD and other dementias increases with age, and it is estimated that the number of individuals worldwide currently affected by this condition is approximately 50 million (Nichols et al., 2022). Significantly, this number is set to rise to 152 million by 2050 — causing a severe burden on individuals and society (Nichols et al., 2022). Developing effective therapies to treat or prevent the onset of dementia and other neurodegenerative diseases remains an obstacle, amplified by the existence of the blood-brain barrier (BBB).

1.1.1. The blood-brain barrier

The BBB is a pivotal structure that maintains CNS homeostasis by regulating the efflux of cells and large molecules into the brain parenchyma and limiting the influx of toxins and pathogens

(Segarra et al., 2021). The BBB regulates the extracellular brain environment, for example, maintaining optimal CNS levels of ions such as Na^+, K^+, Ca^{2+}, Cl^- through efflux and influx transporters, which are key to homeostasis and maintaining health (Wu et al., 2023). The evolution of a protective neuronal-blood barrier occurred following the centralization of the nervous system in invertebrates (Pivoriūnas & Verkhratsky, 2021).

In mammals, the BBB is maintained by the cells of the neurovascular unit, comprised of endothelial cells, basement membrane, pericytes, perivascular macrophages, astrocytic endfeet and microglia (Figure 1), which collectively interact with other types of glial cells and neurons to regulate physiological functions, such as brain metabolism and cerebral blood flow. These cells also limit the passage of therapeutic compounds over 400 daltons (Da) in molecular mass and according to their number of hydrogen bonds, lipid solubility, surface and polar area, significantly hampering the treatment of numerous neurological conditions (Pardridge, 2005; Kadry et al., 2020).

The BBB creates a strict seal through binding of tight junction proteins in endothelial cells at the cerebral capillaries, restricting the extravasation of blood-borne molecules into the brain (Engelhardt, 2003). Surrounding endothelial cells are pericytes that provide structural support by releasing signalling molecules such as vascular endothelial growth factor and transforming growth factor-β, which contribute to the stability of tight junctions (Armulik et al., 2010). The basement membrane is a form of extracellular matrix consisting of various glycoproteins, including laminins and collagen type IV, which regulate the movement of cells and molecules and promotes the structural stability of the endothelial tissue (Leclech et al., 2020). Astrocytes are the most abundant glial cells in the CNS and provide structural support by tightly covering pericytes and endothelial cells with their endfeet (Abbott et al., 2006). Apart

from their structural role, astrocytes aid neuronal function by monitoring neurotransmitter release, reducing glutamate excitotoxicity and metabolizing glucose into lactate which can be shuttled to neurons for their metabolic needs. Astrocytic endfeet express aquaporin 4 water channels that regulate the osmotic balance and glymphatic functions in the CNS, as well as amyloid β (Aβ) clearance in AD (Abbott et al., 2006; Pivoriūnas & Verkhratsky, 2021).

Furthermore, the BBB is protected by microglia, the resident innate immune cells of the brain. These cells play a pivotal role in supporting brain health by surveying the environment (Nimmerjahn et al., 2005; Šimončičová et al., 2022). In response to injury or disease, microglia change, for instance, their distribution, structure and function to participate in the immune response through phagocytosis and release of soluble factors such as cytokines, chemokine and neurotrophic factors (Paolicelli et al., 2022; Šimončičová et al., 2022; Tremblay et al., 2011). However, recent advances in genome-wide association studies have reported the association of microglial genes in the pathogenesis of various neurodegenerative, neurodevelopmental and neuropsychiatric diseases (Efthymiou & Goate, 2017; Šimončičová et al., 2022). These studies have highlighted the diverse involvement of microglia in CNS disorders, making them a therapeutic target for prevention or treatment (Efthymiou & Goate, 2017; Šimončičová et al., 2022).

1.1.2. Microglia: the shapeshifters of the central nervous system

Microglia are the primary CNS immune responders. Originating in the embryonic yolk sac, microglia enter the brain in the early stage of embryonic development, where they use local cues to state differentiate and maintain their population by self-renewal (Prinz et al., 2021). This distinguishes them from structurally and functionally similar peripheral monocyte-derived

macrophages, which arise in the fetal liver and later in the postnatal bone marrow (Prinz et al., 2021).

Initial studies in the microglial field saw changes in the homeostatic inflammatory activity of microglia, commonly known as 'microglial activation', as largely detrimental. This perspective positioned microglia at the center of pathological inflammation, neurodegeneration, synaptic loss, demyelination, and vascular pathology across diseases (Sierra et al., 2019; Tay et al., 2018). Discoveries since 2005, however, have shed light onto the beneficial roles of microglia including dynamic brain surveillance, control of the neuronal population, for example, neurogenesis, synaptic remodeling, neuronal excitability regulation, regulation of vascularization, BBB formation and maintenance, as well as glial support (Figure 1).

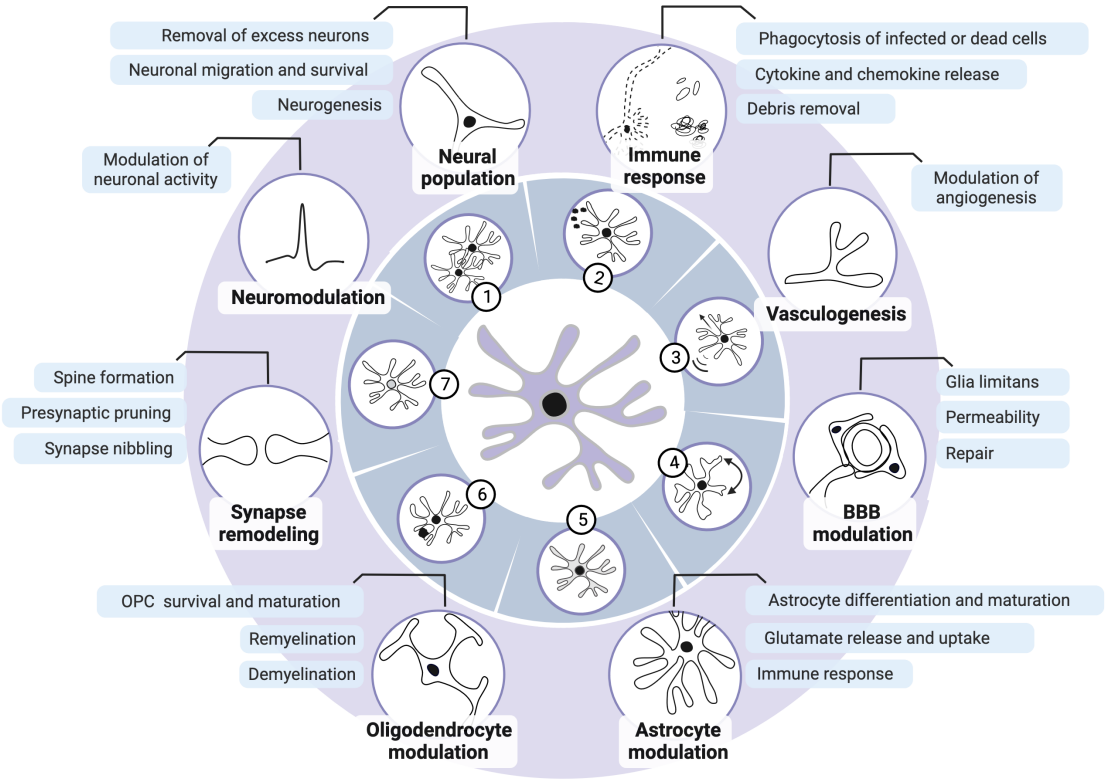

Figure 1. Microglia are crucial for brain function.

Microglia fulfill a broad range of activities in both health and disease. According to local microenvironmental cues, microglia can (1) proliferate, (2) secrete soluble factors, (3) migrate, or (4) adapt their morphology, (5) metabolism, (6) phagocytic activity, (7) transcriptome, and (8) proteome (middle ring). During brain development, microglia stimulate neurogenesis and blood vessel formation, remove excess neurons and endothelial cells and fill gaps in astrocytic endfeet coverage. Postnatally, microglia actively regulate BBB permeability and repair, as well as frequently crosstalk with astrocytes to stimulate their development and immune responses. Moreover, microglia are needed for oligodendrocyte progenitor cell (OPC) survival and maturation, myelination and myelin turnover throughout life. Synaptic remodeling is achieved via microglial (1) partial (*i.e.,* trogocytosis), or (2) full (*i.e.*, phagocytosis) pruning, in addition of (3) displacement of synaptic elements (*i.e.,* stripping) and (4) formation of dendritic spines *via* the release of neurotrophic factors, which also regulate neuronal activity and excitability. Neurons can also instruct microglia to remodel the extracellular matrix to promote synaptic plasticity. Microglia coordinate peripheral immune cell infiltration and clear parenchymal debris, apoptotic or infected cells. These responsibilities are shared with neurons, astrocytes, oligodendrocytes and border-associated macrophages, as required for homeostasis. Adapted from Šimončičová *et al.,* 2022. Agreement number: EO25QMGRE3.

Current perspectives on the field posit microglia as a spectrum of phenotypic states that coexist in the CNS (Paolicelli et al., 2022; Šimončičová et al., 2022). These states vary in overlapping transcriptome, proteome, metabolome, ultrastructure, morphology, distribution and number, notably in relation to the species, sex, age, location, lifestyle and exposure to immune challenges such as infection, trauma or stress (Paolicelli et al., 2022; Šimončičová et al., 2022; Stratoulias et al., 2019). Of note, a predominant focus on some of these contextual agents in the field makes our understanding of microglia limited. This is the case with the predominance of studies with males, which, albeit informative, may mask female-specific traits that are highly relevant in conditions such as AD (Bordeleau et al., 2019). Examples of microglial states include but are not restricted to disease-associated microglia, prevalent after neurodegeneration, and

capillary-associated microglia, which are fundamental to vascular health (Bisht et al., 2021; Deczkowska et al., 2018). Such context-dependent existence can make the activity of microglia mysterious. Detailed characterizations of these cells can aid in determining not only strategies to prevent and/or revert aberrant microglial functions, but also promote beneficial ones (Šimončičová et al., 2022). However, current microglial therapeutic modulation is challenged by limited access to the CNS due to BBB, which brings us to the discussion of interventions that can modulate BBB permeability, as outlined next.

1.2. Therapeutic implications of the blood-brain barrier

The BBB offers protection of brain cells, but at the cost of limited access for intravenous treatments. The BBB has previously been overcome in clinical settings through invasive intracranial injections requiring brain surgery or intravenous injections of high dosages of therapeutics and hyperosmotic solutions, with risks of side-effects (Castle et al., 2020; Gerstenblith et al., 2012; Mendell et al., 2017). In 2001, Hynynen *et al.* demonstrated that the BBB permeability can be increased temporarily by combining focused ultrasound sonication (FUS) with intravenously injected microbubbles (MB) (FUS+MB) (Hynynen et al., 2001). Prior to this, MB-based contrast agents were typically used in ultrasound imaging because they get trapped in blood vessels and increase echogenicity. MB contain a protein or lipid shell and a stabilized, inert gas core and are usually below 10 μm in size. Upon interaction with focused ultrasound waves, MB expand and contract, a process known as cavitation, which causes shear stress on the BBB and increases its permeability (Cammalleri et al., 2020). Since its inception, the safety of FUS+MB-mediated BBB modulation has been confirmed in clinical trials with application in a volume of up to 21 cm^3 of the human brain (Lipsman et al., 2018; Mainprize et al., 2019; Park et al., 2021).

As opposed to intracranial injections, where each injection causes tissue damage along the needle track, FUS+MB can be applied to multiple brain regions in rodents and humans without affecting adjacent areas, and hereby has the potential to confer a more widespread yet selective delivery of therapeutics blood-derived molecules (Kofoed et al., 2022; Park et al., 2021). Preclinically, FUS+MB has demonstrated the ability to increase the permeability of several barriers between the blood and the CNS and enabled delivery of therapeutics to the brain (notably with tumors), spinal cord and retina. The range of therapeutics that have been delivered to the rodent brain with FUS+MB is wide and includes small molecule drugs, recombinant proteins, nanoparticles, viral vectors and stem cells, for the treatment of a broad spectrum of animal models of neurological pathologies such as AD, Parkinson's disease (PD), Huntington's disease, spinal cord injury, and glioblastoma (Burgess et al., 2014; Chang et al., 2017; Jordão et al., 2010; Kofoed et al., 2022; Mead et al., 2017; Song et al., 2017; Xhima et al., 2021). Encouraging results in animal models have pushed various clinical trials investigating the feasibility and safety of FUS+MB in individuals with brain tumors, AD and amyotrophic lateral sclerosis (Abrahao et al., 2019; Lipsman et al., 2018; Mainprize et al., 2019; Meng et al., 2021).

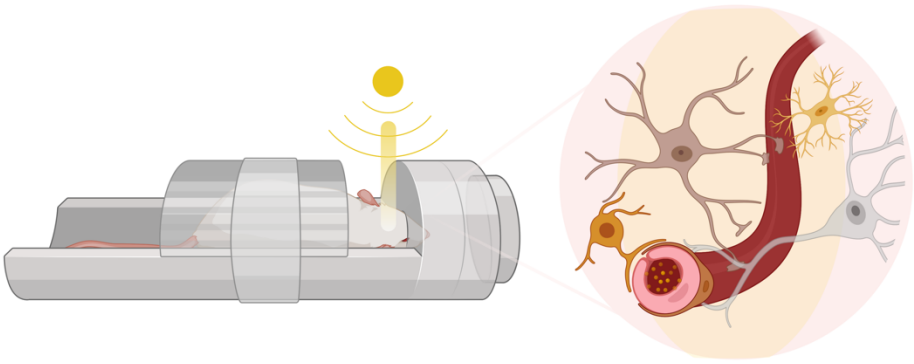

Figure 2. Focused ultrasound sonication with microbubbles modulates the blood-brain barrier.

Schematic representation of mice exposed to magnetic resonance imaging-guided focused ultrasound sonication with microbubbles (yellow shade). The blood-brain barrier within the neurovascular unit is depicted as follows: blood vessel – red, endothelial cell – pink, pericyte – dark brown, astrocytic endfeet – light brown, perivascular macrophages – orange, microglia – yellow, neuron – grey. Created with BioRender.com. Agreement number: BN25QMGYCP.

1.2.1. A brief history of ultrasound applications

In the late 19th century, Paul-Jacques Curie and Pierre Curie uncovered the piezoelectric phenomenon. This led to the development of the piezoelectric transducer that can convert electrical signals into mechanical vibration, i.e., inverse piezoelectric effect, which generates pressure waves above the audible frequency (>20 kHz), also known as ultrasound waves (Krishna et al., 2018). Significant development in ultrasound technologies during the World War II pushed the therapeutic use of ultrasound forward, with the first demonstration of thermal ablation induction of mouse liver tissue (Lynn et al., 1942; Yoo et al., 2018). Later, Fry *et al.*, (1958) documented the neuromodulatory potential of high-intensity ultrasound, which led to the reversible inhibition of neural activity in the thalamus of cats.

In the 1980s and 1990s, technological advancements allowed ultrasound waves to be focused on a specific region without affecting the skull. The result was a focal size with a diameter and length of less than 10 mm that used ultrasound frequencies between 220–650 kHz, which are much lower than diagnostic ultrasound (1–15 MHz) (Lynn et al., 1942; Yoo et al., 2018). This technology was termed focused ultrasound sonication or FUS. It provided great advantages over other non-invasive neurological therapeutic approaches, such as transcranial magnetic stimulation and direct current stimulation, as well as more invasive therapies such as deep brain stimulation, radiation, and surgery, due its incision-less procedure using highly localised ultrasound waves that penetrate deep into tissue with a high spatial resolution (Fini &

Tyler, 2017). Remarkably, researchers observed changes in the permeability of the BBB in proximity to the regions targeted with FUS, which established the foundation for currently ongoing research into its BBB therapeutic potential (Bakay et al., 1956; Ballantine et al., 1960).

The combination of FUS transducers with magnetic resonance imaging (MRI) allowed better target visualization, temperature monitoring and tissue coagulation detection (Hynynen et al., 2001; Konofagou, 2012). As a result, it was uncovered that immediately following FUS, maximum MRI signal with the contrast agent gadolinium is observed in the brain parenchyma. This suggested that increased BBB permeability (up to 100-fold) is achieved instantly. The BBB permeability reaches its maximum at 1 hour (h), gradually decreasing at 2, 4, and 8 h after FUS+MB in adult rats (Cho et al., 2016; Jalali et al., 2010; Seng et al., 2011; Sheikov et al., 2006, 2008).

Notably, FUS+MB increases transport through both transcellular, using the luminal and abluminal membranes, and paracellular, using the intercellular spaces, BBB pathways (Vykhodtseva et al., 2008). This is achieved by a free passage through the mildly injured endothelium but also enhancement of transcytosis, endothelial cell fenestrations, channels, and a significant reduction in the expression of tight junction proteins such as claudin 5 (CLDN5), zona occludens 1 and occludin 1 at 2 h after sonication, but a return to baseline levels following 4 h (Cho et al., 2016; Jalali et al., 2010; Seng et al., 2011; Sheikov et al., 2006, 2008). The biological outcomes of FUS are influenced by four major properties: power, amplitude, frequency, and duration of exposure (Krishna et al., 2018). The input voltage to the transducer's piezoelectric material determines the power of the sound wave, which controls the amount of energy of the ultrasound beam, measured in watts (Wonhyee et al., 2021). Amplitude refers to the strength or height of the sound wave and is given in pascal (Pa) (Cammalleri et al., 2020).

Power is proportional to the square of the amplitude, so doubling the amplitude means quadruplicating the energy delivered to the tissue. FUS is typically administered in a series of pulsed sinusoidal pressure waves, where each pulse has a specific burst duration that is repeated at a certain pulse repetition frequency, represented in hertz (Hz) (Cammalleri et al., 2020). Correspondingly, the frequency of FUS is inversely proportional to the energy delivered (Krishna et al., 2018, Cammalleri et al., 2020).

1.2.2. Focused ultrasound sonication with microbubbles modulates the ultrastructure of the blood-brain barrier

Following FUS+MB, structural changes of the BBB propagate towards the neuropil in a time-dependent fashion. One minute after FUS+MB, horseradish peroxidase (HRP, 40 kDa and 5 nm) was absorbed by vesicles in the luminal front of endothelial cells in male rabbits (Hynynen et al., 2005). The number of plasma membrane invaginations, *i.e.,* caveolae, also appeared to increase immediately after FUS+MB in rats, an event associated with significantly enhanced caveolin-1 protein expression, essential to caveolae transcytosis (Deng et al., 2012). Five minutes (min) after sonication, HRP was observed in caveolae, vacuoles and vesicles within endothelial cells, basement membrane and perivascular space, indicating rapid changes in BBB transport (Hynynen et al., 2005). Arterioles exhibited a faster infiltration than venules and capillaries, with staining appearing in the neuropil 5 min post FUS+MB in adult rabbits (Sheikov et al., 2006).

However, regardless of the vessel size, in male rabbits, HRP was detected in the neuropil within 20 min and the distribution remained similar 1 h post sonication (Sheikov et al., 2006). At 1 h, extravasated red blood cells and perivascular oedema were observed in three out of eleven locations exposed to 0.8 MPa FUS+MB (Hynynen et al., 2005). Similar findings regarding the density of vesicles and extravasated red blood cells were detected in the thalamus

between 1 and 2 h following FUS+MB 1 MPa (Sheikov et al., 2004). Moreover, while at 5 min post sonication, HRP caveolae concentrated in the luminal front of endothelial cells, at 1 h, HRP-filled vesicles were now found in the abluminal surface of endothelial cells (Sheikov et al., 2006).

In the thalamus of adult male rabbits, an increased number of vesicles, vacuoles, plasmalemmal pits in endothelial cells and pericytes was observed at 1 h following 1 MPa FUS+MB (Sheikov et al., 2004). At this acoustic pressure, the endothelial membrane had folds and channels exposing the vessel lumen to the basement membrane. Moreover, some but not all vessels had visually widened tight junctions, occasionally with endogenous IgG staining. While the basement membrane did not seem structurally different compared to the control, it also presented IgG particles (Sheikov et al., 2004).

Notably, when the acoustic pressure was increased to 3 MPa, more distinct effects were found, including darkened and detached endothelial cytoplasm. Degeneration of both pericytes and astrocytes was observed, accompanied by a tortuous and irregular basement membrane that exposed the brain parenchyma. Correspondingly, IgG staining was present in much larger densities, confirming a harsher disruption of the BBB (Sheikov et al., 2004). In female rats, 1 h after FUS+MB treatment at 100 W/cm^2 the ultrastructural changes worsened in relation to the focal area, where vessels presented with swollen endothelial cells, containing swollen mitochondria, pinocytotic vesicles, and disrupted cell membrane, and swollen astrocytic endfeet with degenerating cytoplasm (Yoshino et al., 2009). Remarkably, there is no record of ultrastructural investigations of microglia following FUS+MB, which significantly limits the understanding of the biological outcomes of this technology in the BBB and CNS.

1.3. Focused ultrasound with microbubbles elevates blood-to-brain communication

From drugs of approximately 500 Da, to antibodies, of 150 kDa, and gene vectors of 4 MDa, FUS+MB-induced BBB modulation provides a powerful tool to increase the entry of molecules of various weights into the brain, in rodents (Meng et al., 2021), non-human primates (Blesa et al., 2023) and humans undergoing clinical trials (Meng et al., 2021). According to the FUS acoustic pressure, preclinically, the BBB can allow passage of molecules of varying sizes, for instance, with 2.3 to 54.4 nm diameter (Chen & Konofagou, 2014). This increased permeability persists from 6 to 8 h following FUS+MB, although blood-derived components can linger in the brain parenchyma for multiple days (Todd et al., 2019). Upon entry into the brain parenchyma, molecules distribute according to their sizes. For instance, compared to 7 kDa, the dextran of 3 kDa was found at higher concentrations and had a more uniform distribution in the hippocampus of male mice after FUS+MB (Choi et al., 2010).

This indicates that varied endogenous blood antigens have the potential to extravasate into the brain after FUS+MB, a process which merits investigation in many brain areas, including the hippocampus, the therapeutic epicenter of many conditions targeted by FUS+MB (Meng et al., 2021). The ventral hippocampus, in particular, has been repeatedly shown to reliably increase BBB permeability following FUS+MB (Meng et al., 2021). Notably, this area receives inputs from the medial band zone of the entorhinal cortex, carrying primarily olfactory, visceral, and gustatory information. The ventral hippocampus broadly impacts emotional and affective processes, with outputs to amygdala nuclei, the *nucleus accumbens* and the prefrontal cortex, which modulate motivated behavior, as well as neuroendocrine and autonomic circuitry in the hypothalamus (Fanselow & Dong, 2010).

The hippocampus is divided in two main components: the *cornu ammonis (CA)* and the dentate gyrus. The *CA* is comprised of four subfields (*CA1-4*), of which the *CA1* is of special interest (Keller et al., 2018), because of its output of the trisynaptic circuit (Fanselow & Dong, 2010; Hong & Kaang, 2022). The *CA1* is organized in four strata that have distinct neuronal compositions. Laterally to medially, the strata are distributed as follows. The *CA1 stratum oriens (Or)* is characterized by the presence of basal dendrites of pyramidal neurons that receive input from *CA2* and *CA3* pyramidal cells, septal and commissural fibers. The *CA1 stratum pyramidale (Py)* is marked by cell bodies of excitatory pyramidal neurons. *Or*, *Py* and *stratum radiatum (Rad)* contain different interneuron populations. In the *Rad*, these interneurons receive connections from septal, commissural and Schaffer collateral fibers from the *CA3* to *CA2*, which continue to project through the *stratum lacunosum*. The latter is associated with the *stratum moleculare*, hence, they are often characterized as a single layer (*LMol*: *stratum lacunosum-moleculare)*. The entorhinal cortex perforant path fibers synapse onto pyramidal cell dendrites in the *LMol,* from where there are projections to the subiculum, olfactory bulb and other primary olfactory cortical areas, relaying information regarding social or fear memory, anxiety and reward to the amygdala, the *nucleus accumbens* and prefrontal cortex (Sik et al., 1995).

In addition to neurons, microglia vary along both hippocampal subregions and layers (De Felice et al., 2022; Jinno et al., 2007; Keller et al., 2018). In the ventral hippocampal *Rad,* microglia are less dense and more ramified compared to cells within the dorsal pole, findings associated with longitudinal basal differences in synaptic plasticity, *e.g.,* reduced long-term potentiation (De Felice et al., 2022; Jinno et al., 2007; Keller et al., 2018). The vascular tree, likewise, varies within the hippocampal strata. While smaller vessels, such as capillaries, guarantee blood supply to the entire hippocampus, large vessels such as the internal transverse

hippocampal vein and external transverse hippocampal artery are adjacent to the *CA1 LMol* and *Rad* (Choi et al., 2010).

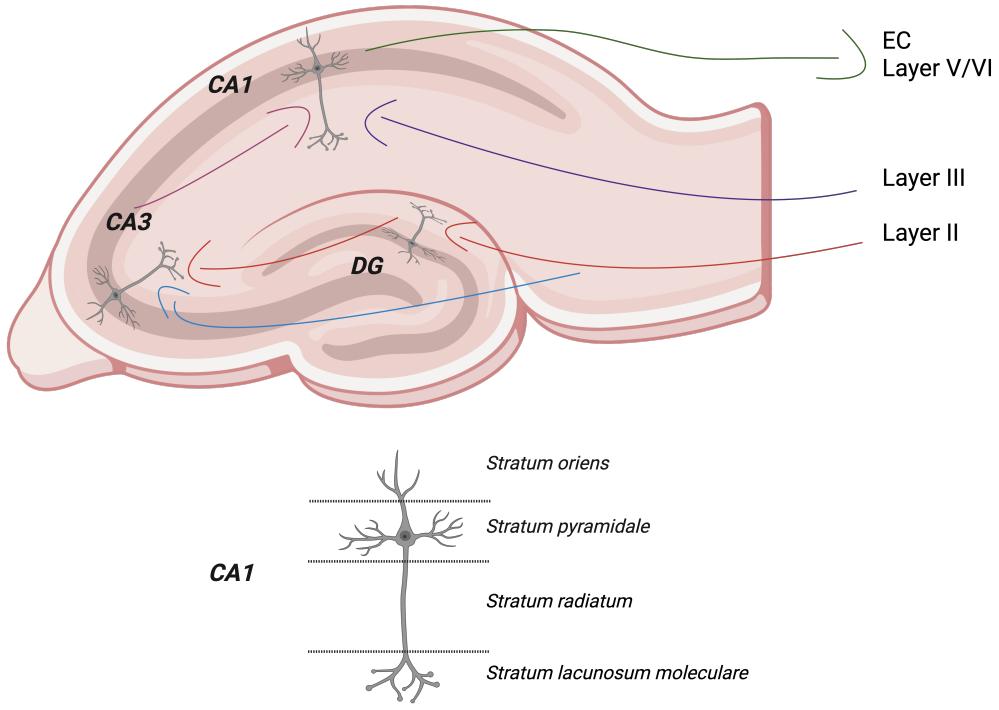

Figure 3. The *Cornu ammonis 1* is an important region in the hippocampal trisynaptic circuit.

Information flows from the entorhinal cortex to the dentate gyrus (perforant path), then to the *CA3* region (mossy fibers), and finally to the *CA1* (Schaffer collaterals), specifically the *stratum radiatum*. From the *CA1 stratum pyramidale,* output pathways are projected to many cortical areas, including the entorhinal cortex and subiculum, where they are further processed, stored and retrieved (Stepan et al., 2015). Created with BioRender.com. Agreement number: CE25QLZUED

1.3.1. Blood serum molecules

Albumin is the most abundant serum plasma protein and plays vital roles in the osmotic balance of the blood and transport of molecules (Kozlowski et al., 1992). Typically, albumin is blocked

by the BBB because of its size (66.5 kDa). However, upon 1 MHz FUS+MB at 0.7 MPa, albumin quickly extravasates into the brain parenchyma (Leinenga & Götz, 2015). When the whole brain of APP23 mice, an AD pathology model, was targeted using scanning ultrasound, Evans blue-conjugated albumin (67 kDa) was detected in the forebrain parenchyma as early as 30 min after sonication (Leinenga & Götz, 2015). Similarly, in male rats, targeting the cerebral cortex with 1 MHz FUS+MB at 1.25 MPa also revealed increased levels of albumin extravasation 30 min after the treatment, which despite colocalizing with microglia, persisted up to 24 h (Alonso et al., 2011). At lower acoustic pressure, 0.3 MPa, albumin was also detected at significantly higher levels compared to control in the anterior cerebral cortex of female rats 6 h after 0.5 MHz FUS+MB (Kovacs et al., 2017). Yet, this work used a concentration of MB 5 to 10 times higher than recommended, which may have contributed to increased cavitation and BBB modulation (Silburt & Aubert, 2022). In primary rat cultures, microglia respond to albumin by producing interleukin (IL)-1β (Ralay Ranaivo & Wainwright, 2010). Moreover, BV-2 cells, an immortalized cell line of microglia-like cells, incubated with a 20% of the concentration of albumin found in the serum of mice increased their uptake of co-cultured Aβ by 65%, which indicates that albumin may act as a chaperone for microglial phagocytosis (Leinenga & Götz, 2015). Correspondingly, Evans blue-conjugated albumin co-localized with ionized calcium-binding adapter molecule 1 (Iba1) positive (+) cells, representing microglia/macrophages (Alonso et al., 2011). Iba1 is a protein involved in actin reorganization and cell motility that has recently been implicated synaptogenesis and synaptic pruning during postnatal CNS development (Gonçalves de Andrade et al., 2022; Lituma et al., 2021).

In addition to albumin, another well-established extravasate of FUS+MB is immunoglobulin (Ig). Increased CNS concentration of exo- and endogenous Igs occurs in

animals treated with FUS+MB, including wild-type mice and various mouse models of AD (TgCRND8, APP/PS1 and B6C3-Tg) (Bathini et al., 2022; Dubey et al., 2020; Jordão et al., 2010, 2013; Kinoshita et al., 2006; Raymond et al., 2007, 2008). In a transgenic mouse model, with both female and male mice overexpressing the human amyloid precursor protein (*e.g.,* TgCRND8), elevated blood evasion of endogenous IgG and IgM into the parenchyma was identified from 4 h to 4 days after 0.5 MHz FUS+MB at 0.3 MPa targeting the cerebral cortex (Jordão et al., 2013). IgG was detected in higher concentrations in the treated hemisphere compared to contralateral control of TgCRND8 and wild-type mice, while IgM was only found in the treated hemisphere (Jordão et al., 2013). Although the infiltration rate of IgM is likely smaller than IgG (6 times lower molecular weight), similar co-localization of IgM and IgG with Aβ plaques after FUS+MB may be explained by greater binding avidity (Jordão et al., 2013). Similar exogenous IgG extravasation was identified in the hippocampus at 4 and 24 h post sonication, but not at 7 and 14 days, suggesting a transient presence of Igs after FUS+MB (Dubey et al., 2020).

Once in the brain, Igs are detected by signal transduction activation and inhibition receptors, Fc receptor, IgG, high affinity I, and Fc receptor, IgG, low affinity IIb, respectively (Brazil et al., 2000, Quan et al., 2009). IgG opsonization of Aβ aggregates leads to trafficking into endosomes and lysosomes in primary microglia (Bard et al., 2000; Brazil et al., 2000), however, subsequent signalling pathways are not well known. Delivery of an antibody against Aβ protein with 835 kHz FUS+MB at 0.33 MPa pulsed at 2 Hz resulted in a reduction in plaques and less synapse loss in the hippocampus of APP-PSI male mice, compared to the FUS+MB or intravenous antibody injection alone (Sun et al., 2021). It is important to note, however, that albeit a characteristic feature of the disease, recent evidence has challenged Aβ as the main

culprit of AD pathology, shedding light on the contribution of other components, including metabolism, as well as cellular stress and arrest (Lau et al., 2023).

1.3.2. The immune hypothesis

The physical stress exerted on the vascular endothelium by the oscillation of MB and the influx of molecules into the brain triggers an acute inflammatory process in the region targeted by FUS+MB. The exact pathways involved are elusive but seem to include cytokine or pattern recognition activating the canonical nuclear factor of kappa b cascade (Choi et al., 2023; Kovacs et al., 2017; McMahon et al., 2020; McMahon & Hynynen, 2017). This process is illustrated by an increased transcriptomic expression of endothelial genes related to inflammation, such as the cytokines tumor necrosis factor (*Tnf*), *Il1β* and *Il6* in male rodents (Ji et al., 2021; Kovacs et al., 2017; McMahon et al., 2020; McMahon & Hynynen, 2017). Endothelial cytokine production is thought to contribute to tissue regeneration after FUS+MB, increasing largely at 6 h but reversing to baseline 24 h after the treatment (Kovacs et al., 2017; McMahon & Hynynen, 2017).

FUS+MB also results in the endothelial and parenchymal production of chemokines, proteins associated with immune cell migration (Cartier et al., 2005; McMahon & Hynynen, 2017). BBB modulation with 1.1 MHz FUS+MB at 0.42 MPa upregulates chemokine (C-C motif) ligand (*Ccl)2, 12, 3* expression, associated with the recruitment of microglia and macrophages (Choi et al., 2022; Ransohoff & Perry, 2009). Moreover, a single treatment of 0.5 MHz FUS+MB at 0.3 MPa in young female rats increased the expression of damage-associated molecular patterns (DAMPs), resulting in an increase of chemokine (C-X-C motif) ligand (CXCL) 1 and 3 proteins which can recruit cells such as neutrophils to the site of inflammation (Kovacs et al., 2017).

1.3.3. Immune infiltration

Macrophages exhibit similar immune regulatory functions as parenchymal microglia, such as phagocytosis and cytokine secretion, but, when in the CNS, reside in the surrounding regions of the meninges, choroid plexus, peripheral and perivascular space (Lee et al., 2021). While macrophages are rare in the brain parenchyma, neuroinflammation, as observed in AD, for example, can promote infiltration to the brain (Jung & Schwartz, 2012; Muñoz-Castro et al., 2023). Previously, it has been suggested that FUS+MB can contribute to the infiltration of macrophages (Burks et al., 2011). However, to investigate this question, most studies have used markers such as Iba1, integrin alpha M (CD11B) (Liu et al., 2010) and CD68 antigen (CD68) (Kovacs et al., 2017; Pouliopoulos et al., 2021), which are present in both macrophages and microglia (Šimončičová et al., 2022). CD11B is a component of complement receptor 3 which mediates microglial pruning of axon terminals (Schafer et al., 2012), while CD68 is a protein present in secondary and tertiary lysosomes, indicative of microglial phagolysosomal activity (Lecours et al., 2020), although it can also increase in contexts of disrupted phagocytosis (Janda et al., 2018).

Notably, an *in vivo* imaging study in rats, revealed that, during and after the FUS+MB treatment, groups of cells accumulate and obstruct cortical blood vessels and more rarely transmigrate through the endothelium (Poon et al., 2021). This infiltration was primarily associated to neutrophils in a mouse model of AD pathology (TgCRND8) (Poon et al., 2021). Moreover, in a mouse model of glioma, chemokine (C-C motif) receptor 2 (CCR2)+ cells infiltrated the treated parenchyma after 2 and 3, but not one FUS+MB sessions. Flow cytometry data supported that the tumor immune microenvironment following multiple FUS+MB sessions had significantly less chemokine (C-X3-C motif) receptor 1 (CX3CR1)+ CCR2- cells, likely

microglia, but more lymphocytes, monocytes, neutrophils in both the ipsi- and contra-hemispheres compared to naïve animals (Q. Zhang et al., 2023).

Although evidence of immune infiltration in the CNS following a single FUS+MB session is inconsistent, *in vitro* studies have shown that ultrasound alone can exert anti-inflammatory effects by increasing release of *Il10* and decreasing of pro-inflammatory markers *Tnf* and *Il8* expression in human leukemia monocytic macrophages treated with the pro-inflammatory antigen, lipopolysaccharide (LPS) (Fontana et al., 2021). Additionally, macrophages differentiated from the U937 cell line treated with low-intensity ultrasound alone at 38 kHz significantly reduced pro-inflammatory cytokines by activating piezo-type mechanosensitive ion channel component 1 (PIEZO1) ion channels, (Iacoponi et al., 2023), suggesting that FUS can modulate macrophage function.

The innate immune response carried out by cells such as microglia and macrophages can be complemented by the adaptive immune response, comprised of specialised T cells that can recognise and eliminate antigens derived from pathogens, viruses, or cancer cells (Cooper & Alder, 2006). Under homeostatic conditions, T cells are rare in the brain parenchyma (Smolders et al., 2013). Previous research has demonstrated that FUS can regulate the infiltration of T cells in various models of cancer, albeit none in the CNS (Bandyopadhyay et al., 2016; Liu et al., 2012). For instance, Liu *et al.*, (2012) demonstrated that 0.5 MHz FUS+MB pulsed at 1.4MPa in CT-26 tumor cells subcutaneously injected into mice significantly reduced tumor growth by 34.4% and increased the infiltration of cytotoxic CD8+ T cells, which are normally inhibited by cancer cells, resulting in immune evasion and a challenge for anti-tumor immune responses (Schreiber et al., 2011). Overall, CNS infiltration of innate and adaptive immune cells following FUS+MB is still unclear. More established, however, is the evidence that the resident immune

cells of the brain, microglia, play a role in the acute inflammatory process resulting from FUS+MB-induced BBB modulation, as outlined next.

1.3.4. Microglia change their organization in response to focused ultrasound with microbubbles: Density and distribution evidence

The density and distribution of microglia is varied across regions, subregions and even layers in the CNS (Khakpour et al., 2022). Microglia rearrange 10–15% of their cortical distribution daily in adult mice to effectively scan their environment (Hammond et al., 2021). This reorganization is further increased in response to stressors, *e.g.,* seizures and laser injury (Eyo et al., 2018). In AD, microglia proliferate and migrate towards Aβ plaques, shielding them to prevent further spread (Hammond et al., 2021). In homeostatic and pathological conditions, changes in microglial density and distribution are stimulated by microenvironmental cues, which cause proliferation, migration and cell death (Khakpour et al., 2022). Disruption of the BBB permeability can influence the distribution of microglia, potentially impacting parenchymal surveillance. In male mice modelling systemic lupus erythematosus, cortical BBB disruption led to a decrease in the density of parenchymal Iba1+ cells, which associated with vessels and increased protein expression of CLDN5 (Haruwaka et al., 2019).

Similarly, FUS+MB can impact the organization of microglia. Following 2 days after 0.25 MHz FUS+MB treatment in the prefrontal cortex of adult non-human primates, at 0.8 MPa but not 0.4 MPa, Iba1+/CD68+ cells migrated towards blood vessels. However, in both cases, no changes in density were found 18 days post treatment (Pouliopoulos et al., 2021). Changes in microglial density were not observed in the cerebral cortex of an adult mouse model of AD pathology (TgCRND8), after 0.5 MHz FUS+MB at 0.3 MPa, regardless of the proximity to Aβ plaques (Jordão et al., 2013). By contrast, a reduction in nearest neighbour density (NND) was

observed in the treated compared to non-treated hippocampus of wild-type male mice 7 days after FUS+MB (Silburt & Aubert, 2022). NND represents the average of the distance of between each and its closest neighbor, thus, it is an indicator of the proximity between cells (González Ibanez et al., 2019). In addition, 7 weeks after 1 or 6 weekly FUS+MB treatments (0.3MPa and 0.5 MPa), the Iba1+ area increased in the cerebral cortex of female rats, as did the number CD68+ cells (Kovacs et al., 2017). Elevated microglia density after FUS was similarly observed in a mouse model of glioma (GL26) receiving two or three 0.5 MPa FUS+MB sonications (Zhang et al., 2023). Furthermore, FUS+MB delivered 9 days after immunization with recombinant myelin oligodendrocyte glycoprotein, an animal model of experimental autoimmune encephalomyelitis, was associated with increased Iba1+ and transmembrane protein 119 (TMEM119)+ foci of microglia 12 days post sonication in young female mice (Schregel et al., 2021). Notably, FUS alone does not seem to alter microglia density in the cerebellum. Both shorter-duration, 0.3 seconds (s), and longer-duration, 15 s, FUS pulses, inducing mechanical-dominated and mechanical and thermal effects, respectively, did not significantly affect the Iba1+ cell density in the cerebellum of adult female mice (Baek et al., 2018). These findings suggest that changes in the distribution and density of microglia in rodents may occur several days after one or multiple FUS+MB treatments, but evidence on earlier timepoints and at steady-state conditions is not yet available. These insights would be important to infer if FUS+MB has a short-term impact on microglial proliferation, migration and cell death, which are kept in a tight balance to support all the homeostatic functions of these cells (Khakpour et al., 2022)

1.3.5. Microglia change their shape and form after focused ultrasound with microbubbles: Morphological evidence

Microglia, as CNS surveyors, constantly shift their morphology to probe and sense their environments (Bosch & Kierdorf, 2022; Savage et al., 2019). On average, they extend and retract their processes at a rate of 1.5 μm per min in the mouse cerebral cortex (Fuhrmann et al., 2010; Nimmerjahn et al., 2005) and can increase their cell body size in rodents to enhance transcriptomic and phagocytic activities (Gonçalves de Andrade et al., 2022). Microglial morphological states exist in a spectrum and are broadly classified as: ramified (normal soma, highly branched processes), ameboid (enlarged cell soma with filopodia), hypertrophic (large soma, short and thick processes), rod-shaped (small nuclei and bipolar processes), and dystrophic (seemingly fragmented, with tortuous processes) (Savage et al., 2019; Šimončičová et al., 2022). However, it is important to note that morphological analyses, albeit informative, are not standardized across research teams (Green et al., 2022) and represent one level of complexity of microglial function that should be complemented with other analyses (Paolicelli et al., 2022).

Morphological changes enable microglia to respond to BBB disruption. Increased BBB permeability caused by systemic inflammation after LPS injection in the motor cortex led to delayed (5 to 7 days) alterations in microglia morphology that resemble capillary-associated microglia (Bisht et al., 2021), including decreased number of microglial processes and increased soma size (Haruwaka et al., 2019). Similar findings were observed in the cerebral cortex of female and male adult mice with cerebral ischemia and mannitol-induced BBB disruption. Here, reductions in process length and number were concurrent with an increased dendritic spine turnover (Ju et al., 2018), as found during developmental synapse pruning and sleep (Colombo et al., 2022; Hristovska et al., 2022).

Both FUS and FUS+MB are tied to morphological changes in microglia (Bobola et al., 2020; Silburt & Aubert, 2022), offering insights into, for example, surveillance and *glia limitans* outcomes following treatment (Savage et al., 2019). Hippocampal Iba1+ cells in wild-type male mice exhibited only minor reductions in the branch length and number of branches 7 days after FUS+MB (Silburt & Aubert, 2022). These arborization differences became more pronounced when cells were spatially organized into morphological clusters. Using an unsupervised machine learning workflow, cells were categorized based on the detection of morphological alterations between FUS+MB treated and control hemispheres (maximal, medium, no change) and grouped according to the extent of their changes (focal, proximal, and distal regions) (Silburt & Aubert, 2022).

Both focal and proximal microglia had significantly increased area and soma size, colocalizing with transforming growth factor, beta 1 (TGFβ1). The reductions in branch length and number of branches per cell were more expressive in these two clusters *versus* (*vs*) the total group of cells (Silburt & Aubert, 2022). Thus, effects of FUS+MB on hippocampal microglia are heterogenous and spatially distributed multiple days following the treatment. This could indicate that subsets of cells are more responsive to FUS+MB. When the same methodology was applied to an aged model of AD pathology (7-months-old TgCRND8 mice), focal microglia were found to overlap with Aβ plaques (Silburt & Aubert, 2022). Microglia have distinct roles in health and disease, but these findings suggest an overlapping response following FUS+MB. To establish the directionality of this relationship, it would be important to characterize the responses of microglia in steady-state conditions, at early timepoints following FUS+MB, when changes in microglial function could aid or hinder the return of BBB homeostasis. Moreover, as the integrity of the BBB is affected by sex, brain region and age, for instance, being superior in younger

females *vs* males in the human cingulate cortex (Moon et al., 2021), it follows that the context of microglia can affect the outcomes of BBB modulation after FUS+MB.

1.3.6. Microglia change their function in response to focused ultrasound with microbubbles: Phagocytic activity evidence

Microglia, the primary phagocytes in the brain, are involved in controlling the densities of other cell populations in the CNS, including astrocytes and oligodendrocyte progenitors (Nelson et al., 2017; Santos et al., 2016). Microglia notably phagocytose apoptotic neurons (Sierra et al., 2010) and synapses (Tremblay et al., 2010) during steady-state conditions. In addition to these steady-state functions, the phagocytic activity of microglia is a crucial component of inflammatory responses in the CNS, guarantying the removal of cellular debris, apoptotic and infected cells, extracellular toxins and pathogens (Šimončičová et al., 2022).

Previous research has proposed that FUS+MB can facilitate the removal of Aβ plaques through modulating the phagocytic activity of microglia. For instance, 0.5 MHz FUS+MB treatment in 4-month-old TgCRND8 mice significantly increased the colocalization of Iba1+ cells and Aβ in the treated hippocampus compared to the contra- control, an effect which was associated with decreased Aβ plaque burden (Jordão et al., 2013). This finding holds clinical importance as microglia in the advanced stages of AD lose their ability to efficiently remove Aβ (Galloway et al., 2019). Moreover, BBB modulation with 1.5 MHz FUS+MB at 0.45 MPa has reported similar effects in the co-localization of Iba1+ cells and tau, ameliorating tau pathology in the hippocampus of rTG4510 mice, another important hallmark of AD (Karakatsani et al., 2019). Enhanced BBB permeability is likely to have induced an immune response modulating the activity of microglia and promoting the clearance of tau pathology (Karakatsani et al., 2019), although further research is needed to confirm this hypothesis.

1.4. Further research directions on the impact of focused ultrasound with microbubbles on microglia:

Current findings on the responses of microglia following FUS+MB have built a sound foundation. However, many questions remain unanswered, notably with respect to the early changes following BBB permeability, which are discussed next.

1.4.1. Microglial contacts with the blood-brain barrier

Microglia communicate closely with blood vessels in the CNS (Joost et al., 2019). In the cerebral cortex of adult male mice as well as aged and middle-aged humans (female and male), they contact most of the vascular tree, for periods ranging from 5 to 15 min, and often repetitively. Here, microglial processes simultaneously touch multiple vessels and nearby neurons, connecting the entire neurovascular unit (Császár et al., 2022). Myeloid cells associated with capillaries present characteristic ultrastructural features of microglia, including clumps of chromatin beneath their nuclear envelope and throughout their nucleoplasm, in the adult mouse brain (females and males) (Bisht et al., 2021). In fact, it is estimated that ~30% of microglia cell bodies are associated with capillaries across multiple cell regions such as the cerebral cortex, thalamus, and hippocampus (Bisht et al., 2021).

In addition to capillaries, the most common type of blood vessel contacts of microglia, microglia can also be directly adjacent to veins and arteries in mice (Joost et al., 2019). 3D reconstructions of rapidly preserved human surgical samples from the temporal lobe of the cerebral cortex confirmed that most microglial cell bodies are within 5 μm of a blood vessel (Shapson-Coe et al., 2021). Császár *et al.,* (2022) showed that microglial processes, marked by the purinergic receptor P2Y, G-protein coupled 12 (P2Y12R) contact most cortical astrocytic endfeet. Microglia have been proposed to associate with the vasculature particularly in areas

lacking astrocytic endfeet during late postnatal development in mice (Mondo et al., 2020), but also in the highly vascularized hippocampal *LMol* of adult male rats (Bisht et al., 2016; Joost et al., 2019; Mathiisen et al., 2010).

Beside endfeet, P2Y12R+ processes also interact with smooth muscle actin and most pericytes in the cerebral cortex of adult male mice (Császár et al., 2022). A specific cortical subset of pericyte-associated microglia has been identified in female and male mice (Morris et al., 2023). Of note, pericytes cover proximately 1/3 of the endothelial surfaces in the *LMol* (Mathiisenet al., 2010). Strikingly, P2Y12R+ processes contacted 15% of endothelial cells in cortical blood vessels of adult female and male mice. Direct apposition of P2Y12R+ processes and endothelial mitochondria suggested that adenosine triphosphate (ATP) release attract these contacts (Császár et al., 2022). Indeed, capillary-associated microglia rely on purinergic signaling to interact with the vasculature (Bisht et al., 2021).

It is possible that after FUS+MB BBB modulation, the evasion of blood molecules from the blood into the brain and the endothelial chemokine release attracts microglia toward the BBB. Following LPS, typically associated with BBB disruption, parenchymal Iba1+ cells in the hippocampus, parietal cortex and thalamus increase their association with vessel surfaces without AQP4 (Bowyer et al., 2020). Similarly, the density of microglia within 20 µm of vessels was significantly increased 28 h after LPS treatment in the cortical grey matter in layer III of adult male mice (Erickson et al., 2023).

Once microglia are in contact with the BBB, the outcomes are variable and context-dependant. In steady-state conditions, microglia interact with the BBB to regulate blood vessel dilation and constriction (Bisht et al., 2021, Császár et al., 2022). In a mouse model of lupus, markedly presenting increased BBB permeability, microglia processes were suggested to project

through the basement membrane and to contain phagocytic inclusions with AQP4 content, which could indicate an effort to seal the leaky BBB but also engulf astrocytic endfeet (Haruwaka et al., 2019). The authors suggested that time was the determining factor in driving the opposing effects. While one day after LPS infection in healthy mice, microglia increased CLDN5; at later timepoints (7 days), *in situ* microglia elevated instead the protein expression of CD68, along with their colocalization with AQP4. This suggested a shift from adaptive to maladaptive microglia responses due to LPS-induced inflammation, bearing a possible link with BBB permeability (Haruwaka et al., 2019), although more research is required to confirm this data. Considering the transient nature of BBB modulation after FUS+MB, it is tempting to speculate that microglia-BBB interactions may remain unaffected or elicit protective responses.

1.4.2. Microglia-neuronal interactions

Although transient, the increased permeability of the BBB caused by FUS+MB is likely to impact the interactions between microglia and synaptic elements, as in other work using other models that promote BBB permeability. In the hippocampus *CA1* (*Rad* and *LMol*) of adult female and male mice, 24 h after treatment with LPS, Iba1+ processes contacted more frequently with synaptic clefts, pre-synaptic terminals and dendritic spines (Savage et al., 2019). Considering that there were no significant changes in the contact between microglia and the extracellular space after LPS, it is possible that the adaptations in microglia-synapse interactions observed in this model represent microglia separating synaptic elements, *i.e.*, synaptic stripping (Savage et al., 2019). In the adult macaque retina, engulfment of parts of neurons, was suggested to improve antigen presentation after an inflammatory insult (Goyal et al., 2023; Weinhard et al., 2018). In the hippocampus of adult healthy mouse, perivascular macrophages secrete phosphoprotein 1 (SPP1/osteopontin) which stimulated microglial phagocytosis of synapses (De

Schepper et al., 2023). This effect was exacerbated in an AD pathology mouse model (APP-NLF) (De Schepper et al., 2023), raising the intriguing possibility that inflammation can increase the crosstalk between microglia and perivascular macrophages surrounding the BBB to stimulate synaptic removal. Notably, increased microglia-synapse interactions after LPS were associated with induced sickness behavior (Savage et al., 2019). Thus, alterations in microglia-neuronal contacts after FUS+MB could contribute both to future inflammation resolution and behavioral changes.

1.4.3. Microglial intracellular environment

Electron microscopy provides rich snapshots into the responses of microglia to inflammation (Savage et al., 2018, 2019). However, to our knowledge, no study has yet accessed the nanometric outcomes of FUS or FUS+MB on these cells. During an inflammatory insult, such as the one elicited after BBB modulation, microglia undergo metabolic shifts, favoring glycolysis over oxidative phosphorylation ATP production (Šimončičová et al., 2022). This metabolic adaptation is accompanied by ultrastructural changes in microglial mitochondria to comply with higher cellular stress and reactive oxygen species production (Katoh et al., 2017). In mouse primary cultures treated with LPS, mitochondria appeared shorter and exhibited fewer branches after 2 h, although these changes were reversed at 12 h, possibly due to microtubule elongation (Katoh et al., 2017). Similarly, in a mouse model of myelin loss, ameboid Iba1+ cells in demyelinated cerebellar white matter had shorter and smaller mitochondria (Katoh et al., 2017).

Moreover, in a mouse model of AD pathology (14-months and 20-months-old, APP-PS1, male) that accumulates Aβ plaques, there were elevated ultrastructural markers of cellular stress, *e.g.,* dilated ER/Golgi, altered mitochondria near Aß plaques and dystrophic neurites (El Hajj et al., 2019; St-Pierre et al., 2019, 2020). Ultrastructural evidence of microglial stress was

similarly detected in the hippocampus of adult female and male mice following LPS treatment (Savage et al., 2019). Notably, microglia showing ultrastructural signs of stress interacted less with the vasculature in aged male APP-PS1 mice, although it is unclear the temporal relationship between these events (St-Pierre et al., 2022). Intriguingly, human microglia co-cultured with TNF and Aβ showed autophagosome-like structures at the endpoint of their minor processes, which may increase cell surface interaction to compensate for reduced process ramification (Dyne et al., 2022). Acute inflammation induced by FUS+MB may cause similar reversible cellular stress at the ultrastructural level.

1.2.3 Manipulation of focused ultrasound with microbubble parameters reduces brain damage

Tissue damage after FUS+MB can occur through multiple mechanisms, including temperature increase, caused by the absorption of ultrasound energy, mechanical pressure, caused by cavitation, and lipid reorganization in affected membranes (Man et al., 2019). Although avoided in the context of BBB modulation via MRI monitoring, temperature increase and intense cavitation can be beneficial for treatment of disorders, such as tremors, tumors, fibroids and bone metastasis. Manipulation of FUS parameters can help prioritize cavitation *vs* heat ablation-mediated effects. Higher FUS frequencies and acoustic pressures tend to induce an increase in temperature, while lower frequencies and lower acoustic pressures are associated with cavitation. Moreover, at higher acoustic pressures, MB are more likely to collapse and can produce shock waves, as well as high-velocity jets, whereas at lower acoustic pressures, cavitation, microstreaming and acoustic radiation of MB are more probable.

1.5. FUS alone can modulate microglia

Currently, FUS alone is approved by the Food and Drug Administration (FDA) for the treatment of bilateral essential tremor, PD, prostate cancer, uterine fibroids and bone metastases (Bond et al., 2017; Elias et al., 2013; Stewart et al., 2006). Acoustic radiation forces from ultrasound waves can activate mechano-sensitive ion channels and induce ruffling of the plasma and internal membranes, impacting cell function (Yoo et al., 2018). Accordingly, FUS alone activates *in vitro* rodent primary hippocampal and cortical Ca^{2+} and Na^{2+} mechano-sensitive channels, causing an influx of extracellular Ca^{2+}, which aids in transmitting depolarization (Blackmore et al., 2023). Notably, high-intensity FUS alone elicited action potentials in skin peripheral nerves via stimulation of piezo-type mechanosensitive ion channel component 2 (PIEZO2) in female mice (Hoffman et al., 2022). Moreover, FUS directed to the somatosensory cortex of healthy adult volunteers, predominantly males, resulted in transient tactile sensations and sonication-specific evoked potentials (Lee et al., 2015). Clinical trials have also reported the efficacy of FUS as a neuromodulation tool for the treatment of epilepsy and neuropathic pain in adult females and males with temporal lobe epilepsy or chronic and therapy resistant neuropathic pain (Stern et al., 2021; Gallay et al., 2023).

Microglia express multiple mechano-sensitive ion channels and are likely to be affected by FUS acoustic radiation (Blackmore et al., 2023). Activation of the mechano-sensitive Ca^{2+} channel PIEZO1 in microglia increased the number of Iba1+ cells and their co-localization with Aβ plaques in the hippocampus of adult male mice modelling AD pathology (5xFAD) (Jäntti et al., 2022). Intriguingly, in the hippocampus of male 5XFAD mice acutely treated with 2 MHz FUS alone, an increased co-localization of Iba1+ cells with Aβ plaques has been observed, associated with nearly 50% of plaque clearance (Bobola et al., 2020). Altogether, variations in

the FUS parameters used, with or without microbubbles, provide exciting opportunities for personalised therapeutic applications targeting microglia. However, many questions remain, particularly comparing how different microenvironments based on sex, region and age affect the response of microglia to FUS. Within the context of FUS+MB, the specific effects of BBB permeability *vs* acoustic force are poorly understood, however, it is possible that both mechanisms act in concert to modulate microglial function.

1.6. Project questions and objectives

The BBB serves a protective role for the CNS, shielding the parenchyma from possible harm and maintaining homeostatic levels of nutrients, ions, and cell waste. From an extensive review of the literature, it is evident that FUS+MB can modulate BBB permeability and temporarily alter this structure. As a result, the local parenchyma is invaded by antigens, antibodies and molecules signalling mechanical and inflammatory stress, which likely involves microglia. These cells are primarily equipped to scan and remove antigens, infected and apoptotic cells and return the balance of the brain microenvironment. Following the molecules that infiltrate the brain, microglia may immediately approach affected blood vessels, altering their morphology and distribution. This would entail increasing cellular stress and shifting interactions with the neuropil and blood vessels. Failure to complete such changes could hinder the resolution of the acute inflammatory process and diminish the beneficial effects of BBB modulation, such as increased neurogenesis. However, current studies have yet to capture a detailed view of the early changes in microglia following FUS+MB, particularly in steady-state conditions and at earlier timepoints, such as 1 h after FUS+MB when there is a peak in BBB permeability and at the 24 h mark, a short period following BBB restoration. Moreover, many studies solely rely on gene expression to infer “activation” of microglia. While this data provides a solid foundation upon

which to build on, detailed density, distribution, morphology and ultrastructure analyses can provide a much more powerful characterization of the microglial responses following FUS+MB. Establishing baseline changes in microglial number, shape and form early after FUS+MB in steady-state conditions would aid in understanding how this technology can be used to modulate the surveillant and phagocytic activity of microglia toward disease resolution, for example. Given this gap in the literature, this thesis addressed the following 3 research questions:

Research question #1: Are there changes in adult male mice ventral *CA1* microglial density and distribution 1 and 24 h following FUS+MB? If so, do they correlate with IgG permeability?

Hypothesis #1: Parenchymal microglial density and distribution will not be changed in the ventral *CA1* 1 and 24 h after MRI guided FUS+MB. However, shifts in microglial distribution and numbers will strongly correlate with IgG staining, suggesting that cells sense increased BBB permeability.

Experimental approach and rationale for research question #1: First, in collaboration with the Aubert Lab, I targeted the ipsilateral ventral hippocampus of adult male mice with MRI guided FUS+MB. Next, I assisted in animal perfusion and brain cutting. I selected ventral hippocampus brain sections and processed them for double immunohistochemistry targeting Iba1 and IgG. After imaging using brightfield microscopy, I confirmed increased BBB permeability *via* increased average voxel intensity and IgG staining in ipsi- hippocampus. To contend for microglia regional diversity, I manually counted Iba1+ cells in each *CA1* layer and calculated their density, nearest neighbour distance, cluster density and spacing index. I then compared contra- and ipsi- hemispheres to establish whether there were FUS+MB related differences. Further comparisons of 1 and 24 h timepoints allowed to

investigate if putative changes in density and distribution were time dependent. Moreover, I correlated the values obtained with the IgG staining, measured *via* optical density, and microglial density and distribution to infer a possible connection between microglial changes and IgG staining.

Research question #2: Are there changes in adult male mice ventral *CA1* microglial morphology averages and distribution 1 and 24 h following FUS+MB? If so, do they correlate with IgG staining?

Hypothesis #2: Microglial soma, cell and arborization shape descriptors will indicate a shift toward rounder, less ramified morphological states in the ventral *LMol* 1 h after MRI guided FUS+MB but not at 24 h. This increase will be strongly correlated with IgG staining and diverge ipsi- and contra- morphological datasets.

Experimental approach and rationale for research question #2: I used the brightfield images obtained in the first aim to randomly select Iba1+ cells for the morphology analysis. I performed the following steps for each cell. First, I manually traced the soma and measured several shape descriptors (area, perimeter, aspect ratio, circularity, roundness and solidity). Next, I traced the process endpoints to create a convex shape that represents the overall territory of each cell and collected the aforementioned shape descriptors. Using a semi-automated approach, I obtained a mask that models the cell and retrieved, again, the same shape descriptors, along with fractal patterns. Lastly, I created an arbor based on the previous mask and attained descriptors relevant to cell ramification. I analyzed the average value of each parameter and its relative distribution across ipsi- *vs* contra- *LMol* to establish whether there were FUS+MB related differences. Further comparisons of 1 and 24 h timepoints allowed me to investigate if putative changes in morphology were immediate and resolved within 24 h.

Moreover, I correlated the values obtained with the IgG staining, measured *via* optical density, and microglia morphology to infer a possible relationship between IgG staining and microglial changes. Finally, I carried out a principal component analysis to verify if specific morphological parameters explained the segregation between ipsi- *vs* contra- *LMol.*

Research question #3: Are there changes in the average number and distribution of blood vessel and neuropil contacts, and intracellular organelles of microglia in the adult male mice ventral *CA1* 1 and 24 h following FUS+MB? If so, do they correlate with blood vessel proximity or area?

Hypothesis #3: Microglial contacts with the BBB and synaptic elements will be increased, as well as intracellular organelles associated with cellular stress in the ventral *LMol* 1 h after MRI guided FUS+MB but not at 24 h. This increase will be correlated with blood vessel proximity and segregate ipsi- from contra- ultrastructural datasets.

Experimental approach and rationale for research question #3: First, I selected ventral hippocampus brain sections and processed them for double immunohistochemistry targeting Iba1 and IgG. Next, I prepared the samples for electron microscopy using an osmium-thiocarbohydrazide-osmium protocol which improves contrast and membrane preservation. I excised the *LMol* and prepared resin blocks for ultramicrotomy. Subsequently, I assisted in the ultramicrotomy and scanning electron microscopy imaging. Moreover, I performed a blinded analysis assessing the microglial contacts with the BBB, neuronal elements and intracellular organelles. I analyzed the average value of each parameter and its relative distribution across ipsi- *vs* contra- *LMol* to establish whether there were FUS+MB related differences. Further comparisons of 1 and 24 h timepoints allowed me to understand if changes in ultrastructure were immediate but resolved within 24 h. Moreover, I correlated the values obtained with blood vessel

size and distance to infer if there was a relationship between vessel proximity and microglial ultrastructure. Finally, I carried out a principal component analysis to verify if specific ultrastructural parameters were more implicated in the segregation between ipsi- *vs* contra-*LMol.*

CHAPTER 2: MATERIALS AND METHODS

2.1. Animals and ethics

Male (n = 6 animals) C57BL/6J mice, 3 months of age, were purchased from the Jackson Laboratory. We opted to start with males to allow more comparisons with the current literature and due to technical limitations, but future studies investigating female cohorts are highly encouraged. The animals were group housed at 18-22 °C, 40-60% humidity and a 12 h light/dark cycle with *ad libitum* access to food and water. Ethical approval was obtained for all the animal experiments from the Sunnybrook Research Institute Animal Care Committee and conducted according to the Canadian Council on Animal Care Policies & Guidelines and the Animals for Research Act of Ontario.

2.2. Magnetic resonance imaging-guided focused ultrasound sonication with microbubbles

I acknowledge the contributions of Dr. Rikke Hahn Kofoed, from the Aubert Lab, who carried out the magnetic resonance imaging-guided focused ultrasound sonication (MRIgFUS) treatment in the following section:

The mice were anaesthetized using isoflurane maintained 2–3% for 30 min (CP0406V2, Fresenius Kabi, Toronto, Canada). Each mouse had its head shaved and an angiocatheter inserted into the tail vein. Mice were next placed in a supine position on an MRI-compatible sled. The sled was inserted in a 7.0 T MRI (BioSpin 7030, Bruker, Massachusetts, United States of America [USA]) to obtain T1- and T2-weighted scans. T2-weighted scans were used as anatomical references for targeting the ultrasound. The ventral hippocampus in the left hemisphere (ipsi-) was targeted by a single focus beam, while the right hemisphere (contra-) was not targeted by any and used as the control. An in-house developed prototype for LP-100 (FUS

Instruments Inc., Toronto, Canada) was used. The ultrasound waves were generated by a 0.58 MHz spherically focused transducer (75 mm outer diameter, 26 mm inner diameter, 60 mm radius of curvature) driven at the 3rd harmonic (1.78 MHz). Focused ultrasound was applied for 120 s in 0.001 s bursts at a frequency of 1 Hz, while 0.02 mL/kg Definity® MB (Lantheus Medical Imaging, Massachusetts, USA) were injected through the angiocatheter. Definity® MB are lipid-coated, polydisperse (mean diameter 1.1 to 3.3 μm) MB formed by a self-assembled monolayer. The acoustic pressure was increased incrementally after each burst. Once the signals scattered from the MB were at half the transmitted frequency (subharmonic emissions), the acoustic pressure was reduced to 50% and this level was maintained throughout the ultrasound treatment (O'Reilly & Hynynen, 2012). Subharmonic emissions were detected by a 4.8 mm diameter wideband polyvinylidene fluoride hydrophone in the transducer and analyzed as described previously (McMahon et al., 2020). Upon detection of subharmonic emissions or MB cavitation (De Santis et al., 2005), 0.2 mL/kg gadodiamide diluted in water (0.1 mmol/kg, 573.66 Da) MRI contrast agent (Omniscan, GE Healthcare Canada, Ontario, Canada) was administered *via* the angiocatheter. This was immediately followed by T1-weighted scans to visualize BBB permeability. Herein, I use MRIgFUS to refer to the magnetic resonance imaging-guided focused ultrasound sonication with microbubbles approach we utilized.

BBB permeability was quantified using Medical Image and Processing, Analysis and Visualization software (V11.0.17 for Mac OS X 10.7, MIPAV, National Institutes of Health, Maryland, USA) and regional-based analysis as previously described (Xhima et al., 2021). Briefly, a 1×1 mm^2 square, the theoretical size of the focused ultrasound spot, was used to measure the average voxel intensity in each ipsi- targeted and corresponding non-targeted contra-

brain region (Xhima et al., 2021). This average is obtained by adding the intensity of all voxels in the square and dividing the result by the sum of the voxels.

2.3. Perfusion and tissue sectioning

I acknowledge the contributions of Dr. Katherine Picard, from the Tremblay Lab, who carried out the perfusion and assisted in brain cutting in the following section:

To evaluate the short-term temporal microglia responses during and shortly after the interval of increased BBB permeability, 1 and 24 h post FUS (h), male (n = 3 animals/timepoint) adult mice were anaesthetized with a mix of ketamine (80 mg/kg)/xylazine (10 mg/kg) and transcardially perfused with phosphate-buffered saline (PBS; 50 mM, pH 7.4), followed by 3.5% acrolein and 4% paraformaldehyde diluted in phosphate buffer (PB; 100 mM, pH 7.4). Once extracted from the skull, brains were post-fixed in 4% paraformaldehyde diluted in PBS for 2 h at room temperature (RT). After 3 x 10 min washes with PBS, the ipsi- and contra- brain hemispheres were separated using a blade and horizontal brain sections with 50 μm thickness were prepared in ice-cold PBS using a vibratome (VT1200S, Leica Biosystems, Ontario, Canada) at frequency of 90–100 Hz and a speed of 0,5 mm/s. The sections were stored at -20°C in cryoprotectant (30% (v/v) glycerol and 30% (v/v) ethylene glycol in PBS) until further processing.

2.4. Microglial density, distribution and morphology

To describe the short-term microglial response to MRIgFUS, I took a multiscale approach, investigating snapshots of micro-structural changes first, followed by the nanometric ones. As such, I detail next the methodology used for the microglial density, distribution and morphology analyses. In the subsequent section (2.5), I describe the methods utilized instead in the ultrastructural investigation.

2.4.1. Double immunohistochemistry and brightfield imaging

Double immunohistochemistry staining against Iba1 and IgG was performed in 3 sections (in both the ipsi- or contra- hemisphere) per animal (n = 3 animals/timepoint). As previously discussed, Iba1 is expressed by microglia but also peripheral and border associated macrophages (Šimončičová et al., 2022). However, the MRIgFUS settings we utilized is not typically associated with peripheral immune cell infiltration in the brain, thus, herein I use Iba1 staining to refer to microglia (See section 1.3.3.). IgG was used to delineate regions of increased BBB permeability after MRIgFUS (Jordão et al., 2013). The sections containing the ventral hippocampus (Bregma -2.36 mm to -3.44 mm) were selected based on a qualitative assessment of T1-weighted scans showing maximum BBB permeability, as well as the Paxinos and Franklin Stereotaxic Atlas, 4th edition (Paxinos & Franklin, 2019).

Sections were first assessed for IgG staining. Free-floating sections immersed in cryoprotectant were washed in PBS 3 x for 10 min each. Next, the sections were quenched with 2% H_2O_2 diluted in 70% methanol for 10 min. After 3 subsequent 10 min PBS washes, the sections were placed in 0.1% $NaBH_4$ diluted in PBS for 30 min. This was followed by 3 x 10 min washes with PBS. Sections were then incubated in a blocking solution of 10% normal donkey serum and 1% Triton X-100 in Tris-buffered saline (TBS; 50 mM, pH 7.4) for 1 h at RT. Blocking buffer was also used to dilute the secondary antibody donkey anti-mouse IgG (1:500, cat# 715-065-150, Jackson ImmunoResearch, Philadelphia, USA), in which sections were subsequently incubated for 2 h at RT. Sections were washed in TBS and immersed in an avidin-biotin solution (1:100 in TBS, cat# VECTPK6100, VECTASTAIN, Vector Labs, California, USA) for 1 h at RT. The staining was next revealed by incubation with a HRP substrate kit solution (cat# SK-4600, Vector® VIP, Vector Labs, California, USA).

The reaction was stopped using PB, where the sections were left to incubate overnight at 4°C. Only ipsi- sections that presented hippocampal IgG staining (visually inspected through hippocampal Vector® VIP pinkish coloration) were used next to ensure increased BBB permeability across all samples. Moreover, although hippocampal IgG staining was not detected in contra- sections, all sections had positive choroid plexus IgG staining indicating that the staining worked (data not shown). The next day, the sections were processed for Iba1 staining to visualize microglia. First, sections were immersed in a blocking solution of 10% fetal bovine serum, 3% bovine serum albumin (BSA), and 1% Triton X-100 in TBS for 1 h at RT. Subsequently, the blocking buffer was used to dilute the primary antibody Iba1 (1:1000, Iba1, cat# 019-19741, FUJIFILM Wako Chemical, Virginia, USA), where the sections were left incubating overnight at 4°C.

The following day, the sections were washed 3 x for 10 min in TBS and incubated in a biotinylated goat anti-rabbit secondary antibody (1:300 in TBS, cat# 111-066-046, Jackson Immunoresearch, Philadelphia, USA). After 3x 10 min washes in TBS, the sections were once again incubated for 1 h in an avidin–biotin solution (1/100 in TBS, cat# VECTPK6100, VECTASTAIN ABC HRP Kit, Vector Labs, Labs, California, USA). They were washed 3 x 10 min in TBS and revealed in a solution containing 0.05% 3-3′-diaminobenzidine (DAB, D5905-50TAB, Millipore Sigma, Massachusetts, USA) and 0.015% H_2O_2 in 100 mM Tris–HCl. Sections were mounted onto glass slides and allowed to dry for 72 h. Slides were incubated in Milli-Q water (Milli-Q) for 5 min and dehydrated in increasing ethanol concentrations (50%, 70%, 80%, 90%, 100%, 100% for 5 min each) at RT. After 2 x 5 min incubations in xylene (cat# 534056, Millipore Sigma, Massachusetts, USA), the glass slides were cover-slipped with

distyrene, plasticizer, and xylene (DPX) mounting medium (cat# 13510, Electron Microscopy Sciences, Pennsylvania, USA).

Images (1 hemisphere/animal, n = 3 animals/timepoint) of the whole hippocampus were captured in a single z plane at 40× with numerical aperture of 0.65, using a Basler area scan camera (2.3 MP; a*cA1*920-40uc) and visualized through the Microvisioneer manualWSI Scan software (2019B-3S; Microvisioneer, Baden-Württemberg, Germany).

2.4.2. IgG qualitative and quantitative light analysis

The IgG staining was measured in the *CA1*, *LMol*, *Rad*, *Py* and *Or* of 3 sections (in both the ipsi- or contra- hemisphere) per animal (n = 3 animals/timepoint). The Vector® VIP substrate used to reveal the IgG staining produces a pink-to-brown parenchymal deposition, visually identified in the samples. Moreover, the mean gray value used for optical density analysis was obtained through FIJI (V2.13.1 for Mac OS X 10.7, FIJI, National Institutes of Health, Wisconsin, USA) (Schindelin et al., 2012). Each value was processed using the following formula (Bordeleau, M et al. 2021), to infer the presence of BBB permeability, where minimal intensity value is black (0) and indicates no IgG permeability and maximum intensity value is white (255), suggesting absolute presence of IgG:

$$Calibration\ optical\ density = \log_{10}\left(\frac{I_{min}}{I_{max}}\right) = \log_{10}\left(\frac{Mean\ gray\ value_{background}}{Mean\ gray\ value_{Region\ of\ interest}}\right)$$

2.4.3. Microglial density and distribution analyses

I acknowledge the contributions of Keelin Henderson Pekarik, from the Tremblay Lab, who carried out the region of interest tracing in the following section:

All analyses were performed blinded to the experimental conditions using FIJI software (V2.13.1 for Mac OS X 10.7, FIJI, National Institutes of Health, Wisconsin, USA) (Schindelin et

al., 2012), as previously described (Tremblay et al., 2010). First, based on the Paxinos and Franklin Stereotaxic Atlas, 4th edition (Paxinos & Franklin, 2019), the freehand selection tool was used to trace the region of interest (ROI), the *CA1* along with all of its strata, *Or, Py, Rad, LMol* (Figure 3). Considering the structural diversity within these layers (De Felice et al., 2022; Jinno et al., 2007), I analyzed each strata individually.

The Iba1+ cell density and distribution were assessed in 3 sections (in both the ipsi- or contra- hemisphere) per animal (n = 3 animals/timepoint) and ROI via a semi-automated macro. I analyzed 3,079 Iba1 positive (+) cells in total (minimum of 227 microglia/layer/timepoint), a sample size which was considered sufficient to obtain statistical power based on calculations obtained using G*Power software (V3.1.9.6 for Mac OS X 10.7, G* Power Software, Nordrhein-Westfalen, Germany) (effect size of 0.25 and power of 0.8 estimated to 128 individual cells) (Faul et al., 2007). First, the area of the traced *CA1* was measured in pixels and converted into μm^2. Each Iba1+ cell in focus containing a minimum of 3 processes was marked by a dot using the brush tool. Next, the *CA1* layers were duplicated in new images, converted to 8-bit and processed utilizing the grayscale and threshold, which segment images into features of interest and background. The resulting images were analyzed using the plugin "analyze particles" to detect objects with size and circularity corresponding to a dot. Moreover, the "NND" plugin was used to measure the distance between the center of all other dots in the image Microglial density was defined as the total number of Iba1+ cells divided by the total area (# microglia/μm^2). The NND of Iba1+ cells was obtained by quantifying the average distance between each positive cell to its nearest neighbour (μm). The spacing index (arbitrary unit, a.u.) was calculated as the square of the average NND multiplied by the microglia density. The spacing index can inform how regular or irregular the distribution of cells is according to the area. Two or more cells less

than 12 µm apart were considered a cluster and averaged by animal to obtain the cluster density (# clusters/µm^2) (Enlow et al., 2021). Overall, changes in microglia number, distance and regularity provide insights into microglia surveillance, which can notably impact synaptic plasticity (Gonçalves de Andrade et al., 2022).

2.4.4. Microglial morphology analysis

All ipsi- *LMol* areas were positive for IgG staining, while the remaining ipsi- *CA1* strata had less consistent staining, particularly at 1 h after MRIgFUS. I thus hypothesized that the *LMol* was the primary layer impacted by increased BBB permeability in the *CA1*. Accordingly, *LMol* Iba1+ cells were randomly selected for the morphology analysis in 3 sections (in both the ipsi- or contra- hemisphere) (n = 21 cells/hemisphere, N = 3 animals/timepoint). This sample size was sufficient to obtain statistical power based on calculations obtained using G*Power software (V3.1.9.6 for Mac OS X 10.7, G* Power Software, Nordrhein-Westfalen, Germany) (effect size of 0.25 and power of 0.8 estimated to 128 individual cells) (Faul et al., 2007). A previously developed semi-automated macro was adapted to this project (Bordeleau et al., 2019). Briefly, after tracing the cell body using the freehand selection tool, the area (µm^2), perimeter (µm), circularity ($4\pi \times$ (area/perimeter^2)), aspect ratio (major axis/minor axis, a.u.), roundness (arbor area/area of a circle with same convex perimeter, a.u.) and solidity (area/convex cell area, a.u.) were obtained. A circularity of 1.0 represents a perfect circle and 0.0 is indicative of an elongated cell shape. Similarly, values higher than a 1.0 aspect ratio equate to more elongated cell shapes. A solidity of 1.0 reflects a less ramified, convex shape, whereas 0.0 solidity points to a porous cell shape that is more ramified. Moreover, values closer to 1.0 for roundness represent more circular cell shapes (De Felice et al., 2022).

Next, the polygon tool was used to trace the endpoints of the microglial processes, creating a convex shape that serves as a proxy for the cellular territory. The image was converted to 8-bit and processed to produce an unsharp mask of the cell. Pixels outside the manual arbor were removed using the "remove outliers" function and the image was next subjected to thresholding. When necessary, the unsharp mask was manually corrected using the brush function to represent the observed cell. The "clear outside" and "despeckle" functions were used to turn the pixels outside the Iba1+ cell into background value and smooth the value of pixels within the mask. Once polished, the mask arbor was detected through the "analyze particles" command. The mask arbor was analyzed through the "analyze skeleton" function to calculate the number of branches, endpoints, average branch length, maximum branch length (μm) and longest shortest path (μm), increasing with the cell ramification. The mask arbor was also converted into an outline and analyzed using the FracLac (Karperien et al., 2013) plugin, as previously described (De Felice, Gonçalves de Andrade 2022). The fractal dimension (a.u.) and lacunarity (a.u.) were extracted based on the cell's contour. Fractal dimension increases proportionately to the repetition of a scale-invariant pattern, thus, the cell surface's complexity. In contrast, lacunarity rises in proportion to the heterogeneity of spacing across the cell surface. Fractal dimension and lacunarity are complementary; the first is particularly sensitive to morphology in whole cells, and the latter to features such as soma size and process length (Karperien et al., 2013). Higher values for the lacunarity index and fractal dimension indicate a more complex organization of branching and more ramified morphological states (De Felice et al., 2022).

2.5. Scanning electron microscopy staining and imaging

I acknowledge the contributions of Jared VanderZwaag who carried out part of the ultramicrotomy and the entire scanning electron microscopy imaging in the following section:

Double immunohistochemistry staining against Iba1 and IgG was performed in 3 sections (in both the ipsi- or contra- hemisphere) per animal (n = 3 animals/timepoint) in a similar protocol as described above (see Section 2.4.1). A few steps in the protocol were adapted to preserve tissue detail at the nanometric scale (St-Pierre et al., 2022). First, the quenching was performed with 0.3% H_2O_2 in PBS for 7 min. Secondly, the blocking buffer and antibody incubation solutions contained 0.01% Triton X-100. Thirdly, after the DAB incubations, sections were left in PB overnight at 4°C. Similar to the immunohistochemistry for light microscopy (see Section 2.4.1), all ipsi- sections used for electron microscopy had IgG staining in the hippocampus, detected with the naked eye via marked VIP pink-to-brownish staining. Moreover, all contra- sections had IgG staining in the choroid plexus.

Following double immunohistochemistry, the next day, sections were post-fixed flat using an osmium-thiocarbohydrazide-osmium protocol (De Felice et al., 2022). In this protocol, samples were first incubated in 3% potassium ferrocyanide (cat# PFC232.250, BioShop, Ontario, Canada) diluted in PB and combined (1:1) with 4% aqueous osmium tetroxide (cat# 19170, Electron Microscopy Sciences, Pennsylvania, USA) for 1 h at RT. The osmium potassium ferrocyanide improves the contrast and preservation of lipid containing membranes and droplets (St-Pierre et al., 2022). After 3 x 5 min washes with Milli-Q, the sections were immersed in 1% thiocarbohydrazide (cat# 2231-57-4, Electron Microscopy Sciences, Pennsylvania, USA) diluted in Milli-Q for 20 min at RT. The thiocarbohydrazide is used to link an additional layer of 2% osmium tetroxide diluted in Milli-Q to the tissue, applied for 30 min following 3 x 5 min Milli-Q H_2O washes at RT. This was followed by 5 x 3 min washes with Milli-Q and dehydration with ascending concentrations of ethanol (35%, 35%, 50%, 70%, 80%, 90%, 100%, 100%, 100%, each 5 min) and propylene oxide (3 x 5 min) (cat# 110205, Millipore Sigma, Massachusetts,

USA) at RT. Next, sections were embedded in Durcupan ACM resin (cat# 44611-44614, Millipore Sigma, Massachusetts, USA) overnight at RT. The following day, sections were covered with a thin layer of resin between two fluoropolymer sheets (ACLAR; cat# 50425-25, Electron Microscopy Sciences, Pennsylvania, USA) and placed for 72 h at 55 °C to polymerize. The ROI, the *LMol*, was excised from the flat-embedded sections on ACLAR® sheets and glued to the top of resin blocks (2/hemisphere/animal, n = 3 animals/timepoint). Ultrathin sections (~ 75 nm) were generated with an ultramicrotome (Ultracut UC7 ultramicrotome, Leica Biosystems, Ontario, Canada), collected on a silicon nitride chip, and glued onto specimen mounts for scanning electron microscopy (SEM). In each resin block, 6 levels (~ 5 µm apart) of ultrathin sections were collected. Imaging was done on 1 ultrathin section from each level at 5 and 25 nm of resolution using a Zeiss Crossbeam 350 Focused-Ion Beam SEM (Zeiss, Baden-Württemberg, Germany). In summary, from each animal (n = 3 animals/timepoint), 2 ipsi- and 2 contra- sections were stained to obtain 2 ipsi- and 2 contra- blocks, cut into 6 levels each. One ultrathin section was imaged per level, where Iba1+ microglial cell body were selected and exported as TIFF files with the Zeiss ATLAS Engine 5 software (Fibics, Ontario, Canada) at a resolution of 5 nm per pixel.

2.6. Ultrastructural analyses

To quantify ultrastructural changes, I analyzed 151 microglia cell bodies (N = 11-13 microglia from each ipsi- and contra- hemisphere, n = 3 animals/timepoint). This sample size was considered sufficient to obtain statistical power based on calculations using G*Power software V3.1 (effect size of 0.25 and power of 0.8 estimated to 128 individual cells) (Faul et al., 2007; St-Pierre et al., 2022). All analyses were blinded to the hemisphere, timepoint and animal. Images were analyzed using QuPath V0.4.3 (Bankhead et al., 2017) and FIJI (V2.13.1 for Mac

OS X 10.7, FIJI, National Institutes of Health, Wisconsin, USA) (Schindelin et al., 2012), adapted for use in previous work from our lab (Bordeleau et al., 2020). Microglial cell bodies were identified based on their positive DAB staining for Iba1 and their unique ultrastructure, notably their smaller cell bodies and nuclei than neighbouring astrocytes or neurons, a characteristic heterochromatin pattern, long stretches of endoplasmic reticulum (ER) distinct from oligodendrocytes, as well as a presence of inclusions (*e.g.,* lysosomes, lipofuscin granules) dispersed in their cytoplasm (De Felice et al., 2022; Savage et al., 2019; St-Pierre et al., 2022). Microglial processes were identified based on their positive staining for Iba1. Prior to analysis, a total of three trained and blinded observers separately agreed on the selected cells.

Microglial contacts were classified based on their ultrastructural hallmarks. Notably, contact with other cell bodies (*i.e.,* astrocytes and neurons), myelinated axons, blood vessels, and synaptic elements (pre-synaptic axon terminals and post-synaptic spines) were quantified (De Felice et al., 2022; Savage, et al., 2019; St-Pierre et al., 2022). The ultrastructural criteria used to identify each structure are outlined next. Astrocytes and astrocytic endfeet had pale nuclei with a thin rim of heterochromatin and pale irregular cytoplasm, often containing intermediate filaments (Peters, 1991). Astrocytic endfeet were considered swollen when increased drastically inside, showing a clear cytoplasm enclosed by a cell membrane (Nahirney & Tremblay, 2021). Neurons presented pale nuclei, cytoplasm and direct contacts with pre-synaptic terminals (Peters, 1991). Myelinated axons were characterized by electron-dense sheaths and granular cytoplasm, often presenting with mitochondria. Degraded myelin was recognized by ballooning, swelling or distancing between the well-defined myelin sheaths (Peters, 1991). Blood vessel area was recorded on FIJI. Using the freehand tool, I traced two orthogonal diameters, each delimited by the basement membrane, which was identified as electron-dense layers surrounding endothelial

cells and blood vessels. Because the orthogonal diameters were of different sizes, resembling a flattened circle, I used the ellipse formula to calculate an approximate vessel area (major radius*minor radius*π). The distance between each microglia and the most proximal blood vessel was also assessed using FIJI. Using the freehand tool, I traced a line connecting the microglia membrane (from either a cell body or process) and the closest basement membrane (De Felice et al., 2022; Savage et al., 2019; St-Pierre et al., 2022). Microglia were associated with a blood vessel when their distance from the vascular basement membrane was under 150 nm (De Felice et al., 2022; Savage et al., 2019; St-Pierre et al., 2022). Notably, justavascular microglial cell soma are 10 μm apart from blood vessels (Mondo et al., 2020). Moreover, among the parenchyma, microglial contacts with erythrocytes, which are marked by a complete electron-dense cytoplasm, were counted. Microglial contacts with synaptic elements were categorized as contacts with axon terminals or dendritic spines (De Felice et al., 2022; Savage et al., 2019; St-Pierre et al., 2022). Pre-synaptic axon terminals showed a minimum of five synaptic vesicles, and were usually in contact with post-synaptic spines, displaying a visible post-synaptic density (Peters, 1991). Extracellular space pockets, essential for microglial motility and neuronal remodeling, were classified based on clear spaces without delineating membranes directly surrounding the microglia (Bordeleau et al., 2020; Tremblay et al., 2010). Extracellular digestion referred to extracellular space pockets containing debris in the vicinity of a microglia cell body or process, often in proximity to degraded myelin (ballooning, swelling or distancing between the well-defined myelin sheaths) (Nahirney & Tremblay, 2021).

In addition to the extracellular environment, I also characterized the intracellular ultrastructural state of microglia. Notably, I analyzed ER/Golgi apparatus, lysosomes, lipofuscin, mitochondria, and phagosomes (De Felice et al., 2022; Savage et al., 2019; St-Pierre et al.,

2022). ER/Golgi cisternae were characterized by their long and narrow stretches. ER/Golgi apparatus dilation, associated with cellular stress, was identified when the distance between cisternal membranes was greater than 100 nm (El Hajj et al., 2019; St-Pierre et al., 2022). Mitochondria (homeostatic) were similarly found in the cytoplasm, presenting an electron-dense appearance, double membrane, numerous cristae, and a circular shape. Mitochondria bigger than 1 μm in length were established as elongated. These typically increase in response to cellular stress and protect cells from starvation (Gomes et al., 2011). Moreover, when presenting with deteriorated outer membrane, vacuoles or degradation in their cristae membranes (electron-lucent pockets), mitochondria were classified as dystrophic (De Felice et al., 2022; Savage et al., 2019; St-Pierre et al., 2022). Events of proximity between mitochondria and ER/Golgi apparatus, associated with calcium transfer and lipid synthesis (Lounas et al., 2022), were quantified. Moreover, endothelial, astrocytic endfeet and synaptic element containing mitochondria were counted. Mitochondrial apposition to the cell membrane has been proposed to represent a component of purinergic signaling attracting microglial cell or process contacts (Császár et al., 2022). Primary lysosomes were identified by their circular and homogenous contents (digestive enzymes) enclosed by a single membrane (De Felice et al., 2022; Savage et al., 2019; St-Pierre et al., 2022). Secondary lysosomes were darker, at least twice larger than primary lysosomes and often fused with phagosomes containing digested material. Tertiary lysosomes were the largest, presenting residual material, such as lipofuscin, large lipid bodies and phagosomes (De Felice et al., 2022; Savage et al., 2019; St-Pierre et al., 2022). Lipid bodies are sites for synthesis and storage of inflammatory mediators and were characterized by their electron-dense circular shape and interior. Oval structures with electron-dense content and a unique fingerprint-like pattern were identified as lipofuscin. Phagosomes were defined by their ovoid or circular shape with a

single membrane and electron-lucent interior. They were classified as empty (completely electron-lucent) or filled (electron-lucent with content) (De Felice et al., 2022; Savage, et al., 2019; St-Pierre et al., 2022). Autophagosomes, part of an intracellular degradation pathway, were instead identified by the presence of elements inside circular, double-membrane vacuole with a clear interior, resembling the cell's cytoplasm (Hui et al., 2018; St-Pierre et al., 2022).

2.7. Statistics

Microglial density, distribution, morphology and ultrastructural statistical analyses were conducted in the software GraphPad Prism (V 8.0.0 for MAC OS Ventura 13.4, GraphPad Software, California USA). Normality of the data was assessed using a Shapiro-Wilk test. A two-tailed paired Student's *t*-test was used to compare the average contrast intensity between ipsi- and contra- *LMol*. Mixed effects 2-way ANOVA with Šídák's multiple comparison correction was used for microglial density and distribution, optical density, morphology, and ultrastructure analyses comparing animal (n) averages between ipsi- and contra- *LMol* at both timepoints (Bordeleau et al., 2020). Post-hoc analyses compared ipsi- *vs* contra- and 1 h *vs* 24 h. Both nonparametric and parametric data were used for the 2-way ANOVA, considering there is no non-parametric alternative to this test. The frequency distribution of cell values (morphology and ultrastructure) was assessed using the Gaussian or Sum of 2 Gaussian nonlinear regression models for modal and bimodal data, respectively. The Wilcoxon test was applied to the nonlinear models comparing ipsi- *vs* contra- *LMol* in each timepoint (Enlow et al., 2021). When the number of recorded events within the cell dataset was not high enough to create the nonlinear model, I computed presence *vs* absence of the variable across conditions. The conditional relative frequency of ultrastructural changes was measured using Fisher's exact test. Spearman r correlations were computed for density and distribution, morphology and ultrastructural datasets

separately, as described below. Mean differences were considered statistically significant when $p < 0.05$, with **** $p < 0.0001$, *** $p < 0.001$, ** $p < 0.01$, * $p < 0.05$. All reported values are mean ± standard error of the mean (S.E.M).

2.7.1. Correlation analyses

To investigate a possible relationship between IgG staining, estimated by the optical density, and microglia density and distribution, I performed a correlation analysis. The ipsi- *CA1* density and distribution (n = 3 animals/timepoint) dataset (density, NND, spacing index and cluster density) and optical density values were imported into GraphPad Prism (V 8.0.0 for MAC OS Ventura 13.4, GraphPad Software, California, USA) for the analysis. The built-in correlation tool was used to compute the relationship between all features (Table 4). The same approach was used to understand the ipsi- relationships between the 30 morphological features analyzed and the IgG staining quantified by optical density (n = 3 animals/timepoint) (Table 5). In addition, I assessed possible relationships within the ipsi- and contra- ultrastructure dataset, primarily focusing on correlations between the distance to the closest vessel and vessel area to all microglia ultrastructural features analyzed. Using the same built-in correlation tool, values from both contra- and ipsi- *LMol* cells of both timepoints were included in the analysis (n = 151 cells, N = 3 animals/timepoint) (Table 11).

2.7.2. Principal component analyses

To better understand the variability between the ipsi- and contra- *LMol* at 1 and 24 h within the morphology and ultrastructure datasets, I took a dimensionality reduction approach using the built-in principal component analysis (PCA) tool available in the GraphPad Prism software (V 8.0.0 for MAC OS Ventura 13.4, GraphPad Software, California USA). Briefly, the variables were standardized to have a mean 0 and standard deviation of 1 to obtain a correlation matrix.

The principal components (PC) were selected based on a parallel analysis. Moreover, loadings and PC scores were visualized using scatterplots. Loadings and PC scores were used to understand the morphological and ultrastructural features that contributed to most variability in the ipsi- compared to the contra- *LMol*.

CHAPTER 3: RESULTS

3.1. Magnetic resonance imaging-guided focused ultrasound sonication with microbubbles increased hippocampal blood-brain barrier permeability in adult male mice

To investigate the modulatory effect of MRIgFUS on microglia, the ipsi- ventral hippocampus of adult male mice (n = 6 animals) was targeted by one ultrasound beam, while the contra-hippocampus was used as a control (Figure 4A). Immediately after MRIgFUS, gadolinium-enhanced T1-weighted MR images were acquired to verify increased BBB permeability, identified by gadolinium parenchymal entry (dashed circle) in every ipsi- hippocampus (Figure 4B). Elevated BBB permeability was also indicated by the detection of endogenous IgG in the ventral hippocampus *via* double immunoperoxidase staining for IgG and Iba1. Brightfield microscopy revealed IgG+ staining in the hippocampal parenchyma and alongside vessels only in the ipsi- *CA1* strata at both 1 and 24 h after MRIgFUS, indicating that BBB permeability increased only in the targeted region (Figure 4C inset). Further, significantly increased average voxel intensity, representative of parenchymal gadolinium leakage, was detected in the ipsi- compared to contra- hippocampus (Figure 4D, $p = 0.0449$, t = 2.661, Table 1). Notably, optical density assessing overall IgG staining was higher in the *LMol* ipsi- at 24 h compared to contra- at 24 h, contra at 1 h and ipsi- at 1h (Figure 4E, T $p = 0.0001$ and f = 17.49, Contra- 1h *vs* Ipsi- 24 h $p = 0.0013$ and t = 4.1970, Ipsi- 1h *vs* Ipsi- 24h $p = 0.0044$ and t = 3.7620, Contra-24 h *vs* Ipsi- 24 h $p = 0.0014$ and t = 4.1740, Table 1). By contrast, in the remaining *CA1* strata, *Rad*, *Py* and *Or*, there was no significant change (Table 1). Indeed, visual inspection of IgG staining was confirmed in all ipsi- *LMol* at 1h and 24 h, but only at 24 h for *Rad*, *Py* and *Or* (data not shown). This suggests that IgG staining of the parenchyma was more significantly increased following

ipsi- BBB modulation in the *LMol* at 24 h compared to 1 h and control regions, while for the remaining *CA1* strata it did not vary across time with MRIgFUS treatment.

3.2. Magnetic resonance imaging-guided focused ultrasound sonication with microbubbles did not change ventral *cornu ammonis* 1 microglial density and distribution at 1 and 24 h in adult male mice

BBB permeability modulation at 7 days and up to 7 weeks after MRIgFUS has been shown to affect microglia density and distribution (Kovacs et al., 2017; Silburt & Aubert, 2022), raising the question as to whether similar changes would be observed early after the treatment. Using immunoperoxidase staining for Iba1, I quantified the density, NND and spacing index of Iba1+ cells across individual *CA1* layers of the ipsi- and contra- hemispheres at 1 and 24 h (Figure 5A–D). There was no significant difference in microglial density between conditions (Figure 5E, H, K, N and Q, Table 2). However, I found a main effect of time in modulating the NND, in the *CA1* as a whole, but not a specific layer, which could be reflective of a general tendency to change the distance between cells in response to MRIgFUS (Figure 5R, n = 3 animals/timepoint, Mixed-effects ANOVA with Šídák's multiple comparisons test, T $p = 0.0464$ and $f = 5.5390$). By contrast, I did not detect significant differences in how microglia regularly distributed across the parenchyma (spacing index) or in the number of cells in close contact (cluster density) between contra- and ipsi- groups (Figure 5F–S, Table 2), suggesting that, while no expressive changes in microglia cell number or distribution were found, time had a significant effect in the overall distance between cells in the ventral *CA1* of adult male mice following MRIgFUS.

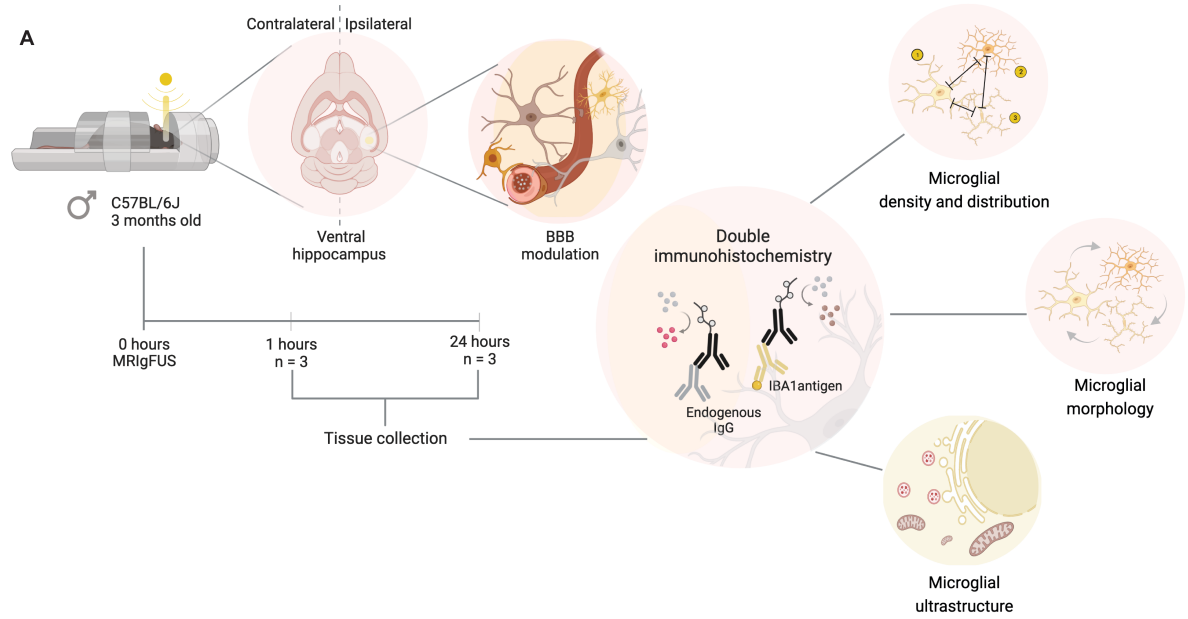
A
Contralateral
Ipsilateral
C57BL/6J
3 months old
Ventral
hippocampus
BBB
modulation
Microglial
density and distribution
Double
immunohistochemistry
IBA1antigen
Endogenous
IgG
Microglial
morphology
0 hours
MRIgFUS
1 hours
n = 3
24 hours
n = 3
Tissue collection
Microglial
ultrastructure

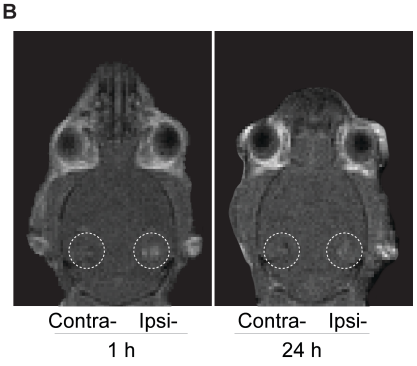
B
Contra-
Ipsi-
1 h
Contra-
Ipsi-
24 h

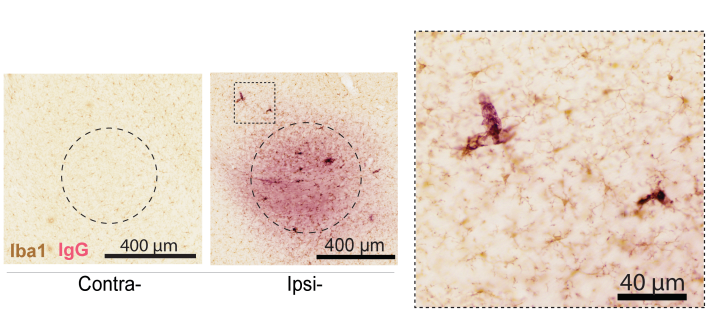
C
Iba1
IgG
400 µm
400 µm
Contra-
Ipsi-
40 µm

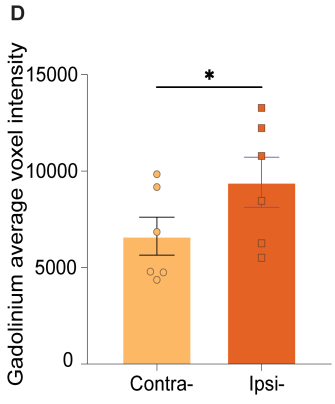
D
Gadolinium average voxel intensity
15000
10000
5000
0
*
Contra-
Ipsi-

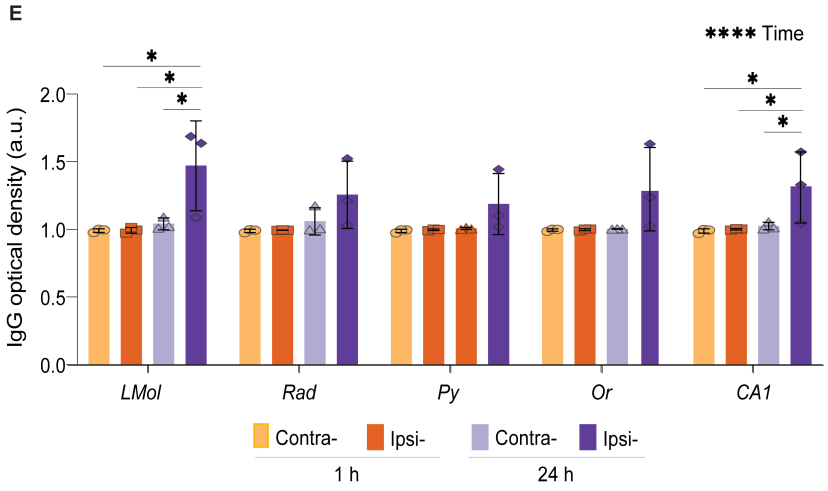
E
**** Time
IgG optical density (a.u.)
2.0
1.5
1.0
0.5
0.0
LMol
Rad
Py
Or
CA1
Contra-
Ipsi-
Contra-
Ipsi-
1 h
24 h

Figure 4. Magnetic resonance imaging-guided focused ultrasound sonication with microbubbles opens the blood-brain barrier in the ipsilateral hippocampus of adult male mice.

A. Scheme of the methodology. Briefly, adult male mice were sonicated with magnetic resonance imaging-guided focused ultrasound sonication with microbubbles (MRIgFUS) targeting the left hemisphere (ipsilateral, ipsi-) ventral hippocampus, while the right hemisphere (contralateral, contra-) was used as a control. The animals were perfused, brains collected and sectioned at 1 and 24 hours (h). All tissue sections were processed using a double immunohistochemistry protocol targeting immunoglubulin G (IgG) and ionized calcium-binding adapter molecule 1 (Iba1). Samples were imaged using brightfield microscopy to assess microglial density, distribution and morphology, and scanning electron microscopy to analyze microglial ultrastructure. Created with BioRender.com. Agreement number: WK25QMGYX1. **B.** T1-weighted images confirmed increased blood-brain barrier (BBB) permeability indicated by gadolinium detection (dashed circle) in the ipsi- ventral hippocampus parenchyma at 1 and 24 h after MRIgFUS. **C**. Representative images of IBA1 and IgG immunoperoxidase double staining imaged with a 40x brightfield microscope. IgG was only detected in the ipsi- hemisphere and was often in circular shape (dashed circle), indicative of the area targeted by the focus. IgG was observed in the parenchyma and along vessels (inset). Scale bars 400 and 40 μm. **D.** The average voxel intensity was significantly increased in the ipsi- compared to the contra- hemisphere, supporting T1-weighted image findings. Bar graph shows mean, standard error of the mean, as well as individual data points (n = 3 animals/hemisphere/timepoint), analyzed with a paired two-tailed Student's *t*-test. **E.** Optical density was significantly increased in the ipsi- *stratum lacunosum moleculare* (*LMol*) at 24 h, *versus* contra- *LMol* at 24 h, ipsi- *LMol* at 1 h and contra- *LMol* at 1 h. Bar graphs show mean, standard error of the mean, as well as individual data points (n = 3 animals/hemisphere/timepoint), analyzed with a mixed effects 2-way ANOVA with Šídák's multiple comparison tests. * $p < 0.05$, ** $p < 0.01$, *** $p < 0.001$. a.u.: arbitrary unit, *Or*: *stratum oriens*, *Py*: *stratum pyramidale* and *Rad*: *stratum radiatum*.

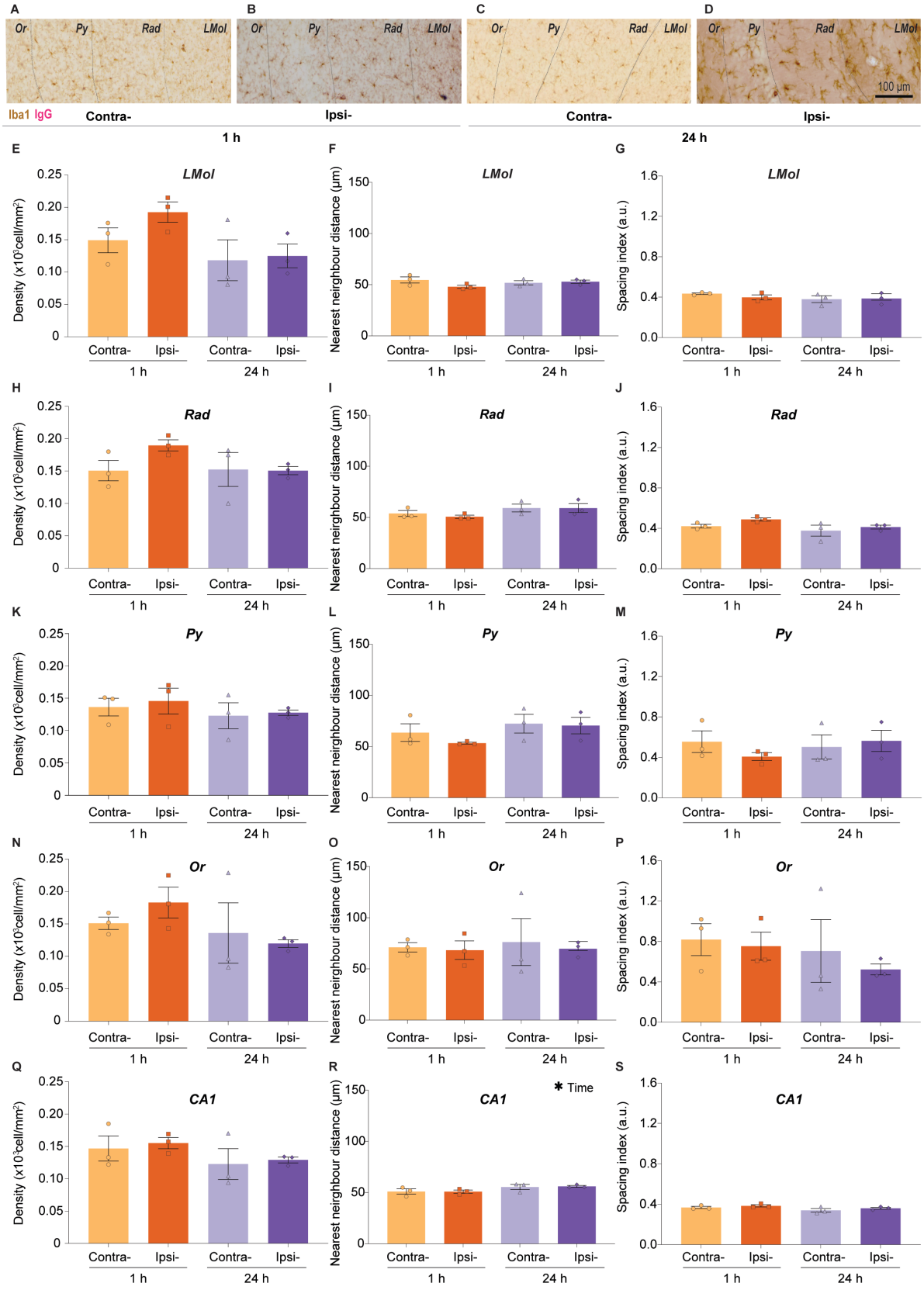
A
B
C
D
Or
Py
Rad
LMol
100 µm
Iba1 IgG
Contra-
Ipsi-
1 h
24 h
E
F
G
H
I
J
K
L
M
N
O
P
Q
R
S
LMol
Rad
Py
Or
CA1
Density (x10³cell/mm²)
Nearest neirghbour distance (µm)
Spacing index (a.u.)
* Time

Figure 5: Time has a significant effect in the proximity of microglia cells in the ventral *cornu ammonis 1* following magnetic resonance imaging-guided focused ultrasound sonication with microbubbles in adult male mice.

A-D. Representative brightfield microscopy images taken at 40x illustrate ionized calcium-binding adapter molecule 1 (Iba1) positive (+) cell and immunoglubulin G (IgG)+ parenchymal distribution along the 4 (*cornu ammonis 1*) *CA1* strata. Accordingly, images were obtained in ipsilateral (ipsi-) and contralateral (contra-) hemispheres of adult male mice at 1 hour (h) and 24 h following double immunoperoxidase staining. **E-P.** There were no differences between brain hemispheres in Iba1+ cell density, nearest neighbour distance and spacing index in the *stratum lacunosum moleculare (LMol)* (**E-G**), *stratum radiatum (Rad)* (**H-J**), *stratum pyramidal* (*Py)* (**K-M**), *stratum oriens (Or)* (**N-P**) of adult male mice at 1 and 24 h. **Q-S.** In the overall *CA1* (counted separately), both the density and spacing index were not altered, despite a main effect of time in the nearest neighbour distance. Bar graphs show mean, standard error of the mean, as well as individual data points (n = 3 animals/hemisphere/timepoint). Statistical significance was assessed by a mixed-effects 2-way ANOVA. Scale bar 100 μm. a.u.: arbitrary unit.

3.3. The distribution of morphological states varies in response to magnetic resonance imaging-guided focused ultrasound sonication with microbubbles

Microglia modify the size of their cell body and the shape, number and form of their processes to continually probe the brain parenchyma (Šimončičová et al., 2022). Following 7 days after MRIgFUS, hippocampal microglia form focal and proximal morphological clusters in male adult mice (Silburt & Aubert, 2022), possibly in response to infiltration of blood-derived molecules. I next examined if microglia also change their morphology at 1 and 24 h in the ipsi- *CA1 LMol* of adult mice, where I observed high prevalence and temporal variation of IgG + staining. The cell body of Iba1+ cells was manually traced (Figure 6A-D, Table 3) to measure the soma area, perimeter, aspect ratio, solidity, circularity and roundness (Figure 6E-N, Table 3). The same shape descriptors were used to assess the convex shape, determined through manual tracing of process endpoints (Table 3). Moreover, I generated a complementary automated arbor mask

(Figure 7A-D, Table 3), which was used to evaluate the fractal pattern of the cell outline (Table 3), shape descriptors (Figure 7E-P, Table 3) and mask arborization (Figure 8A-D, Table 3). Animal averages of each descriptor were used to infer the overall microglia temporal response to MRIgFUS. Mean changes obtained in each *LMol* represent a coordinated response of a population of cells engaged in specific microenvironments (Stratoulias et al., 2019). Different animals may adopt distinct strategies to reach the same overall outcome (Waldherr, 2018; Zanier et al., 2015). In light of this diversity, I also characterized the relative distribution of each morphological parameter using nonlinear regression models.

3.3.1. The distributions of microglial soma shape descriptors changed following magnetic resonance imaging-guided focused ultrasound sonication with microbubbles

The average soma area (Figure 6E, Table 3), aspect ratio (Figure 6G, Table 3), solidity (Figure 6H, Table 3) and circularity (Figure 6J, Table 3) were not significantly different at 1 and 24 h after MRIgFUS in the ipsi- *vs* contra- *LMol*. However, I observed an increase in soma perimeter in the ipsi- compared to contra- at 24 h (Figure 6F, n = 3 animals/timepoint, Hemisphere p = 0.0171 and F = 15.4300, Hemisphere x Time p = 0.0474 and F = 8.0070, 24 h p = 0.0175 and T = 4.7780). Although soma roundness decreased in the contra- at 24 h *vs* 1 h (Figure 6I, n = 3 animals/timepoint, Time p = 0.0102 and F = 11.1700, Contra- at 1 h *vs* 24 h p = 0.0423 and T =2.8540), it did not significantly change in the ipsi- *LMol* across the two timepoints (Figure 6I, Table 3). These results indicate an increase in the average cell body perimeter of microglia in response to MRIgFUS with a preservation of the roundness, area, aspect ratio, circularity and solidity initial values across the two hemispheres.

In addition, nonlinear regression curves of the relative distribution of soma area (Figure 6K, 1 and 24 h p = <0.0001), perimeter (Figure 6L, 1 and 24 h p = <0.0001), aspect ratio (Figure 6M, 1 and 24 h p = <0.0001), solidity (Figure 6N, 1 and 24 h p = <0.0001) and roundness (Figure 6O, 1 and 24 h p = <0.0001) significantly changed in the ipsi- *vs* contra- *LMol* at 1 and 24 h, although only at 1 h for soma circularity (Figure 6P, 1 h p = <0.0001). This suggests that the overall balance of soma states in the *LMol* changes in response to MRIgFUS at 1 and 24 h.

Analysis of the amplitude and mean of each ipsi- curve in comparison to the contra- model provided further insights into how these relative distributions were modified across treatment and timepoint (Table 3). Briefly, higher amplitudes indicate decrease in spread, while higher means point to a shift towards elevated values for the variable analyzed. Correspondingly, the ipsi- soma area and roundness mean increased at 1 and 24 h, along with the amplitude at 1 h, which sequentially decreased at 24 h (Table 3). Alternatively, the ipsi- soma perimeter mean was higher at 1 and 24 h, while the amplitude was lower at both timepoints (Table 3). The ipsi- soma aspect ratio mean increased at 1 h, with the reverse effect seen at 24 h, whereas the amplitude increased at 1 and 24 h (Table 3). By contrast, the ipsi- circularity mean decreased at 1 and 24 h, while a lower amplitude was present only at 1 h (Table 3). Moreover, the ipsi- solidity mean decreased at both timepoints, while the amplitude increased at 1 h and sequentially decreased at 24 h (Table 3). These findings reveal that part of the microglial population in the ipsi- deviate to bigger soma area, perimeter, roundness, but smaller circularity and solidity states at 1 and 24 h following MRIgFUS (Figure 6K-P). As a result, there is a lower soma area, roundness, solidity and aspect ratio, but higher perimeter, circularity distribution heterogeneity measured at 1 h. By contrast, at 24 h, this heterogeneity is higher for soma area, roundness, solidity and perimeter (Figure 6K-P).

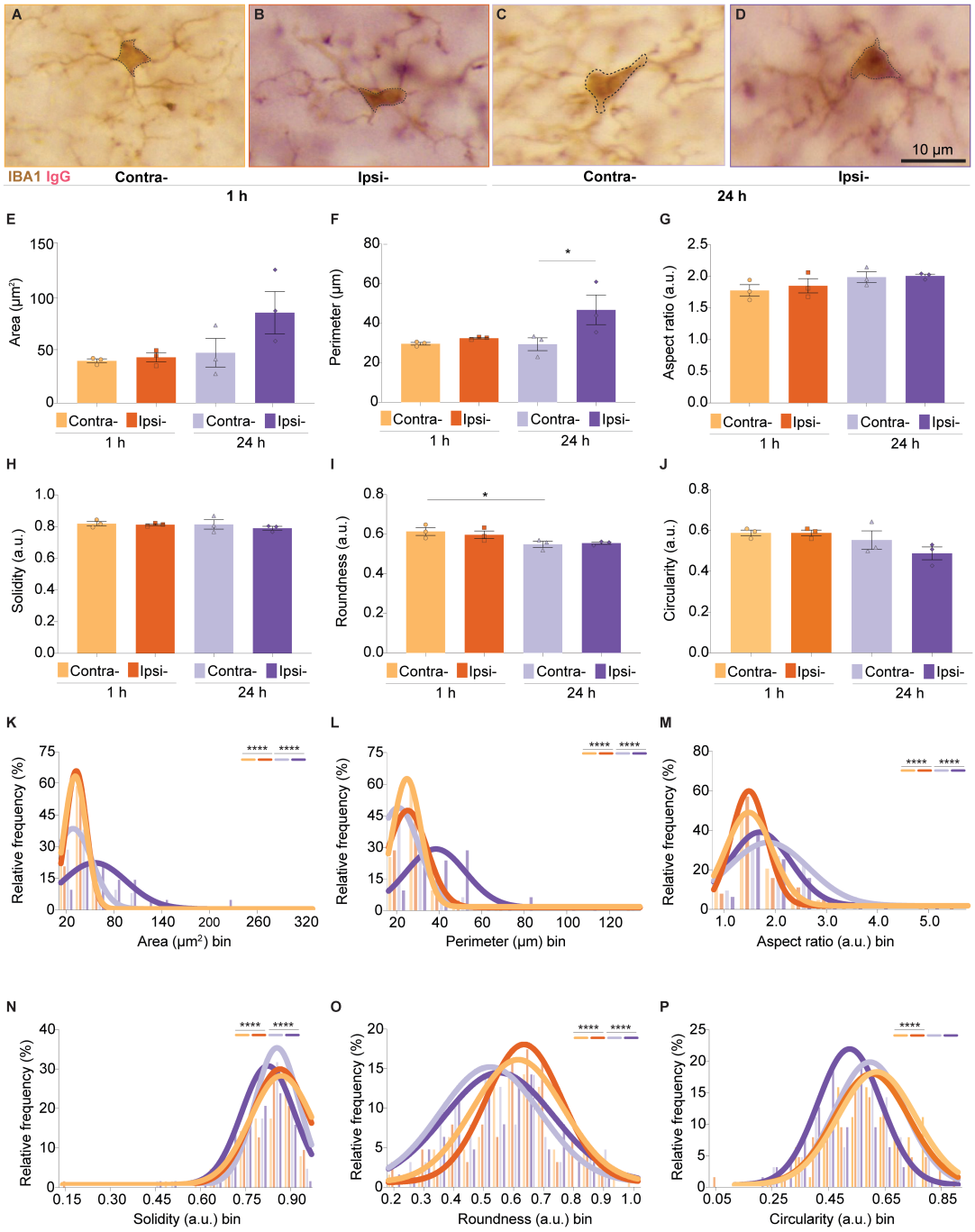
A
B
C
D
10 µm
IBA1 IgG
Contra-
Ipsi-
Contra-
Ipsi-
1 h
24 h
E
Area (µm²)
F
Perimeter (µm)
G
Aspect ratio (a.u.)
H
Solidity (a.u.)
I
Roundness (a.u.)
J
Circularity (a.u.)
Contra-
Ipsi-
1 h
24 h
K
L
M
Relative frequency (%)
Area (µm²) bin
Perimeter (µm) bin
Aspect ratio (a.u.) bin
N
O
P
Solidity (a.u.) bin
Roundness (a.u.) bin
Circularity (a.u.) bin
****
*

Figure 6. The distribution of soma shape descriptors is significantly altered at 1 and 24 hours following magnetic resonance imaging-guided focused ultrasound sonication with microbubbles in adult male mice ventral *cornu ammonis 1 stratum lacunosum moleculare* microglia.

A-D. Representative brightfield microscopy images taken at 40x illustrate ionized calcium-binding adapter molecule 1 (Iba1) positive (+) cell, soma tracing (dashed line) and immunoglubulin G (IgG)+ parenchymal distribution across the 1 and 24 hours (h) contralateral (contra-) and ipsilateral (ipsi-) *lacunosum moleculare* (*LMol*) following magnetic resonance imaging-guided focused ultrasound sonication with microbubbles (MRIgFUS). Scale bar 10 μm. **E–J**. Iba1+ soma area (**E**), aspect ratio (**G**), solidity (**H**) and circularity (**J**) averages did not change in the ipsi- *LMol* of adult male mice at 1 or 24 h, compared to the contra- controls. The soma perimeter (**G**) was significantly increased in the ipsi- vs contra- *LMol* 24 h. Moreover, the soma roundness decreased in the contra- at 24 h *vs* 1 h. Bar graphs show mean, standard error of the mean, as well as individual data points (n = 3 animals/hemisphere/timepoint) analyzed by a mixed-effects 2-way analysis of variance (ANOVA). **K–P**. According to nonlinear regression models, the relative distribution of soma area (**K**), perimeter (**L**), aspect ratio **(M),** solidity (**N**) and roundness **(O)** was significantly distinct in the ipsi- *LMol* compared to the contra- control at both 1 and 24 h. The ipsi *vs* contra- nonlinear regression distribution of soma circularity (**P)** was only different at 1 h. Histograms show the relative frequency and nonlinear regression analyzed via Wilcoxon comparison tests. *p < 0.05, **p < 0.01, ***p < 0.001. a.u.: arbitrary unit.

3.3.2. The distributions of microglial convex shape descriptors changed following magnetic resonance imaging-guided focused ultrasound sonication with microbubbles

The average microglia convex area, aspect ratio, perimeter, roundness, circularity and solidity did not change between the ipsi- and contra- *LMol* at 1 and 24 h following MRIgFUS (Table 2). Overall, this suggests that microglia retain their initial convex forms across the two timepoints and hemispheres. Notably, nonlinear regression curves of the relative distribution of convex area (1 h p = <0.0001, 24 h p = 0.0029), aspect ratio (1 and 24 h p = <0.0001), circularity (1 and 24 h

p = <0.0001) and roundness (1 and 24 h p = <0.0001) significantly changed in the ipsi- *vs* contra- *LMol* at 1 and 24 h. The nonlinear regression curve fit of convex perimeter (1 h p = 0.0006) was only different at 1 h, while convex solidity (Table 3) remained unchanged after MRIgFUS. Shifts in the distribution of convex shape descriptors at 1 and 24 h are evidence of an intra-population response to MRIgFUS.

Description of the ipsi- *vs* contra- nonlinear regression means and amplitudes was performed to characterize further these shifts. The ipsi- convex area mean decreased at 1 h but increased at 24 h, with a lower amplitude detected at both timepoints (Table 3). The ipsi- convex aspect ratio mean, on the other hand, increased at 1 h and 24 h, with the opposite effect seen for the amplitude (Table 3). In addition, the ipsi- convex circularity mean was higher at 1 h but lower at 24 h, with an elevated amplitude measured in both cases (Table 3). Alternatively, the ipsi- perimeter mean decreased, with an opposite effect on the amplitude observed at 1 h. The ipsi- roundness mean increased at 1 h but lowered at 24 h, in both instances decreasing the amplitude (Table 3). The significant shifts in the regression models indicated a tendency towards smaller convex areas and perimeter, but bigger aspect ratios, circularity and roundness values at 1 h. Following 24 h, microglia tended to reduce circularity and roundness and elevate area and aspect ratio magnitudes (Table 3). Such changes lead to overall higher convex area, aspect ratio and roundness distribution heterogeneity, but the reverse effect on perimeter and circularity was seen at 1 and 24 h, except for perimeter, which was only significantly changed at 1 h (Table 3).

3.3.3. The distributions of microglial automated mask shape descriptors changed following magnetic resonance imaging-guided focused ultrasound with microbubbles

The automated mask area (Figure 7E), perimeter (Figure 7F), roundness (Figure 7G) solidity (Figure 7H) aspect ratio (Table 3), circularity (Table 3) averages were not significantly different between the ipsi- and contra- *LMol* at 1 and 24 h after MRIgFUS. To investigate more subtle changes in overall cell shape complexity, I additionally evaluated the fractal dimension and lacunarity indexes of cells. Analysis of averages of fractal dimension (Figure 7I) and lacunarity (Figure 7J) returned, however, similar results. Our findings suggest that microglia retain their average mask forms at 1 and 24 h after MRIgFUS. However, the nonlinear regression curves of the relative distribution of automated mask area (Figure 7K, 1 and 24 h $p = 0.0001$), perimeter (Figure 7L, 1 and 24 h $p = 0.0001$), roundness (Figure 7M, 1 h $p = 0.0028$ and 24 h $p = 0.0040$), solidity (Figure 7N, 1 and 24 h $p = 0.0001$), fractal dimension (Figure 7O, 1 h $p = 0.0197$ and 24 h $p = 0.0008$) and lacunarity (Figure 7P, 1 and 24 h $p = 0.0001$) significantly differed between the ipsi- *vs* contra- *LMol* at 1 and 24 h. These shifts indicated that the overall balance of cell shapes across the population change in response to MRIgFUS at 1 h and 24 h.

To clarify the direction of these shifts, I evaluated the amplitude and mean of each ipsi- curve in comparison to the contra- model (Table 3). The ipsi- automated mask area mean decreased at 1 h but increased at 24 h, with an elevated amplitude measured at both timepoints (Table 3). Both ipsi- automated perimeter and roundness means decreased at 1 h and 24 h, along with the amplitude at 1 h, despite the reverse effect at 24 h (Table 3). The ipsi- solidity and lacunarity means decreased at 1 h and increased at 24 h, while the amplitude reduced at both timepoints (Table 3). The ipsi- fractal dimension mean decreased at 1 h but increased at 24 h,

with a similar pattern observed for the amplitude (Table 3). Altogether the nonlinear regression models point to part of the microglial population adopting a decreased area, perimeter, roundness, solidity, fractal dimension, lacunarity at 1 h (Table 3). Instead, microglia tend to increase their area, solidity, lacunarity and fractal dimension, but decrease perimeter and roundness at 24 h (Table 3). This contributes to lower area, but higher perimeter, roundness, solidity, lacunarity and fractal dimension distribution heterogeneity at 1 h (Table 3). By contrast, at 24 h, there is lower area, perimeter, roundness and fractal dimension, but higher solidity and lacunarity distribution heterogeneity (Table 3).

3.3.4. The distributions of microglial arborization descriptors changed following magnetic resonance imaging-guided focused ultrasound sonication with microbubbles

The average number of branches (Figure 8E) and junctions (Figure 8F), as well as maximum branch length (Figure 8G) and the longest shortest path (Figure 8H) did not change in the ipsi- compared to contra- *LMol* at 1 and 24 h. These results suggest that MRIgFUS does not affect microglial arborizations averages across the two timepoints. Notably, nonlinear regression curves of the relative distribution of number of branches (Figure 8I, 1 and 24 h $p = 0.0001$) and junctions (Figure 8J, 1 and 24 h $p = 0.0001$), as well as the maximum branch length (Figure 8K, 1 and 24 h $p = 0.0001$) and longest shortest path (Figure 9L, 1 h $p = 0.0001$, 24 h = 0.0451) across cells significantly differed between the ipsi- *vs* contra- *LMol* at 1 and 24 h. Shifts in the distribution of microglial arborizations across the population could help conserve overall averages after MRIgFUS.

Comparing the ipsi- *vs* contra- amplitude and mean of the nonlinear regression curves can offer clues of how the relative distributions of each parameter changed after MRIgFUS. The

ipsi- branches mean increased at 1 h but decreased at 24 h, for both timepoints, indicating a lower amplitude (Table 3). The ipsi- junctions mean decreased at 1 h and 24 h, with lower amplitude observed at 1 h but higher at 24 h (Table 3). The ipsi- longest shortest path mean decreased at 1 h and increased at 24 h, with an increased amplitude measured at both timepoints (Table 3). Similarly, the ipsi- maximum branch length mean decreased at 1 h and 24 h, but the amplitude decreased at 1 h, with the reverse effect seen at 24 h (Table 3). Overall, the nonlinear regression models suggest that the relative distribution of microglia with higher number of branches, but lower number of junctions, shorter longest shortest path and maximum branch length increases at 1 h (Table 3). By contrast, microglia with lower number of branches, junctions, shorter maximum branch length but longer longest shortest path increase at 24 h (Table 3). In addition, the model suggests that at 1 h there is a more heterogeneous distribution of number of branches, junctions and maximum branch length across microglia, with the opposite effect on longest shortest path (Table 3). By contrast, at 24 h, there is more heterogeneity of branches, while junctions, longest shortest path and maximum branch length have the reverse pattern (Table 3).

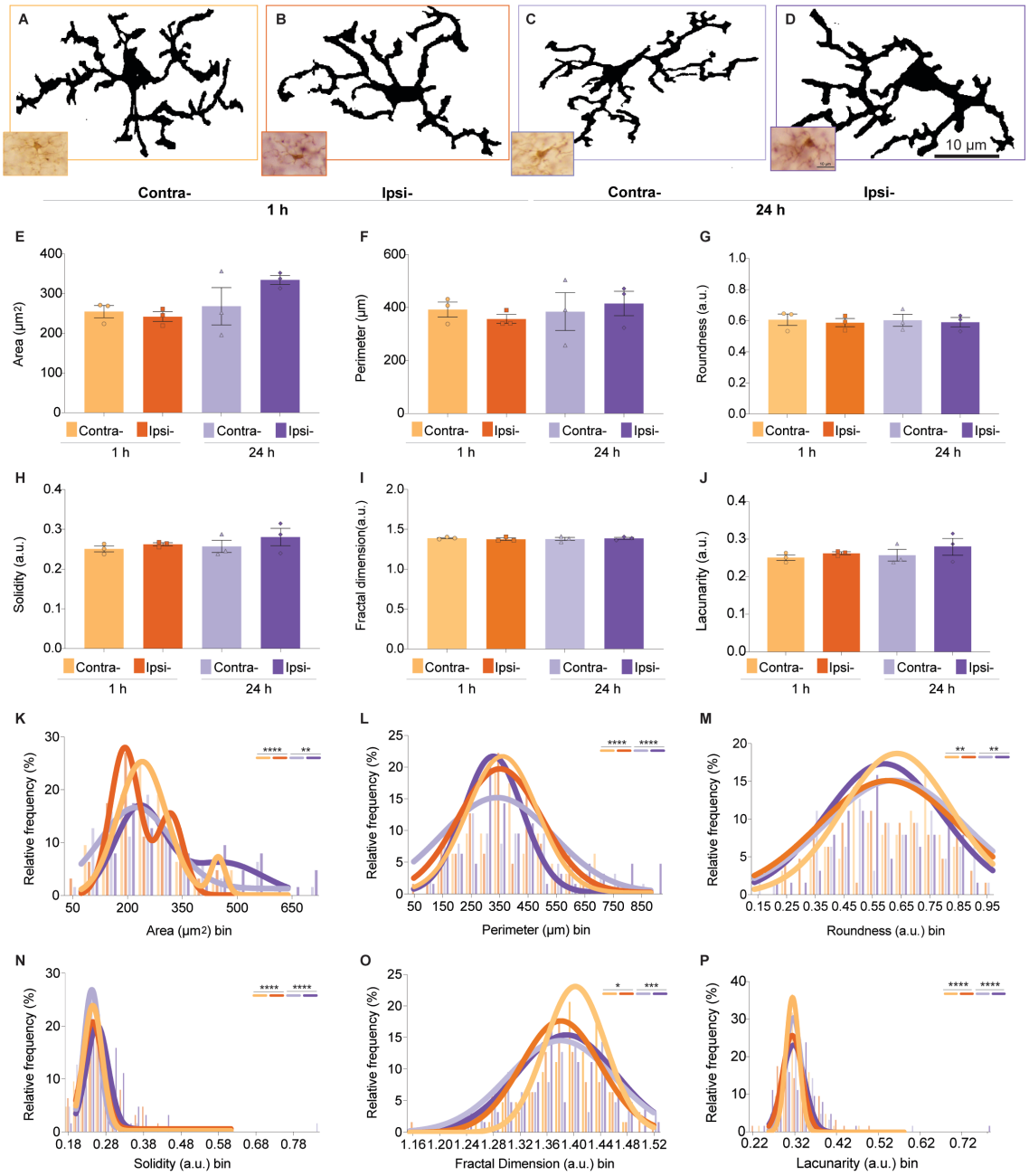

Figure 7. The distribution of automated cell mask shape descriptors is significantly altered 1 and 24 hours following magnetic resonance imaging-guided focused ultrasound sonication with microbubbles in adult male mice *ventral cornu ammonis 1 stratum lacunosum moleculare* microglia.

A–D. Representative brightfield microscopy automated cell masks obtained from 40x images illustrate ionized calcium-binding adapter molecule 1 (Iba1) positive (+) cells across the 1 and 24

hours (h) contralateral (contra-) and ipsilateral (ipsi-) *lacunosum moleculare (LMol)* following magnetic resonance imaging-guided focused ultrasound sonication with microbubbles (MRIgFUS). Scale bar 10 μm. **E–J**. Iba1+ automated cell mask area (**E**), perimeter (**F**), roundness (**G**), solidity (**H)**, fractal dimension (**I**) and lacunarity (**J**) averages did not change in the ipsi- *LMol* of adult male mice at 1 or 24 h, compared to the contra- controls. Bar graphs show mean, standard error of the mean, as well as individual data points (n = 3 animals/hemisphere/timepoint) analyzed by a mixed-effects 2-way analysis of variance (ANOVA). **K–P**. According to nonlinear regression models, the relative distributions of automated cell mask area (**K**), perimeter (**L**), roundness **(M)**, solidity (**N**), fractal dimension (**O)** and lacunarity **(P)** were significantly distinct in the ipsi- *LMol* compared to the contra- control at both 1 and 24 h. Histograms show the relative frequency and nonlinear regression analyzed via Wilcoxon comparison tests. $*p < 0.05$, $**p < 0.01$, $***p < 0.001$. a.u.: arbitrary unit.

3.3.5. Variability within density and distribution, but not morphology of microglia correlated with the IgG staining

The duration and dimension of the BBB modulation influence which molecules can infiltrate the brain and at which concentrations (Chen & Konofagou, 2014). To determine whether the IgG staining associated with changes in the density and distribution of microglia, I performed a Spearman r correlation of parameters in the ipsi- *CA1* at 1 and 24 h after MRIgFUS. I observed a significant negative correlation between optical density and microglia density (Figure 9A, n = 6 animals, $p = 0.0167$, r = - 0.9429, Table 4) and a positive correlation between optical density and NND (Figure 9A, n = 6 animals, $p = 0.0333$, r = 0.8857, Table 4).

In addition, I also hypothesized that IgG staining could be a predictor for morphological changes in microglia. I assessed this question using a Spearman r correlation of all 30 morphology parameters in the ispi- *LMol* at 1 h and 24 h with optical density (Figure 9B, Table 5). Optical density, however, did not correlate with any morphological parameter (Table 4).

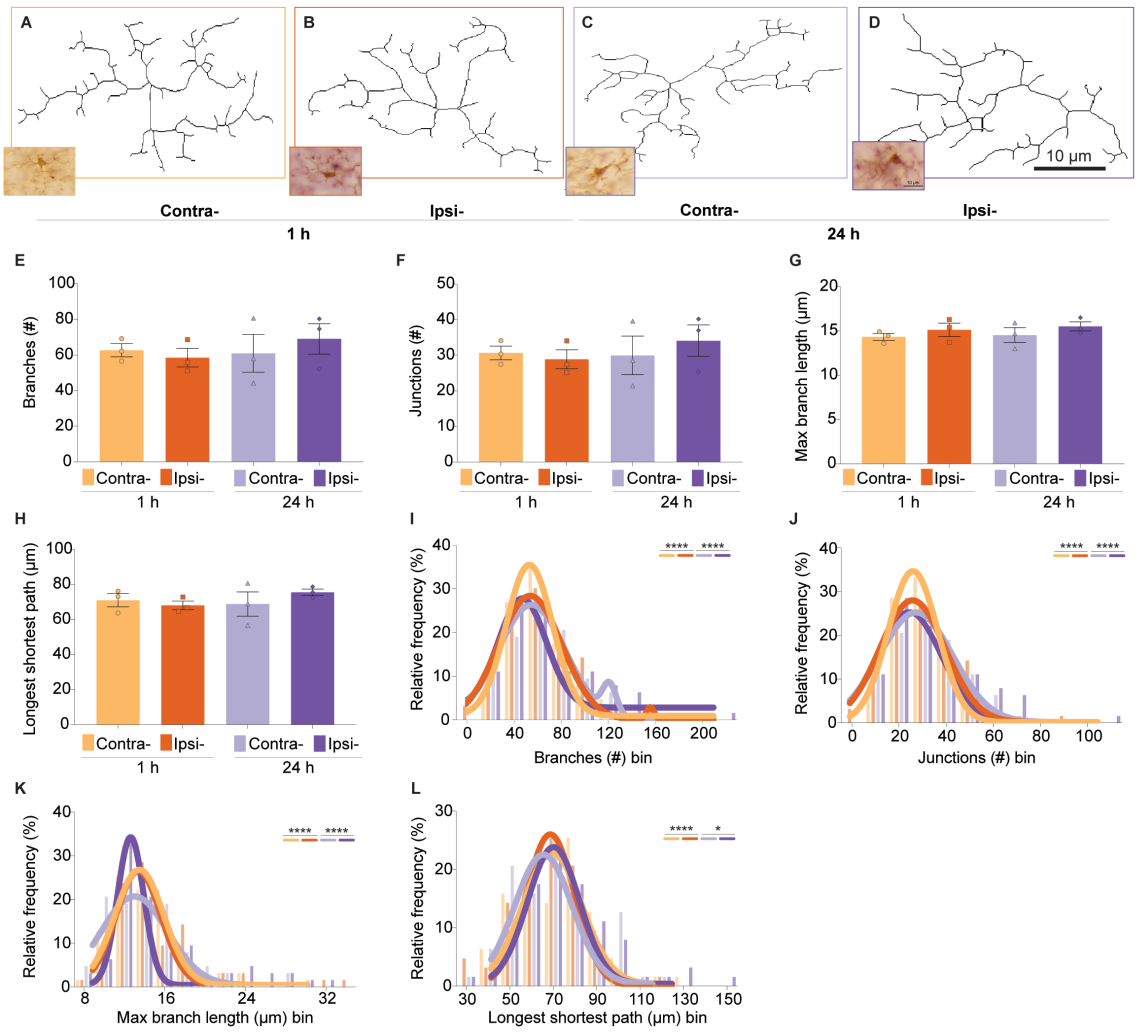

Figure 8. The distribution of arborization descriptors is significantly altered 1 and 24 hours following magnetic resonance imaging-guided focused ultrasound sonication with microbubbles in adult male mice ventral *cornu ammonis 1 stratum lacunosum moleculare* microglia.

A–D. Representative brightfield microscopy arborizations obtained from 40x images illustrate ionized calcium-binding adapter molecule 1 (Iba1) positive (+) cells across the 1 and 24 hours

(h) contralateral (contra-) and ipsilateral (ipsi-) *lacunosum moleculare (LMol)* following magnetic resonance imaging-guided focused ultrasound sonication with microbubbles (MRIgFUS). Scale bar 10 μm. **E–H**. The number of branches (**E**) and junctions (**F**), along with the max branch length (**G**) and longest shortest path (**H)** averages did not change in the ipsi- *LMol* of adult male mice at 1 or 24 h, compared to the contra- controls. Bar graphs show mean, standard error of the mean, as well as individual data points (n = 3 animals/hemisphere/timepoint) analyzed by a mixed-effects 2-way analysis of variance (ANOVA). **I–L**. According to nonlinear regression models, the relative distributions of branches (**I**) and junctions (**J**) number, as well as max branch length **(K)** and longest shortest path (**L**) were significantly distinct in the ipsi- *LMol* compared to the contra- control at both 1 and 24 h. Histograms show the relative frequency and nonlinear regression analyzed via Wilcoxon comparison tests. $*p < 0.05$, $**p < 0.01$, $***p < 0.001$. a.u.: arbitrary unit.

3.3.6. Magnetic resonance imaging-guided focused ultrasound sonication with microbubbles associated with microglial morphological variability at 24 h

Changes in the soma, territory, cell shape and arborization of microglia can happen simultaneously. I examined this multidimensionality in the morphology analysis by subjecting the 30 variables of the dataset to a PCA (Table 6). My goal was to evaluate which specific morphological parameters contributed most to the variability between ipsi- and contra-conditions. The analysis selected six PC, with PC1 explaining 39.23% and PC2 13.91% of the variations in the dataset (Figure 9C, Table 6). The distribution of all data points in the PC1 and 2 suggested that cells in the ipsi- *LMol* at 24 h contribute to most variability within the dataset (Figure 9C). Moreover, the loadings of variables for the PC1 and PC2 (Figure 9D) indicated that

across all variables, arborization parameters such as number of branches and junctions, most strongly correlated with variation within PC1 (Figure 9D and Table 6).

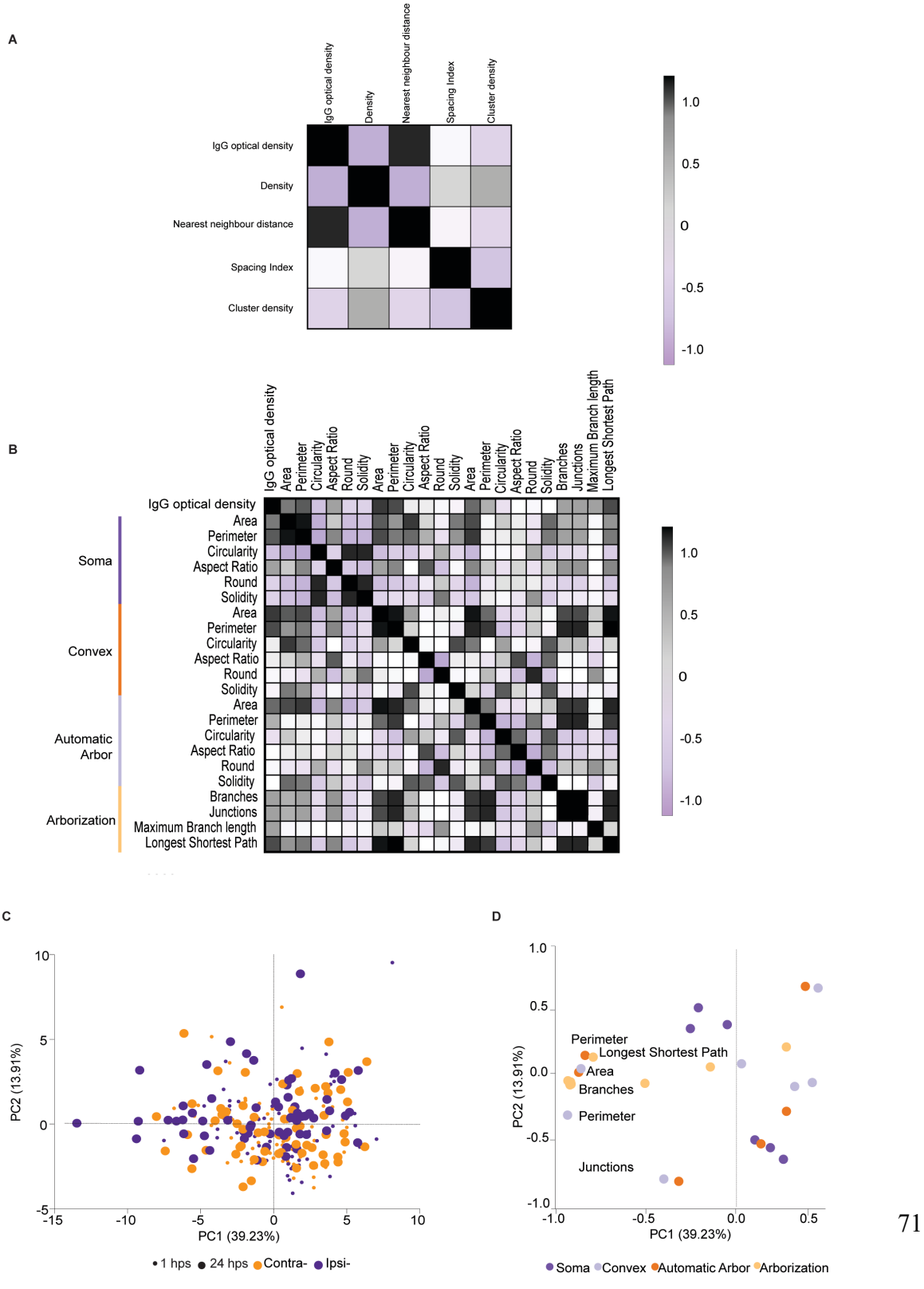

Figure 9. Changes in density and distribution correlate with IgG immunostaining intensity 1 and 24 hours following magnetic resonance imaging-guided focused ultrasound sonication with microbubbles in adult male mice ventral *cornu ammonis 1 stratum lacunosum moleculare* microglia.

A. Optical density was significantly and negatively correlated with microglial density, with the reverse relationship with microglial nearest neighbour distance (NND) in the ipsilateral (ipsi-) *lacunosum moleculare* (*LMol*) 1 and 24 hours (h) following magnetic resonance imaging-guided focused ultrasound sonication with microbubbles (MRIgFUS). **B.** Optical density did not correlate with any ipsi- adaptations in morphology. Correlation matrices of ipsi- features analyzed by Spearman r. **C.** Scores for the first and second principal component (PC1/PC2) of morphological features of all cells analyzed, colored according to the *LMol* hemisphere (orange: contralateral or contra-, purple: ipsi-) and timepoint (small icon: 1 h, big icon: 24 h). A higher variability in parameters is present at 24 h, particularly in the ipsi- group. **D.** Loading plot of morphology dataset, depicting the correlation between the morphological features (light orange: arborization, dark orange: convex shape, light purple: automatic arbor, dark purple: soma) and PC1/PC2, suggesting that variability in arborization descriptors contribute to overall differences between ipsi- and contra- *LMol* ionized calcium-binding adapter molecule 1 (Iba1) positive (+) cells.

3.4. The ultrastructure of microglia varies in response to magnetic resonance imaging-guided focused ultrasound sonication with microbubbles

Electron microscopy studies have offered tremendous insights into the function of microglia, showing, for example, their frequent modulatory contacts with synaptic elements, which can be partially or fully engulfed, and also physically separated (Savage et al., 2018). After systemic inflammation, which is associated with BBB leakage, several electron microscopy studies have suggested that microglia increased their proximity to blood vessels (Bowyer et al., 2020; Erickson et al., 2023; Haruwaka et al., 2019). Moreover, LPS has been similarly connected interactions between microglia and pre-synaptic contacts (Savageet al., 2019). Intracellularly, a

study using an AD pathology mouse model suggest that microglia present more ultrastructural signs of cellular stress (St-Pierre et al., 2022). It is, however, unclear whether similar responses would occur following MRIgFUS. To answer this question, I next investigated the ultrastructure of *CA1 LMol* microglia. Firstly, I evaluated whether microglia alter the number and frequency of their contacts with the BBB. Secondly, I verified if the interactions between microglia and the synaptic neuropil were impacted. Lastly, I measured the number and prevalence of their organelles. All these variables were accounted for at 1 and 24 h after MRIgFUS in adult male mice. Animal averages of each contact or organelle were used to assess the overall temporal response to MRIgFUS. Moreover, to understand specific cell population shifts in these parameters, I also characterized their relative distribution using nonlinear regression models for numerical and presence *vs* absence for categorical analyses.

3.4.1. *Cornu ammonis 1 stratum lacunosum moleculare* microglia change their interactions with blood-brain barrier components after magnetic resonance imaging-guided focused ultrasound sonication with microbubbles

Microglia interact with the BBB to provide physical support, modulate blood flow and seal possible leakages (Császár et al., 2022; Joost et al., 2019). This raises the intriguing possibility that following MRIgFUS, microglia increase their contacts with the BBB, particularly in the *LMol,* given its irrigation by large vessels such as the internal transverse hippocampal vein and external transverse hippocampal artery (Choi et al., 2010). I used scanning electron microscopy to quantify the interactions between Iba1+ cells and blood vessels in the ipsi- and contra- *CA1 LMol* of adult male mice at 1 h and 24 h following MRIgFUS. I did not find significant changes in the average number of microglia located less than 150 nanometers apart from blood vessels at 1 h and 24 h after MRIgFUS (Table 7). Similarly, the average distance between microglia and

blood vessels was not altered after MRIgFUS (Figure 10E, Table 7). Qualitatively, I observed that in the ipsi- *LMol* at 1 h, a Iba1+ process was located within the basement membrane and the endothelial cell (Figure 10B). I identified an interaction effect of microglia contacting the basement membrane (Figures 10A, C and F, Time *vs* Hemisphere $p = 0.0247$ and $F = 12.3100$). Moreover, the microglia touched astrocytic endfeet (Figure 10A-D and G), although these contacts did not change across contra- and ipsi- at 1 h and 24 h time points (Table 7). In rare occasions, I observed microglia contacting red blood cells which were found only in the ipsi- *LMol* parenchyma at 24 h in proximity to severely damaged blood vessels (Table 7).

MRIgFUS BBB modulation can result in swollen astrocytic endfeet in rabbits (Yoshino et al., 2009). However, the *LMol* can present swollen endfeet at steady-state conditions (Bonney et al., 2022). I observed swollen endfeet in both ipsi- and contra- *LMol* at 1 and 24 h (Figure 10B). The average number of contacts microglia made with swollen endfeet did not significantly change between contra- and ipsi- at 1 h and 24 h after MRIgFUS (Figure 10H). However, the relative frequency of these contacts was significantly higher in ipsi- *vs* contra- *LMol* at 1 h and 24 h (Figure 10I, 1 h $p = 0.0007$, 24 h $p = 0.0101$, Table 8).

In addition, it has been proposed that mitochondria lined up near the endothelial cell membrane can participate in purinergic signaling to attract microglia to blood vessels in both humans and mice (Császár et al., 2022). Taking advantage of the nanometric resolution of SEM, I quantified the interactions microglia made with astrocytic endfeet and endothelial cells containing mitochondria associated with microglia membrane. There was no significant change in the average number of contacts between microglia and endothelial cells or astrocytic endfeet with proximal mitochondria (Table 7). However, the relative frequency of those microglia-

astrocytic endfeet mitochondrial interactions was significantly higher in the ipsi- LMol compared to contra- at 24 h (Figure 10J, p = 0.0418, Table 8).

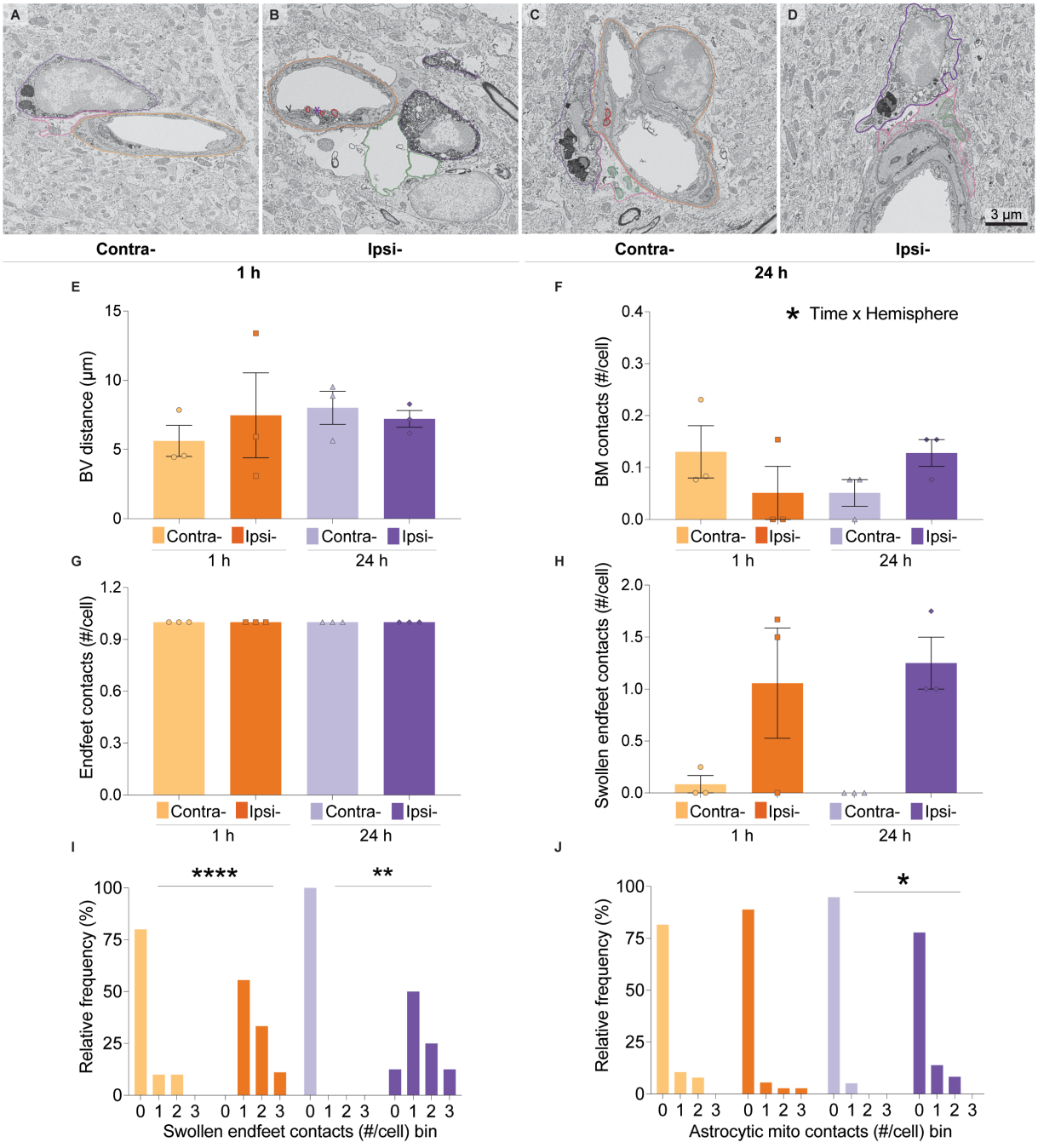

Figure 10. The frequency of interactions between microglia and the blood-brain barrier shifts at 1 and 24 hours following magnetic resonance imaging-guided focused ultrasound sonication with microbubbles in adult male mice *cornu ammonis 1 stratum lacunosum moleculare* microglia

A–D. Representative scanning electron microscopy (SEM) images of ionized calcium-binding adapter molecule 1 (Iba1) positive (+) cells and blood vessels in the ipsilateral (ipsi-) and contralateral (contra-) *stratum lacunosum moleculare* (*LMol*) 1 hours (h) and 24 h after magnetic resonance imaging-guided focused ultrasound sonication with microbubbles (MRIgFUS). Scale bar 3 μm. **E–H.** The average distance between microglia and blood vessels (**E**), the number of contacts between microglia and the basement membrane (**F**), astrocytic endfeet (**G**) and swollen astrocytic endfeet (**H**) did not change between the ipsi- and contra- *LMol* of adult male mice at 1 h and 24 h after MRIgFUS. Bar graphs show mean, standard error of the mean, as well as individual data points (n = 3 animals/hemisphere/timepoint) analyzed by a mixed-effects 2-way analysis of variance (ANOVA). **J.** However, the relative presence of contacts between microglia and swollen endfeet significantly increased in the ipsi- compared to contra- *LMol* 1 h and 24 h. **L**. In addition, the relative presence of microglial contacts with proximal astrocytic endfeet containing with mitochondria was similarly increased in the ipsi- *vs* contra- *LMol* at 24 h after MRIgFUS. Relative frequency bar graphs analyzed via Fisher's exact tests. SEM images are pseudocoloured as follows: purple - microglial cell body and process, orange – basement membrane, green - swollen astrocytic endfeet, red - endothelial cell mitochondria, purple asterisk - microglial process inside a blood vessel, pink - astrocytic endfeet, blue - mitochondria within astrocytic endfeet. $*p < 0.05$, $**p < 0.01$, $***p < 0.001$.

3.4.2. *Cornu ammonis 1 lacunosum moleculare* microglia change their interactions with pre-synaptic elements and extracellular space after magnetic resonance imaging-guided focused ultrasound sonication with microbubbles

Following systemic inflammation microglia interacted more with pre-synaptic elements in adult male mice (Savage et al., 2019). I verified whether interactions between microglia and synaptic elements, myelinated axons, degenerating myelin, extracellular space and extracellular digestion

were similarly altered at 1 h and 24 h after MRIgFUS in ipsi- *vs* contra- *LMol* (Figures 11A-D, Table 7). I did not find any significant differences in the average number of contacts between microglia and post-synaptic elements, neuronal cell body (satellite cells), myelinated axons, degenerating myelin, extracellular digestion and extracellular space (Figure 11G) (Table 7).

However, the average number of pre-synaptic elements contacted by microglial cell bodies significantly decreased throughout the 1 h and 24 h timepoints (Figure 11E, T main effect, F = 33.0600, p = 0.0004, C p = 0.0057, I p = 0.0091). To understand this change at the cell population level, the relative distribution of contacts with pre-synaptic elements was modeled by nonlinear regression (Table 9). There was a significant difference in microglia-pre-synaptic contact relative distribution curves between contra- and ipsi- at 1 h and 24 h (Figure 11F 1 and 24 h p = <0.0001). At both 1 h and 24 h, the pre-synaptic means were lower than the contra- fits, while the ipsi- pre-synaptic amplitude was higher at 1 h and lower at 24 h (Table 9). Overall, these results suggest cells tend to decrease their contacts with pre-synaptic elements at 1 h and 24 h after MRIgFUS (Table 9). As a result, the relative distribution of pre-synaptic interactions become less heterogenous at 1 h, with the reverse effect seen at the 24 h timepoint (Table 9).

I was also interested in assessing the relative frequency of contacts between microglial cell bodies and both neuronal and space elements. Correspondingly, microglia interacted less frequently with extracellular space pockets in the ipsi- *vs* contra- *LMol* at 24 h after MRIgFUS (Figure 11H, p =0.0040, Table 8), without significant differences in contacts with extracellular digestion (Table 8). Together, the reduction in contacts between microglia, pre-synaptic elements and extracellular space could impact rates of trogocytosis, important for synaptic plasticity (Weinhard et al., 2018). By contrast, the relative frequency of microglia adjacent to neuronal cell

bodies, myelinated axons and degenerating myelin did not change across the examined groups (Table 7). These results may indicate that the effect MRIgFUS has on microglia selectively affects pre-synaptic elements and not neuronal structures in general.

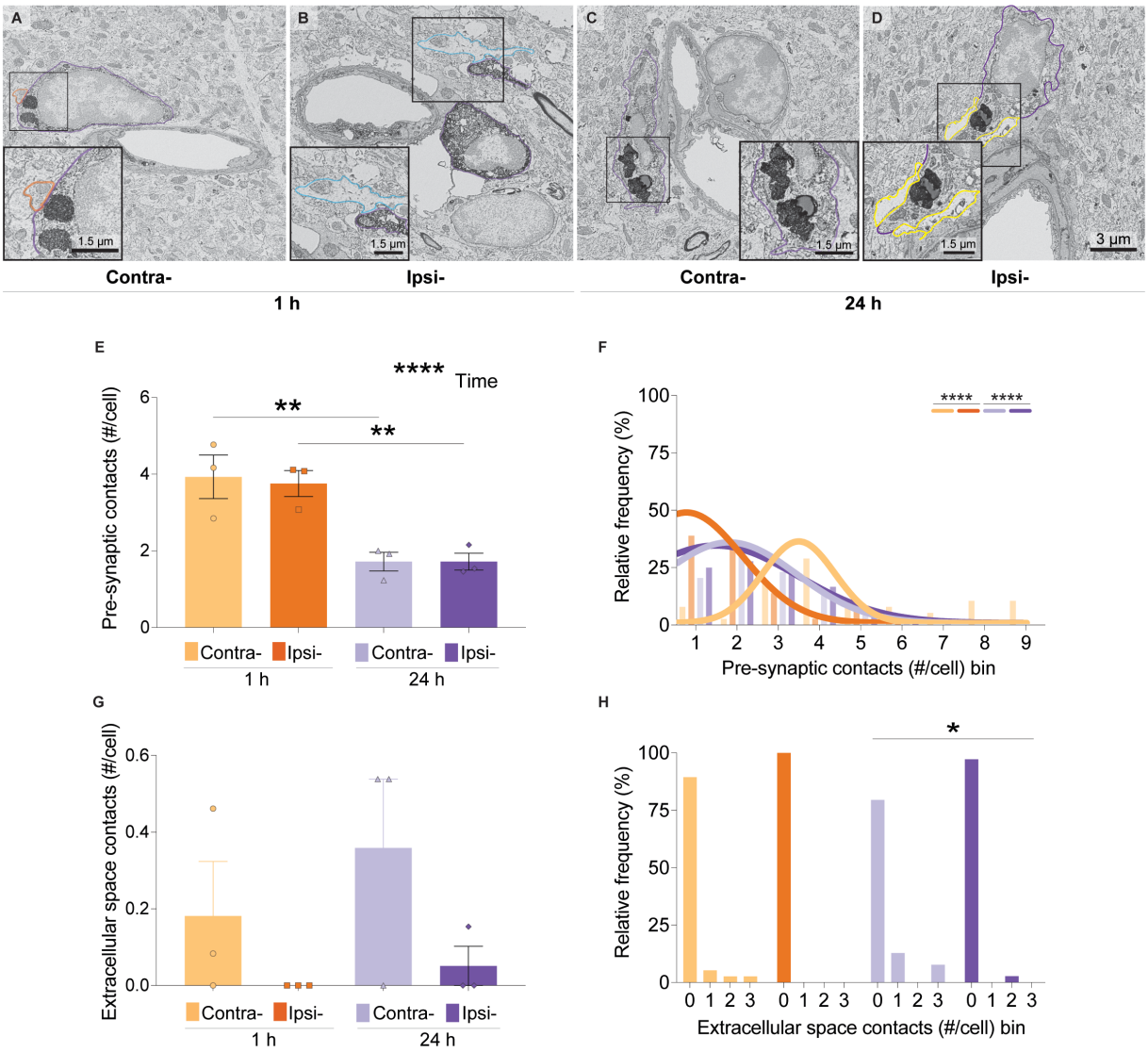

Figure 11. The microglia population shifts the frequency of their interactions with the pre-synaptic elements and extracellular space following magnetic resonance imaging-guided focused ultrasound sonication with microbubbles in the adult male mice cornu ammonis 1 stratum *lacunosum moleculare*.

A–D. Representative scanning electron microscopy (SEM) images of ionized calcium-binding adapter molecule 1 (Iba1) positive (+) cells and blood vessels in the ipsilateral (ipsi-) and

contralateral (contra-) *stratum lacunosum moleculare* (*LMol*) 1 hour (h) and 24 h after magnetic resonance imaging-guided focused ultrasound sonication with microbubbles (MRIgFUS). Insets highlight microglial contacts with pre-synaptic element (A), post-synaptic element (B) and extracellular space (D). Scale bars 3 (original images) and 1.5 (inset) μm. **E**. The average number of contacts between microglia and presynaptic elements significantly decreased 24 h after MRIgFUS in both ipsi- and contra- *LMol*. Bar graph shows mean, standard error of the mean, as well as individual data points (n = 3 animals/hemisphere/timepoint) analyzed by a mixed-effects 2-way analysis of variance (ANOVA) with Šídák's multiple comparisons tests. **F**. According to nonlinear regression modeling, the relative distribution of interactions between microglia and pre-synaptic elements was significantly distinct in the ipsi- *vs* contra- *LMol* at 1 h and 24 h after MRIgFUS. Histograms show the relative frequency and nonlinear regression analyzed via Wilcoxon comparison tests. **G**. The average number of interactions with extracellular space pockets did not differ in microglia 1 h or 24 h after MRIgFUS in the ipsi- *vs* contra- *LMol*. **J**. However, at 24 h, the relative frequency of contacts with extracellular space per microglial cell body decreased in the ipsi- *LMol* compared to the contra- control at 24 h. Histograms show the relative frequency analyzed by Fisher's exact tests. SEM images are pseudocoloured as follows: purple - microglia cell body and process, blue - post-synaptic terminal, orange - pre-synaptic element and yellow - extracellular space pocket. *$p < 0.05$, **$p < 0.01$, ***$p < 0.001$. #: number.

3.4.3. The distribution of endoplasmic reticulum/Golgi apparatus and mitochondria is altered in *cornu ammonis 1 lacunosum moleculare* microglia after magnetic resonance imaging-guided focused ultrasound sonication with microbubbles

The ultrastructural state of organelles can inform whether microglia are undergoing cellular stress, which could occur because of elevated BBB permeability (Savage et al., 2018). I quantified the average number of ER/Golgi, dilated ER/Golgi, ER/Golgi and mitochondrial proximity events, as well as homeostatic, dystrophic and elongated mitochondria within microglial cell bodies at 1 and 24 h after MRIgFUS in the ipsi- *vs* contra- *CA1 LMol* (Figure 12A-D). The average number of ER/Golgi (Figure 12E), dilated ER/Golgi cisternae, ER and

mitochondrial proximity events were not significantly altered across all groups (Table 7). However, I identified a significant main effect of the hemisphere on the number of homeostatic (Figure 10G, H F = 17.3200, p = 0.0141) and dystrophic (Figure 10K, H F = 5.5910, p = 0.0456) mitochondria per microglia.

To detect more subtle differences within the population, I also investigated the relative distribution of ER/Golgi and mitochondria using nonlinear regression models. I identified a significant difference in the nonlinear regression curves of ipsi- *vs* contra ER/Golgi (Figure 12I, 1 and 24 h p = <0.0001), mitochondria (Figure 12J, 1 and 24 h p = <0.0001) and elongated mitochondria (Figure 12K, 1 and 24 h p = <0.0001). The ipsi- mean of ER/Golgi was increased at 1 h and 24 h after MRIgFUS, but the amplitude was higher at 1 h and lower at 24 h (Table 9). The ipsi- mean of elongated mitochondria increased at 1 h and decreased at 24 h, while the opposite relationship applied to the amplitude (Table 9). Moreover, the ipsi- mean of mitochondria was reduced at 1 and 24 h, with the reverse effect for the amplitude (Table 9). Overall, the relative distribution of cells with more ER/Golgi, elongated mitochondria increased, but homeostatic mitochondria reduced at 1 h MRIgFUS (Table 9). Following 24 h, the number of ER/Golgi continue to increase, while both homeostatic and elongated mitochondria decreased at 24 h (Table 9). As a result, at 1 h, the heterogeneity of ER/Golgi and mitochondria distribution decreased, whereas for elongated mitochondria it increased (Table 9). At 24 h, the distribution heterogeneity for ER/Golgi elevated while for mitochondria and dystrophic mitochondria it lowered (Table 9).

Moreover, I was also interested in exploring if the relative frequency of microglial cell body with dilated ER/Golgi and dystrophic mitochondria changed between our groups. I identified that microglia with dystrophic mitochondria were more frequent in the ipsi- *vs* contra-

LMol at 24 h after MRIgFUS (Figure 12L, $p = 0.0040$), while there was no change for dilated ER/Golgi and ER/mitochondria contacts per cell (Table 8).

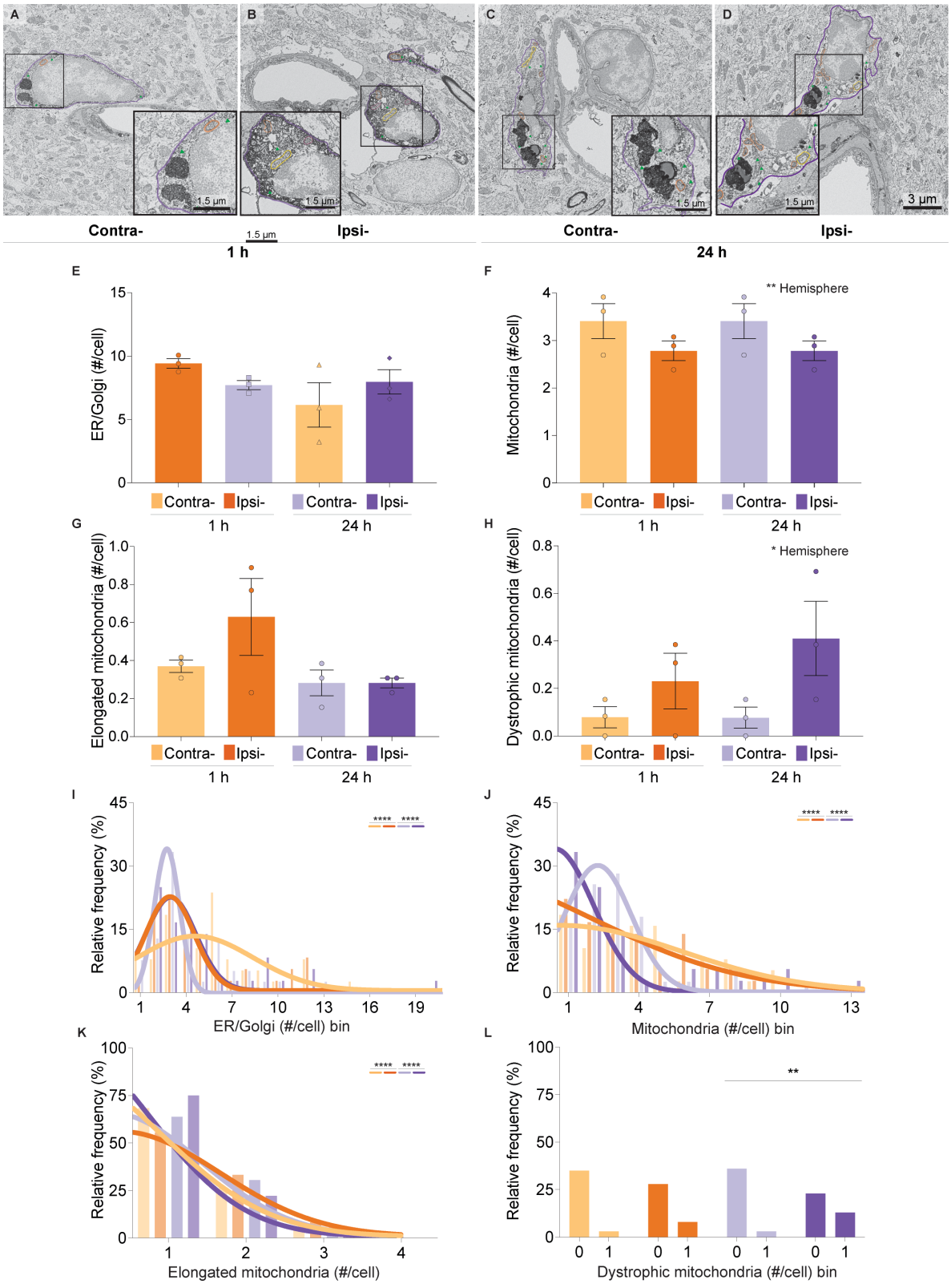

Figure 12. The microglia population shifts their distribution of endoplasmic reticulum/Golgi apparatus and mitochondria per cell following magnetic resonance imaging-guided focused ultrasound in the adult male mice *cornu ammonis 1 stratum lacunosum moleculare* ventral hippocampus.

A–D. Representative scanning electron microscopy (SEM) images of ionized calcium-binding adapter molecule 1 (Iba1) positive (+) cells and blood vessels in the ipsilateral (ipsi-) and contralateral (contra-) *stratum lacunosum moleculare* (*LMol*) 1 hour (h) and 24 h after magnetic resonance imaging-guided focused ultrasound sonication with microbubbles (MRIgFUS). Insets highlight microglia mitochondria and endoplasmic reticulum/golgi apparatus (ER/Golgi) (**A**), elongated and dystrophic mitochondria (**B**). Scale bars 3 (original images) and 1.5 (inset) μm. **E–-H**. The average number of microglia ER/Golgi (**E**), mitochondria (**F**), elongated mitochondria (**G**) and dystrophic mitochondria (**H**) did not change at 1 h and 24 h after MRIgFUS in the ipsi- and contra- *LMol*. Bar graphs show mean, standard error of the mean, as well as individual data points (n = 3 animals/hemisphere/timepoint) analyzed by a mixed-effects 2-way analysis of variance (ANOVA). **I-K.** However, according to the nonlinear regression models, the relative frequency of ER/Golgi (**I**), mitochondria (**J**) and elongated mitochondria (**K**) varied in the ipsi- *vs* contra- *LMol* at 1 and 24 h. **L**. Histograms show the relative frequency and nonlinear regression analyzed via Wilcoxon comparison tests. The number of dystrophic mitochondria per cell was significantly distinct between ipsi- and contra- *LMol* at 24 h. The relative frequency was analyzed *via* Fisher's exact tests. SEM images are pseudocoloured as follows: purple - microglial cell body and process, green arrowhead - ER/Golgi, orange - dystrophic mitochondria, pink - homeostatic mitochondria and yellow: elongated mitochondria. $*p < 0.05$, $**p < 0.01$, $***p < 0.001$. #: number.

3.4.4. The distribution of primary and secondary lysosomes is altered in *cornu ammonis 1 lacunosum moleculare* microglia after magnetic resonance imaging-guided focused ultrasound sonication with microbubbles

Increased phagolysosomal activity is often a hallmark of inflammatory processes and is observed in mouse models of AD following MRIgFUS (Jordão et al., 2013). Currently, it is unclear if a similar effect would occur in wild-type mice treated with MRIgFUS. I investigated this question

by quantifying the number of empty and filled phagosomes, autophagosomes and primary, secondary and tertiary lysosomes within the cell body of microglia in the contra- and ipsi- *LMol*. I did not find any significant differences in the average number and relative frequency of empty and filled phagosomes (Tables 7 and 8), autophagosomes (Tables 7 and 8) and tertiary lysosomes (Figures 13G, Tables 7 and 8) in contra- and ipsi- *LMol* at 1 h and 24 h following MRIgFUS. However, there was significantly fewer primary lysosomes per microglia (Figure 13E, Time *vs* Hemisphere F = 12.720 and $p = 0.0235$, 24 h $p = 0.0368$ and t = 3.8340) and fewer microglial cell bodies with primary lysosomes (Figure 13H, $p = 0.0259$) at 24 h in the ipsi- *vs* contra- *LMol*. In addition, I observed a significant interaction effect for the average number of secondary lysosomes per microglia (Figure 13F Time *vs* Hemisphere F = 8.6430, $p = 0.0424$) with a significant decrease in the number of cells with secondary lysosomes at 24 h (Figure 13I, $p = 0.0379$) and no impact on tertiary lysosomes (Figure 13J). This suggests that the lysosomal activity of cells decreased after MRIgFUS.

3.4.5. *Cornu ammonis 1 lacunosum moleculare* microglia ultrastructure correlates with vessel proximity and area after magnetic resonance imaging-guided focused ultrasound sonication with microbubbles

Vessels with diameter of 10–30 μm had a higher density of transcytosis than capillaries (< 10 μm of diameter) after MRIgFUS (Sheikov et al., 2006). To investigate whether vessel proximity and diameter play a role in modulating the nanometric parameters I analyzed in the ipsi- *LMol* microglia ultrastructure dataset, I performed a Spearman r correlation including both timepoints (Figure 144, Table 11). Vessel area did not correlate with microglial blood vessel proximity (Figure 144, Table 11). However, blood vessel distance significantly and negatively correlated with interactions between microglia and astrocytic endfeet (Figure 14A, r = -0.7330, $p =$

<0.0001), swollen astrocytic endfeet (Figure 14A, r = -0.3126, $p = 0.0019$) and the basement membrane (Figure 14A, r = -0.4722, $p = <0.0001$). Moreover, I observed a significant positive correlation between vessel area and interactions between microglia and astrocytic endfeet (Figure14A, r = 0.3624, $p = <0.0001$), swollen astrocytic endfeet (Figure 14A, r = 0.3072, $p = 0.0001$), the basement membrane (Figure 14A, r = 0.1793, $p = 0.0276$) and endothelial cells containing mitochondria (Figure 14A, r = 0.1800, $p = 0.0270$). Altogether, these results suggest that microglia increase their interactions with bigger vessels after MRIgFUS.

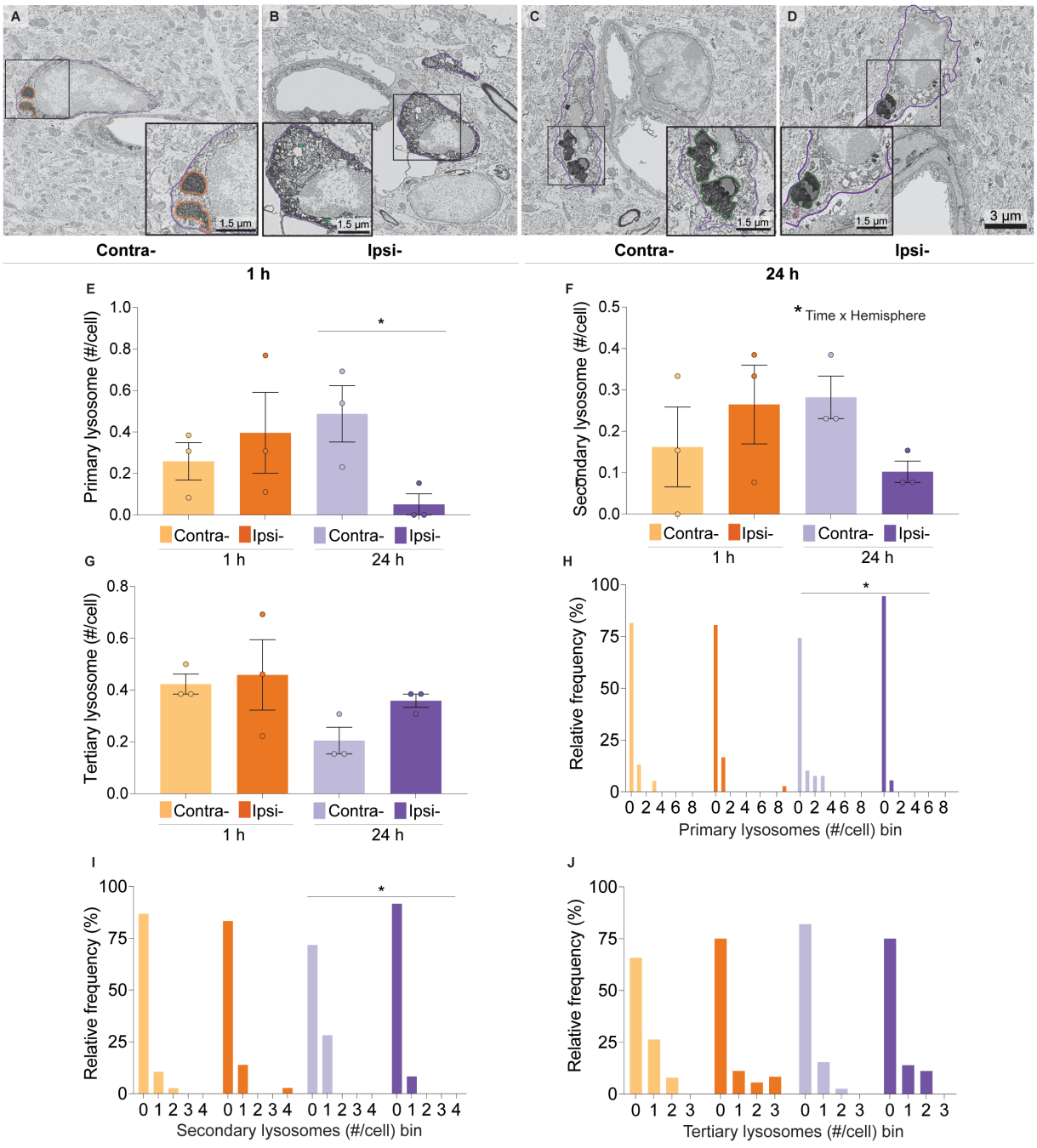

Figure 13. The microglial population shifts its distribution of lysosomes following magnetic resonance imaging-guided focused ultrasound in the adult male mice *cornu ammonis 1 stratum lacunosum moleculare* ventral hippocampus.

A–D. Representative scanning electron microscopy (SEM) images of ionized calcium-binding adapter molecule 1 (Iba1) positive (+) cells and blood vessels in the ipsilateral (ipsi-) and contralateral (contra-) *stratum lacunosum moleculare* (*LMol*) 1 hour (h) and 24 h after magnetic resonance imaging-guided focused ultrasound sonication with microbubbles (MRIgFUS). Insets highlight primary (**D)**, secondary (**A**) and tertiary (**D**) lysosomes. Scale bars 3 (original images) and 1.5 (inset) μm. **E.** The average number of primary lysosomes was significantly decreased in the ipsi- *vs* contra- *LMol* 24 h after MRIgFUS. **G.** A significant interaction effect was observed for the average of secondary lysosomes between ipsi- and contra- *LMol*. **I.** The average number of tertiary lysosomes did not change between ipsi and contra- *LMol* at 1 h and 24 h. Bar graphs show mean, standard error of the mean, as well as individual data points (n = 3 animals/hemisphere/timepoint) analyzed by a mixed-effects 2-way analysis of variance (ANOVA) with Šídák's multiple comparisons tests. **H–J**. However, the relative frequency of primary **(H)** and secondary lysosomes ER/Golgi (**I**) were significantly different between ipsi- and contra- *LMol* at 24 h after MRIgFUS, with no changes in tertiary lysosomes (**J**). Histograms show relative frequencies analyzed via Fisher's exact tests. SEM images are pseudocoloured as follows: purple outline - microglial cell body and process, pink: primary lysosome, orange - secondary lysosome, green: tertiary lysosome. $*p < 0.05$, $**p < 0.01$, $***p < 0.001$.

3.4.6. *Cornu ammonis 1 lacunosum moleculare* microglia ultrastructure is more variable at 24 hours after magnetic resonance imaging-guided focused ultrasound sonication with microbubbles

Modifications in the contacts microglia make with the blood vessels and neuropil happen simultaneously to changes in their organelles. To address this multidimensionality within the ultrastructure dataset, I explored how each of 30 ultrastructural variables related to one another and with the MRIgFUS using a PCA (Table 10). The analysis selected three PC, with PC1 explaining 13.78% and PC2 11.05% of the variations in the dataset (Table 10). The distribution

of data points in the PC1 and 2 was more dispersed in the ipsi- *LMol* at 24 h, compared to the other groups, suggesting that most variability in the ultrastructure dataset came from cells in the targeted *LMol* at 24 h following MRIgFUS (Figure 14B). Moreover, the loadings of variables for the PC1 and PC2 (Figure 14C) indicated that across all variables, parameters such as number of contacts between microglia and astrocytic endfeet, swollen endfeet, basement membrane, along with alterations in ER/Golgi and mitochondria most strongly correlated with variation within PC1 and PCA2 (Figure 14C and Table 10).

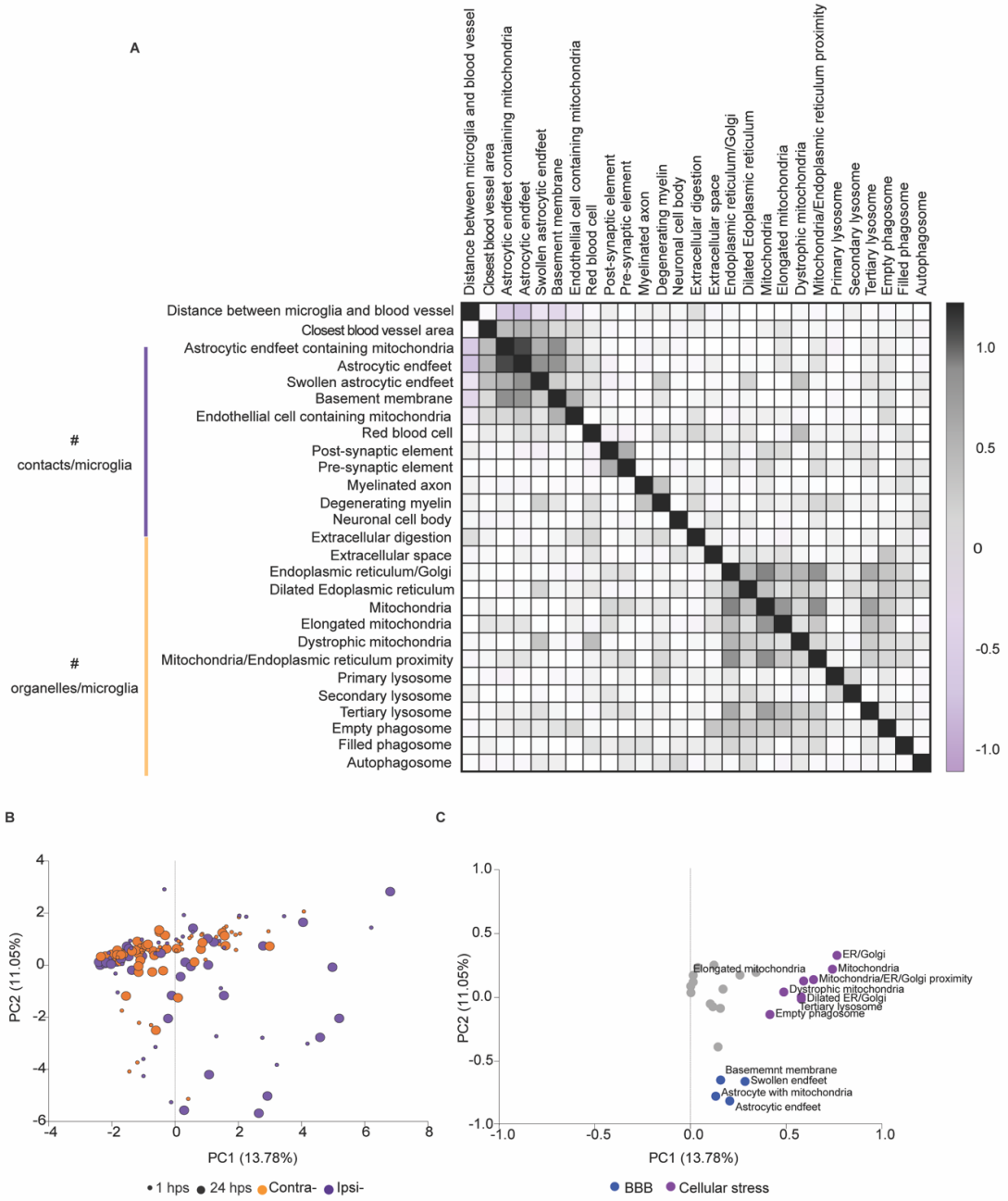

Figure 14. The microglial ultrastructure varies with magnetic resonance imaging-guided focused ultrasound sonication with microbubbles in the adult male mouse ventral *cornu ammonis 1 stratum lacunosum moleculare*.

A. The microglial distance from blood vessels was negatively correlated, while vessel area was positively correlated with changes in microglia contacts with astrocytic endfeet, swollen astrocytic endfeet, basement membrane and endothelial cell containing mitochondria in the ipsilateral (ipsi-) *stratum lacunosum moleculare* (*LMol)* at 1 and 24 hours (h) following magnetic resonance imaging-guided focused ultrasound (MRIgFUS). Correlation matrix of ipsi- features analyzed by Spearman r. **B**. Scores for the first and second principal components 1 and 2 (PC1/PC2) of ultrastructural features analyzed, colored according to the *LMol* hemisphere (orange: contra-, purple: ipsi-) and timepoint (small icon: 1 h, big icon: 24 h). A higher variability in parameters is present at 24 h, particularly in the ipsi- *LMol*. **C**. Loading plot of ultrastructural dataset, depicting the correlation between the ultrastructural features (orange: microglial cellular stress, purple: microglial contacts with the blood-brain barrier or BBB) and PC1/PC2, suggesting that most adaptations between ipsi- and contra- *LMol* ionized calcium-binding adapter molecule 1 (Iba1) positive (+) cells in the scanning electron microscopy dataset arise from interactions with BBB and cellular stress.

CHAPTER 4: DISCUSSION

In this thesis, I characterized the short-term baseline responses of microglia to MRIgFUS in the *CA1* of adult male mice. Significantly, I show that MRIgFUS causes evasion of IgG from the blood into the hippocampal parenchyma at 1 h and 24 h. In the treated *CA1*, this extravasation correlated with the proximity of microglia, despite a lack of difference in overall microglial density between treated and non-treated *CA1* at 1 h and 24 h. Moreover, I found that, while collectively *LMol* microglia increase their soma perimeter after MRIgFUS, additional changes in soma, cell body and arborization parameters occur only in a subset of microglia and relate to a rod-like shape, associated with injury. At 1 h and 24 h after MRIgFUS, microglia do not alter their distance to blood vessels in the ipsi- *LMol,* but increase their interactions with the BBB according to vessel area. This vessel-dependent response could help explain the frequent contacts between microglia and swollen astrocytic endfeet I observed. By contrast, MRIgFUS induces less frequent interactions between microglia, pre-synaptic elements and extracellular space, which could reduce trogocytosis, necessary for synaptic plasticity. Collectively, my thesis provides the first ultrastructural characterization of microglia after MRIgFUS with findings that support the application of this technology.

4.1. Hippocampal evidence of increased blood-brain barrier permeability is found at 1 and 24 hours after magnetic resonance imaging-guided focused ultrasound sonication with microbubbles

My first main goal was to verify the BBB permeability in the ipsi- *vs* contra- hemispheres. To this end, I first looked at the MR contrast agent leakage into the parenchyma, using T1-weighted images. Infiltration of gadolinium could be observed in all ipsi-, but not in the contra-hemispheres. This was supported quantitatively by a significantly elevated average voxel

intensity in the ipsi- *vs* the contra ventral hippocampus. Gadolinium parenchymal leakage has long been used to infer increased BBB permeability (Hynynen et al., 2001), but it is important to note that this metric is highly dependent on the contrast agent dosage and the timing of MR imaging. It follows that, albeit being a clear indicator of an elevated BBB permeability, the voxel intensity is not a direct measurement of the extent of the leakage (Aubert Lab, personal communication).

An alternative to this limitation is to measure BBB permeability directly in the brain sections. Previous research has detected elevated IgG and IgM staining at 4 h and 4 days following MRIgFUS in the treated ipsi- treated *vs* nontreated contra- nontreated hemisphere of an AD pathology (TgCRND8) mouse model (Jordão et al., 2013). I hypothesized that MRIgFUS BBB modulation in homeostatic conditions would similarly increase the blood efflux of endogenous Igs into the mouse brain parenchyma, supporting the MR contrast agent findings. In agreement with this hypothesis, endogenous IgG was found only in the ipsi- hippocampus. IgG staining could be detected in the hippocampal parenchyma, specifically alongside structures that—based on their cylinder structure—resemble blood vessels at both 1 and 24 h timepoints. IgG could be clustering around the parenchymal face of the BBB, prior to slowly pervading the extracellular matrix after MRIgFUS. Higher resolution microscopy, for instance, volume electron microscopy using BBB markers, such as platelet/endothelial cell adhesion molecule, 1 (Pecam1) or Aqp4 would help to test this hypothesis (Carrier et al., 2020; Császár et al., 2022). Specifically, focused ion beam scanning electron microscopy (FIB-SEM) would allow for reconstruction of IgG in the luminal and abluminal portions of the vessel, offering a volumetric characterization that removes possible biases of the plane of cutting (Carrier et al., 2020; Császár et al., 2022).

In addition, the IgG staining revealed that different Bregma levels within each timepoint, specifically across animals, had varied extents of IgG infiltration. This happened despite maintaining the exact same immunohistochemistry protocol across all samples. A possible explanation would be that MRIgFUS targeting shifted slightly within the ventral hippocampus of each animal. On the other hand, this observation illustrates the importance of verifying that increased BBB permeability can be detected in each tissue section prior to drawing further conclusions around MRIgFUS.

Likewise, the IgG variability alerted us to another possible confounder: brain region (Meng et al., 2021). Distinct brain areas harbor different cell populations, with varying densities, distributions and vascular connections (Keller et al., 2018), a fact that is markedly true for microglia (Tan et al., 2020). When assessing the hippocampus, each subfield has distinct neuronal inputs and outputs, as well as microglial properties. For example, the ventral *CA1* is estimated to have double of the *CA3* microglial density (Keller et al., 2018). To account for a regional impact of MRIgFUS, I first analyzed the IgG distribution in the entire *CA1* and then in each individual *CA1* layer. I hypothesized that the *LMol* would be likely more affected by MRIgFUS primarily due to an abundance of larger vessels, an anatomical feature of this subregion. Indeed, visual inspection of IgG staining was confirmed in all ipsi- *CA1 LMol* at 1h and 24 h, but only at 24 h for *Rad*, *Py* and *Or*. Moreover, to provide an estimation of the IgG in each *CA1* strata across the two hemispheres and timepoints, I carried out an optical density analysis, which showed IgG varied across time in the *LMol* but not the remaining strata (Bordeleau et al., 2021).

A previous study detected endogenous Igs starting at 4 h and lasting up to 4 days after MRIgFUS in an AD pathology model (Jordão et al., 2013). The elevated detection of IgG

staining at 24 h *vs* at 1 h is a novel finding and stimulates new questions, especially considering that induced BBB permeability decreases with time and is mostly resolved 6 h after MRIgFUS (Meng et al., 2021). On the other hand, it could reflect that the rate of elimination of IgG is slower in comparison to its infiltration. Studies, however, have suggested that this process is resolved after a few days, since Igs are no longer detectable in the brain of an AD pathology model at 7 days following MRIgFUS (Dubey et al., 2020; Jordão et al., 2013).

However, it is important to note that optical density analysis has limitations. Firstly, although visually the IgG parenchymal staining was clearly discernible from the Iba1+ microglia/macrophage cell bodies and processes, both were revealed using immunoperoxidase reactions. These could not be dissociated by spectral separation nor detected separately through brightfield microscopy, as typically done for immunofluorescence, where channels can be imaged and quantified individually (Carrier et al., 2020). As a result, it is possible that the changes I observed in optical density reflect both IgG and Iba1. A way to corroborate our results would be micro dissect the *CA1* and assess IgG expression using Western blot (Dubey et al., 2020; Jordão et al., 2013). Notably, an immunofluorescence-based method was not compatible with our samples due to high background produced by acrolein, the fixative used to guarantee highest ultrastructural integrity. Alternatively, the double immunoperoxidase staining was advantageous because it allowed further processing of stained samples with electron microscopy, which ensured that imaged regions pertained to sections in which increased BBB permeability was confirmed.

4.2. Microglia change at the microscale in response to magnetic resonance imaging-guided focused ultrasound sonication with microbubbles

The entry of blood-borne molecules into the brain alerts cells in the vicinity to produce inflammatory cues, such as cytokines and chemokines, which broadly signal to the immune system the need to mount an acute response (McMahon & Hynynen, 2017). Microglia are particularly equipped with receptors that recognize inflammatory signals, including those that are blood-derived. Indeed, stereotaxic injection of blood plasma into the brain of wild-type mice elicited specific gene expression associated with the detection of fibrinogen and complement proteins (Mendiola et al., 2023). The idea that microglia are largely sensitive to blood-derived molecules in the parenchyma prompted me to ask if increased BBB permeability at 1 h and at 24 h following MRIgFUS would impact their density and distribution in the ventral *CA1* of adult male mice. Considering that I observed IgG staining more frequently in the *CA1 LMol* as compared to other *CA1* strata, I hypothesized this hippocampal layer would be most impacted. I did not identify significant differences in the number, distribution or cluster formation of microglia in *CA1 LMol* between contra- and ipsi- hemispheres. Nonetheless, I detected a main effect of time in modulating the overall distance between cells, or NND, in the *CA1* as a whole, though not within a specific layer. While post-hoc analysis comparing contra- *vs* ipsi-hemispheres and 1 h *vs* 24 h did not return any significance, the *CA1* NND averages were smaller in ipsi- *vs* contra- hemispheres. A significantly reduced NND of microglia was observed 7 days after FUS+MB targeting the hippocampus of male mice (Silburt & Aubert, 2022). I speculate that microglia could start shifting their proximity at 1 h following MRIgFUS, although significant differences are potentially only observable after 24 h.

On the other hand, it is also possible that changes in microglial organization occur in proportion to the extent of blood molecules extravasation into the CNS. To evaluate possible relationship between BBB permeability and microglia placement in brain parenchyma after MRIgFUS, I examined if the IgG staining correlated with changes in the number and distribution features of microglia. After performing a Spearman r correlation of microglial cell and cluster density, NND, and spacing index in the ipsi- *CA1* at 1 h and 24 h after MRIgFUS, I observed a significant negative correlation between optical density and microglial density and a positive correlation between optical density and NND at both timepoints. These relationships converge with my overarching hypothesis that blood vessel leakage drives changes in microglial distribution (Lou et al., 2016). Previously, Iba1+ cells migrated toward blood vessels 2 days after FUS+MB treatment in the prefrontal cortex of adult non-human primates, although the same effect was not observed in later timepoints (18 days) (Jordão et al., 2013; Pouliopoulos et al., 2021). To further characterize this microglia-vessel leakage relationship, a longitudinal analysis of microglia and blood vessels during the hours and days following MRIgFUS, for example, using *in vivo* two-photon microscopy, would be relevant to conduct (McMahon & Hynynen, 2017; Poon et al., 2021).

Simultaneously with a change in distribution, binding of microglial cell membrane receptors to blood-evading antigens can promote modifications in morphology that support inflammation resolution (Dungrawala et al., 2010; Kozlowski & Weimer, 2012; Marguerat & Bähler, 2012; Mendiola et al., 2023). At 7 days after MRIgFUS, soma area of microglia was previously found to be significantly increased in cells adjacent to the targeted area within the hippocampus of male mice (Silburt & Aubert, 2022). I hypothesized that a similar response would occur early-on after MRIgFUS. To assess this, I manually traced the cell body of Iba1+

cells in the *CA1 LMol*, where a high prevalence and temporal variation of IgG + staining was observed, as previously mentioned. The tracing was used to measure the soma area, perimeter, aspect ratio, solidity, circularity and roundness, which were overall similar between ipsi- *vs* contra- *LMol* at 1 h and 24 h. The only exception was soma perimeter, which significantly increased in the ipsi- compared to the contra- *LMol* at 24 h after MRIgFUS.

An increase in perimeter that is not accompanied by changes in area could indicate a more elongated soma shape, reminiscent of rod microglia (Vidal-Itriago et al., 2022). The latter are a morphological state with a narrow, elongated soma, that typically organizes in a specific orientation along multiple cells, i.e., trains of rod cells (Vidal-Itriago et al., 2022). It has been proposed that microglia adopt this morphology to shield dendrites and axons after traumatic brain injury in adult male rats (Ziebell et al., 2012), which could occur following MRIgFUS. The rod-morphology, although detected in the *LMol,* would be in line with the decreased distance between microglia at 24 h *vs* 1 h, observed in the *CA1*. After optic nerve transection, retinal ganglion degeneration was similarly associated with microglia possessing a rod morphological state presenting with high phagocytic activity and local proliferation in adult male rats (Yuan et al., 2015). This indicates that there would be important functional outcomes to more rod-like cells in the *LMol* after MRIgFUS. While we did not observe significant changes in density and number of phagosomes in *LMol* microglia, it would be interesting to explore if similar effects occur in the *CA1* as a whole, which we explore in the 4.4 section.

In addition to investigating the averaged differences between animals, I was also interested in characterizing the relative distribution of microglial morphological states between the ipsi- and contra- *LMol* at 1 h and 24 h after MRIgFUS, to determine if specific subsets of microglia might be differentially responsive to MRIgFUS (Paolicelli et al., 2022; Stratoulias et

al., 2019). To this end, I utilized nonlinear regression models, which estimate the values that best fit a curve to the observed data and can be used to explain the possible relationship between the values of dependent and independent variables (Motulsky & Ransnas, 1987). By taking advantage of this model, I observed that the significant changes in the relative distribution of soma area, perimeter, aspect ratio, solidity and roundness were in agreement with cells adopting a more rod-like shape in the ipsi- *vs* contra- *LMol* at both 1 h and 24 h. This response increased with time, resulting in a more heterogeneous distribution of ipsi- cell body morphology at 24 h. As a result, I propose that specific *CA1 LMol* microglial states are more responsive to MRIgFUS BBB modulation at 1 h and 24 h. To test this idea, studies isolating microglia from hippocampal tissue targeted by MRIgFUS and analyzing their gene and protein expression in terms of cellular stress intermediates could be helpful (Mendiola et al., 2023). Moreover, I speculate that shifting the microglial cell body morphology to a rod state aids in the response to MRIgFUS. This could be verified by conjugate fluorescence tomography, analyzing *in situ* the expression of markers such as CD68 in relation to the cell morphology and MRIgFUS.

Rod microglia display thin processes, mainly in the apical and basal ends of the cell, that may associate with reduced microglial surveillance activity, otherwise required for proper brain function (Savage et al., 2019). Next, I examined the territory (manual convex shape), arbor (semi-automated arbor), shape complexity (fractal analysis) and ramification of *LMol* microglia (De Felice et al., 2022; González Ibanez et al., 2019), to infer if the changes in the soma are followed by alteration in the processes. The average microglia convex shape and automated cell area, aspect ratio, perimeter, roundness, circularity, solidity, fractal dimension and lacunarity did not change between the ipsi- and contra- *LMol* at 1 h and 24 h following MRIgFUS. Similarly, no differences were found in the number of branches, junctions, and lengths of the longest or

shortest branch per cell. Overall, this suggests that microglia retain their initial morphology at 1 h and 24 h after MRIgFUS. However, this analysis took in consideration *LMol* microglia population as a whole, without addressing their diversity.

Accordingly, I thereafter explored whether specific states within the population of microglia in the *LMol* were more morphologically responsive in terms of changes in processes to MRIgFUS. To this end, I followed the same approach as described above, whereby the relative frequencies of each parameter across the ipsi- and contra- *LMol* at 1 h and 24 h were modelled through nonlinear regression fits. Notably, the results revealed a complex response. At 1 h, the significant changes in ipsi- nonlinear regression fits indicated a shift toward cells with a smaller, less round and complex arbor, that had more branches and an elongated and rounder territory. At 24 h, cells continued to shift toward a smaller territory, arbor roundness, perimeter, but had reduced ramification, elevated area, elongation and arbor complexity. The observation that territory elongation increases at 1 h could support the rod-like state mentioned before, however, it is more probable that cells adopt more than one arbor morphology in response to MRIgFUS (Šimončičová et al., 2022). Notably, for most shape descriptors, the ipsi- distribution of microglial arbor heterogeneity increased at 1 h, but decreased at 24 h. I speculated that this represents specific microglial states changing their morphology in response to elevated BBB permeability at 1 h but returning to baseline at 24 h following MRIgFUS. However, after visually inspecting the spread of ipsi- and contra- cell datapoints across all morphological variables via a principal component analysis, the variability seems to only increase between the 1 h and 24 h timepoints in the ipsi- group, which contradicted, at least in part, a return to baseline. A more conservative conclusion from the morphological findings, therefore, is that the relative distribution of morphological parameters varies in the ipsi- *LMol* in contrast to the contra-

control at both 1 h and 24 h following MRIgFUS. Antibody multiplexing investigating *in situ* spatial morphology of microglia in relation to stained, infiltrated molecules would be interesting as a future direction (Shahidehpour et al., 2023). In this regard, it would be important to establish thresholds for shape descriptors that correspond to different morphological states, in lieu of simply assessing ameboid *vs* ramified (Šimončičová et al., 2022).

Contrary to my overarching hypothesis, there was no correlation between IgG optical density and the morphological dataset in the ipsi- hemisphere at 1 h and 24 h following MRIgFUS. This could suggest that morphological shifts after MRIgFUS are independent of IgG *per se*, although requiring direct measurement of this molecule, for instance, with Western blotting, to confirm. A previous study suggested that albumin, in particular, affected microglial phagocytosis in an AD pathology mouse model following a scanning modality of FUS+MB (Leinenga & Götz, 2015). Recently, Mendiola, AS *et al* (2023) used stereotaxic injection of blood plasma into the brain of wild-type mice to investigate how the transcriptome of microglia can be affected by an increased BBB permeability. Using mice that do not express a receptor for the blood coagulation factor fibrinogen, the authors show that increased infiltration of fibrinogen has a direct relationship to disease-associated transcriptomic profiles in microglia (Mendiola et al., 2023). A modified version of this experimental paradigm could be used to study the specific molecules that alter microglial morphology after MRIgFUS. For instance, targeting mice without purinergic, complement or immunoglobulin receptors, and verifying their morphological response, in addition to -omic analysis of inflammatory, cellular stress and scavenger pathways (Dumas et al., 2021).

Lastly, it is important to note that there are several constraints in the aforementioned analysis. Firstly, functional inferences from morphology results are limited, particularly in 2D

images such as those obtained with brightfield imaging, where the tissue planes are superimposed and may lead to simplification of overall volume arborization (Carrier et al., 2020; Green et al., 2020). On the other hand, brightfield microscopy provided the advantage of more sensitive peroxidase staining with much less background compared to immunofluorescence techniques, which allowed us to correlate light with electron microscopy findings, as outlined below. Moreover, though the same applies to any post-mortem investigation, the microglial morphologies identified in my analysis reflect the cell shape at the time of tissue fixation (Gonçalves de Andrade et al., 2022), when *in vivo* microglia are dynamic, constantly remodeling their process morphology. In this context, *in vivo* studies such as 2-photon microscopy performed in awake mice, would allow recording of the cell shape longitudinally, more accurately dissecting dynamic changes in the shape and form of microglia (Carrier et al., 2020) following MRIgFUS. Lastly, it is fundamental to point out that the nonlinear regression fits herein used provide an approximate comparison between the relative distribution of each variable. To confirm our results and provide morphological clusters across multiple variables, more sophisticated hierarchical clustering and PCA analyses would be encouraged (Silburt & Aubert, 2022; van Weering et al., 2023).

4.2. Microglia change their interactions with the blood-brain barrier at the nanoscale level in response to magnetic resonance imaging-guided focused ultrasound sonication with microbubbles

The first three-dimensional electron microscopy (3DEM) reconstruction of microglia showed that, from a small cell body volume of under 200 μm^3, 10 branches and over 200 filopodia can emerge to scan the hippocampal parenchyma of an adult male mice (Bolasco et al., 2018). Part of these contacts are dedicated to preserve BBB homeostasis (Bisht et al., 2016; Joost et al., 2019).

Accordingly, BBB permeability has been shown to attract microglia toward blood vessels, both in the context of MRIgFUS at day 2 in macaques (Pouliopoulos et al., 2021), but also in multiple studies investigating chronic and acute models of inflammation (Bowyer et al., 2020; Császár et al., 2022; Erickson et al., 2023; Haruwaka et al., 2019; Joost et al., 2019). However, in the superior frontal gyrus of individuals with AD, microglia, instead, reduced their association with pericytes and capillaries (Morris et al., 2023). Taking advantage of state-of-art, nanometric resolution, scanning electron microscopy, I was drawn to investigate the specific interactions between microglia cell bodies and BBB components in the ipsi- *vs* contra- *CA1 LMol*, of adult male mice at 1 h and 24 h following MRIgFUS. Notably, these contacts contributed to high variability in the ultrastructure dataset, as indicated by PCA. I did not find significant differences in the average distance or number of microglia associated with blood vessels at 1 h and 24 h after MRIgFUS, although different results could be found if restricting the analysis per vessel type (arteriole, venule, capillary) or diameter.

Vessels with bigger diameter (10–30 μm) had a higher density of transcytosis than capillaries (< 10 μm) after MRIgFUS (Sheikov et al., 2006). To interrogate if vessel size had a particular effect on microglia following BBB permeability, I next examined if any of the variables included in the ultrastructure analysis correlated with the distinct vessel areas observed among the ipsi- *LMol* at 1 h and 24 h after MRIgFUS. Significantly, I did observe a positive correlation between vessel area and interactions between microglia and astrocytic endfeet, swollen astrocytic endfeet and basement membrane. These findings suggest that after MRIgFUS, bigger vessels were more likely to be contacted by microglia. It is possible that a proportional relationship between vessel area and inflammation exists after MRIgFUS, which would explain the increased microglial-vessel association. It would be important to interrogate this relationship

further, perhaps sampling an analysis based on both microglia and vessel type or size, although this would require bigger sample sizes and be more costly. In addition, it should be noted, that the vessel area calculation included here could be improved by manually tracing the lumen or the entire vessel. This would aid the inherent bias of imaging ultrathin sections with scanning electron microscopy, whereby thinner or thicker portions of vessels can be captured depending on the cutting angle.

In agreement with previous observations (Bisht et al., 2016; Joost et al., 2019), I confirmed that microglia use their cell body to directly touch the BM and astrocytic endfeet. More rarely, I observed Iba1+ processes located within the BM and EC, which could be representative of either perivascular macrophages, infiltrating macrophages or microglia. As they were found in the ipsi- *LMol,* it is tempting to speculate that these processes are sealing possible BBB leakages. However, our sampling is based on cell bodies, thus, results with microglial processes were only qualitative, but represent an interesting route of subsequent data analysis. Future investigations could use FIB-SEM to build a 3DEM dataset to characterize the contacts between microglial processes and the BBB following MRIgFUS. FIB-SEM removes very small layers (3 nm) of tissue after each image and allows acquiring a z-stack with very high-resolution (3–5 nm in x, y, and z planes) that can be segmented across different neuropil and vessel structures (micael 2020).

Notably, a 3DEM dataset could be used to explore the occasional signs of blood vessel damage I observed in the *ipsi- LMol*. For example, I found microglia contacting erythrocytes, which are not normally found in the CNS but have been identified before with MRIgFUS (Hynynen et al., 2001). Erythrocytes can enter the brain after blood vessel disruption and are a physical component of the coagulation cascade that attempts to block blood from further

penetrating into the nervous tissue (Xia et al., 2022). Microglia area needed for the elimination of blood cells after vessel disruption (Xia et al., 2022), highlighting yet another factor that merits further research after MRIgFUS.

In addition to blood cells, I identified swollen astrocytic endfeet, a frequent outcome of edema and elevated BBB permeability (Ezan et al., 2012; Nahirney & Tremblay, 2021). I inquired next if the contacts microglia made with swollen astrocytic endfeet would be altered in the ipsi- *vs* contra- *LMol* at 1 h and 24 h. Although the average number of contacts did not change, their relative frequency was significantly higher in the ipsi- *vs* contra- *LMol* at 1 h and 24 h. Of note, the observation of swollen endfeet in the contra- *LMol* is not unexpected and has been reported previously (Mathiisen et al., 2010). In specific contexts, such as postnatal development in the cerebral cortex of mice, or in the *LMol* of young rats, it has been suggested that microglia fill gaps in the *glia limitans* (Mondo et al., 2020, Mathiisen et al., 2010). However, 2-photon chemical apoptotic ablation of cortical astrocytic endfeet without associated BBB permeability in young mice, led to a replacement by proximal astrocytic endfeet, while microglia remained only adjacent to the affected area to engulf damaged cells (Mills et al., 2022). It is possible that a specific crosstalk exists between microglia and astrocytes responding to BBB permeability (Vainchtein & Molofsky, 2020). Studies assessing the relationship between microglia and astrocytic endfeet in the context of MRIgFUS are thus needed (Choi et al., 2010). One strategy could be to deplete microglia using, for example, an inhibitor of the colony-stimulating factor 1 receptor, such as PLX5622 (Elmore et al., 2014), and follow with MRIgFUS. Next, astrocytes could be characterized post-mortem, employing the same methodological approach as done in this thesis for microglia. Arguably, if a crosstalk between microglia and astrocytes is required to manage the acute inflammation caused by MRIgFUS

BBB modulation, then the microglia-depleted group would exhibit stronger signs of inflammatory stress, both in the parenchyma, but also in astrocytes.

Alternatively, studies could investigate the purinergic crosstalk between microglia and astrocytic endfeet. It has been proposed that mitochondria adjacent to the cell membrane in endothelial cells participate in purinergic signaling that attracts microglia to blood vessels (Császár et al., 2022; Cserép et al., 2020). I was curious if the interactions microglia made with the BBB after MRIgFUS were influenced by these organelles. There was no significant difference in the average number of contacts between microglia and endothelial cells or astrocytic endfeet with proximal mitochondria. However, the relative frequency of those microglia-astrocytic endfeet mitochondrial interactions was significantly higher in the ipsi- *LMol* compared to contra- at 24 h. Albeit tempting to speculate that mitochondria in astrocytic endfeet play a role in the chemotaxis of microglia toward vessels, it is fundamental to note that 3DEM would be more appropriate for the analysis of this relationship. As my work examines ultrathin sections, the presence of mitochondria in the astrocytic endfeet contacted by microglia was likely underestimated. 3D imaging is warranted to examine across the entire endfeet volumes the presence of mitochondria at sites of contact with microglia. Once again, a 3DEM dataset obtained after MRIgFUS can help clarify this.

4.3. Microglia show signs of cellular stress at the nanoscale level in response to magnetic resonance imaging-guided focused ultrasound sonication with microbubbles

Meeting the energetic requirements of an inflammatory response can lead to cellular stress (Lauro & Limatola, 2020; Paolicelli et al., 2022). Indeed, stereotaxic injection of plasma in the brain was associated with oxidative stress, reactive oxygen species and oxidative

phosphorylation gene expression in microglia (Mendiola et al., 2023). I hypothesized that, in response to the evasion of blood molecules into the brain after MRIgFUS BBB modulation, there are increased ultrastructural markers of cellular stress in ipsi- *vs* contra- microglia, both at 1 h and 24 h. These markers include, but are not restricted to: mitochondrial elongation and vacuolization or elevated number of mitochondria per microglia, as a result of increased energetic demand; elevated presence or dilation of ER/Golgi apparatus caused by upregulated protein translation; and increased number of autophagosomes, a cytoplasmic double-membraned structure responsible for degrading abnormal intracellular proteins, excess or damaged organelles (Choi et al., 2022; El Hajj et al., 2019; Katoh et al., 2017; Savage et al., 2019; St-Pierre et al., 2022). Significantly, the average number of ER/Golgi and dilated ER/Golgi were not altered across all groups.

However, it was possible that specific microglial states may be more responsive to MRIgFUS than others and hence display marker of cellular stress more prevalently. Thus, I examined next the relative distribution of ER/Golgi and mitochondria using nonlinear regression fits, which indicated that some microglia shifted to possess an increased number of markers of cellular stress at 1 h (ER/Golgi cisternae and elongated mitochondria), while somewhat returning at 24 h for mitochondria, but not for the ER/Golgi. These findings pointed that, in microglia that are responsive to MRIgFUS, there is a continuous cellular stress due to protein production, as opposed to a discontinuous mitochondrial stress. Contrastingly, microglial cell bodies with dystrophic mitochondria were more frequent in the ipsi- *vs* contra- *LMol* at 24 h after MRIgFUS, with no change for dilated ER. These results are contradicting, warranting more conclusive findings, although there is support in the literature for increased mitochondrial stress following FUS+MB. Elevated [18F] DPA-714 binding to the translocator protein (TSPO), present in

microglial mitochondria and typically upregulated with inflammation, was observed at 24 h after FUS+MB in the cerebral cortex and hippocampus of female rats (Sinharay et al., 2019). Alterations in mitochondria are of special relevance to MRIgFUS, if considering the evidence that these organelles are required to microglia-blood vessels interactions (Császár et al., 2022; Cserép et al., 2020) and that genetic shifts associated with cellular stress are present in microglia following stereotaxic injection of plasma into the brain (Mendiola et al., 2023). To clarify if ER/Golgi apparatus and mitochondrial stress happen after MRIgFUS, future investigations could quantify components of the unfolded protein response, triggered along with ER/Golgi stress, and reactive oxygen species in isolated microglial cells (Dumas et al., 2021).

4.4. Microglia possibly decrease trogocytosis at the nanoscale level in response to magnetic resonance imaging-guided focused ultrasound sonication with microbubbles

The marked increase in IgG staining I observed at 24 h following MRIgFUS led me to inquire if the phagocytic activity of microglia was affected in the treated hemisphere, which would explain the parenchymal accumulation of this immune molecule (Readnower et al., 2010), even after closure of the BBB. IgG binds to microglial membrane scavenger receptors, prompting signaling cascades that drive a partial or full phagocytosis (Wilkinson & El Khoury, 2012). Correspondingly, this would increase the number of cytoplasmic electron-dense (filled) phagosomes, which partially merge with primary lysosomes full of hydrolytic enzymes to form a filled phagolysosome, also known as a secondary lysosome (De Felice et al., 2022; St-Pierre et al., 2022). In this structure, the material engulfed by the cell is broken down to compounds that can be recycled, including lipids carbohydrates and proteins (Majumdar et al., 2007). Thus, efficient phagolysosome responses require proportional increases in the number of phagosomes,

primary and secondary lysosomes. Moreover, after the phagolysosome fusion, part of the phagosome cell membrane is released in circular, electron-lucent (empty) phagosome, used to salvage phospholipids. During ensuing cellular stress, however, the digestive activity of microglia can become less efficient (Plaza-Zabala et al., 2017) and cause cells to accumulate tertiary lysosomes, which contain elements that were not fully digested (St-Pierre et al., 2022).

Increased phagocytosis of Aβ by microglia, inferred by colocalization studies, in AD pathology mouse models (Jordão et al., 2013), have led me to hypothesize that MRIgFUS can modulate the digestive activity of microglia, provided there are elements extravasating from the blood. This process would occur at steady-state conditions following MRIgFUS, which could cause dysregulated phagocytosis of neuropil elements. To assess this, I quantified the number of empty and filled phagosomes, autophagosomes and primary, secondary and tertiary lysosomes within the cell body of microglia in the contra- and ipsi- *LMol* at 1 h and at 24 h after MRIgFUS. While I did not find any significant differences in the average number and relative frequency of empty and filled phagosomes, autophagosomes and tertiary lysosomes, microglia had significantly fewer primary lysosomes per cell body and a significant decrease in the number of cell bodies with any primary or secondary lysosomes at 24 h. Notably, previous results in the lab identified a steady-state significant increase in immature lysosomes, consisting of both primary and secondary lysosomes, in the ventral *Rad vs* dorsal *Rad* hippocampus of adult male mice (De Felice et al., 2022). In this work, gene expression analyses further indicated that this increase in lysosomes was associated with a higher phagocytic intake in the ventral hippocampal pole (De Felice et al., 2022). It is surprising that despite the evasion of blood-derived molecules into the brain parenchyma, at 24 h, MRIgFUS reduces the number of microglial primary lysosomes, particularly, in an area where they are markedly present.

Albeit somewhat contrastingly to previous reports that altering the BBB induces microglial phagocytosis (Jia et al., 2022), the decrease in primary lysosomes following MRIgFUS could be an indicator of important and detrimental decreases on physiological removal of debris and synapses, crucial for synaptic plasticity (Tremblay et al., 2010). To test this hypothesis, I determined the number of interactions with post- and pre-synaptic elements, neuronal cell body, myelinated axons, degraded myelin, extracellular space and extracellular digestion per cell at 1 h and 24 h after MRIgFUS in ipsi- *vs* contra- *LMol*. I did not find significant differences in the average number of contacts between microglial cell bodies and listed neuronal elements, except for pre-synaptic elements, whereby in both ipsi- and contra-hemispheres, reduced interactions were observed at 24 h.

To understand this effect in both hemispheres, I referred to the nonlinear regression fits, which were significantly different between contra- and ipsi- conditions at 1 h and 24 h after MRIgFUS. Overall, the fits suggested ipsi- microglia cell bodies tended to decrease their contacts with pre-synaptic elements at 1 h and 24 h after MRIgFUS which contributed to a less heterogenous distribution at 1 h, but to an opposite effect at the 24 h timepoint. I hypothesize that, in addition to an overall reduction in microglial pre-synaptic contacts at 24 h *vs* 1 h timepoints, this effect is stronger for particular states within the ipsi- hemisphere. This hypothesis could be tested by characterizing the morphology of Iba+ cells in contact with synapsin+ pre-synaptic elements via confocal microscopy for instance.

Functionally, decreased microglia-pre-synaptic interactions could impair trogocytosis, a mechanism by which microglia partially engulf pre-synapses and stimulate spine filopodia formation to modulate synaptic plasticity (Weinhard et al., 2018). Stimulation of filopodia, on the other hand, is a process that requires microglia to engulf the extracellular matrix (Nguyen et

al., 2020), a structural component of the brain embedded in the extracellular space. Notably, I identified a significant decrease in frequency of microglial contacts with extracellular space pockets in the ipsi- *vs* contra- *LMol* at 24 h after MRIgFUS. Putting the pieces together, it is possible that in the ipsi- *LMol* following MRIgFUS, microglia interact less with pre-synaptic elements and the extracellular space, reducing trogocytosis and, as result, the need for lysosomes required for digestion. Confocal imaging of pre-synaptic (synapsin), microglial (Iba1), extracellular matrix (Aggregan) and phagolysosomal (CD68) markers could help explore this relationship. Moreover, studies exploring neuronal function and behavioral would be necessary to understand the outcomes of reduced trogocytosis (Morini et al., 2021).

4.5. Limitations

The effects of MRIgFUS on microglia were tested on wild-type adult male mice, however, for future clinical application, additional testing of similar questions in human-derived models would be important (Masuda et al., 2020). Since access to human cohorts is another challenge in itself, stem-cell derived human microglia transplanted into mice could be a more accessible and easier alternative (Fattorelli et al., 2021). Another important limitation of my experimental design is a male only cohort. Increasingly, research shows microglia can have specific phenotypic responses in female *vs* males (Bordeleau et al., 2019). This is significant also considering how the conditions that aim to be treated by MRIgFUS also present distinct prevalence per sex, with AD, for example, being more frequent in females (Chen et al., 2021). The use of males only *vs* both sexes was not a choice made lightly. We opted to start with males due to technical limitations and to allow more comparisons with the current literature, but future studies investigating female cohorts and possible microglial sex differences are highly encouraged.

In addition, in the present study, MRIgFUS was targeted to the left hemisphere, while the nontargeted, right hemisphere, was used as the control. Similar designs are very common in the MRIgFUS field (Blackmore et al., 2023), however, microglia can exhibit lateralized responses, that is, they can vary between the right and left hemispheres (Ohm et al., 2019; Petrasch-Parwez et al., 2020). For example, there is higher Iba1+ cell density in the right, compared to the left cingulate cortex of individuals with schizophrenia and bipolar disorder (Petrasch-Parwez et al., 2020). It is unclear whether lateralization represents a generalized microglial trait, or is a phenotype restricted to certain CNS disorders. Nonetheless, communication between microglia in the two hemispheres could help explain some curious findings, such as the observed main effect in microglia NND in the *CA1* or in soma roundness and microglial-pre-synaptic contacts in the *LMol.* In this regard, from 1 h to 24 h, microglia could secrete factors in the treated ipsilateral hemisphere, which impact the contralateral side. Another speculation on this topic would be that the hemisphere main effect on the number of homeostatic and dystrophic mitochondria following MRIgFUS is a combinatory effect of BBB modulation and left hemisphere lateralization of microglia. Overall, however, to exclude a possible lateralization confounder, it would be necessary to include an additional cohort of animals that were not targeted by MRIgFUS to be used as a lateralization control.

4.6. Conclusion

MRIgFUS causes mechanical stress in the BBB and increases the evasion of molecules from the blood into the brain parenchyma. This process triggers a local, acute inflammatory process in the targeted area that resolves within weeks. As the resident immune cells of the brain, microglia are likely required to oversee the inflammation induced by MRIgFUS. However, it is not currently known how these cells engage with the area targeted by MRIgFUS, particularly at 1 h after the treatment, when there is a peak in BBB permeability, and at the 24 h mark, when the permeability levels of the BBB are restored. Understanding the baseline responses of microglia to MRIgFUS is fundamental to ensure that their homeostatic roles are not disrupted by this technology. My thesis provides the first spatiotemporal cellular and subcellular description of the hippocampal microglia of adult male mice at 1 h and 24 h following MRIgFUS. My results show that following MRIgFUS, IgG can be found in the *CA1* parenchyma which did not lead to significant differences in Iba1+ cell density and distribution at 1 h and 24 h in the ipsi- *vs* contra-hemispheres. MRIgFUS was associated with increased Iba1+ soma perimeter at 24 h in the ipsi- *vs* contra- *LMol,* accompanied by a shift in the relative distribution of shape descriptors compatible with a rod microglial morphology at both 1 h and 24 h. In the ipsi- *vs* contra- *LMol,* microglial interactions with the BBB correlated with vessel area and were more frequent with swollen astrocytic endfeet. By contrast, microglial cell bodies interacted less frequently with pre-synaptic contacts and extracellular space pockets, which may have impacted trogocytosis rates. Collectively, my thesis proposes that MRIgFUS leads to subtle responses in *CA1* microglia in adult male mice at 1 h and at 24 h following treatment, which suggests a preservation of their homeostatic roles in the brain, pushing forward utilization of MRIgFUS. However, further investigations *in vivo* dissecting at molecular levels the interactions between microglia and

neuronal elements, in addition to the BBB, are encouraged to translate MRIgFUS into human treatments.

APPENDIX TABLES

Table 1. Increased BBB permeability descriptive statistics.

p values are given after paired t-test of contra- and ipsi- average contrast intensity (Average contrast intensity) and 2-way ANOVA with Šídák's multiple comparisons test of optical density absolute values in each CA1 strata (Optical density). For each data, SW results, mean and S.E.M of n = 3 animals/timepoint are given. ANOVA: analysis of variance, BBB: blood-brain barrier, *CA1*: *cornu ammonis* 1, *LMol*: *stratum lacunosum moleculare*, *Or*: *stratum oriens*, *Py*: *stratum pyramidal* and *Rad*: *stratum radiatum* Contra-: contra-, Ipsi-: ipsi-, SW: Shapiro-Wilk normality test, N: no, Y: yes, *p: p* value, f: f value, t: t distribution, df: degrees of freedom, h: hours and S.E.M. standard error of the mean.

	Paired t test		Contra-			Ipsi-		
Average contrast intensity	df=5	*p*	SW	Mean	S.E.M	SW	Mean	S.E.M
	t=2.66	0.044	Y	6629.0	981.4	Y	9421	1302

Optical density 2-way ANOVA

df = 30	*p*	f
Layer Time	0.94	0.43
Layer	0.77	0.45
Time	<0.0001	17.49
Subject	0.39	1.10

	Optical Densiy - Šídák's multiple comparisons									
	LMol		*Rad*		*Py*		*Or*		CA1	
	p	t	*p*	t	*p*	t	*p*	t	*p*	t
C1xI1	1.00	0.44	0.99	0.61	>0.99	0.16	>0.99	0.0700	1.00	0.31
C1xC24	>0.99	0.0200	>0.99	0.05	>0.99	0.07	>0.99	0.02	>0.99	0.11
C1xI24	0.0013	4.20	0.15	2.33	0.44	1.73	0.08	2.64	0.0400	2.87
I1xC24	1.00	0.41	0.99	0.57	>0.99	0.08	>0.99	0.0500	>0.99	0.20
I1xI24	0.0044	3.76	0.46	1.72	0.55	1.58	0.09	2.57	0.09	2.56
C24xI24	0.0014	4.17	0.17	2.28	0.49	1.66	0.08	2.62	0.06	2.76

Table 2. Microglial density and distribution descriptive statistics.

p values are given after mixed effects 2-way ANOVA with Šídák's multiple comparisons test comparing averages per animal for each *CA1* strata across the two timepoints (1 and 24 h). For each data, SW results, mean and S.E.M of n = 3 animals/timepoint/hemisphere are given. ANOVA: analysis of variance, BBB: blood-brain barrier, *CA1*: *cornus ammonis* 1, *LMol*: *stratum lacunosum moleculare*, *Or*: *stratum oriens*, *Py*: *stratum pyramidal* and *Rad*: *stratum radiatum* C or Contra-: contra-, I or Ipsi-: ipsi-, SW: Shapiro-Wilk normality test, N: no, Y: yes, p: p value, f: f value, t: t distribution, df: degrees of freedom, T: timepoint, H: hemisphere, h: hours, S.E.M. standard error of the mean and NND: nearest neighbour distance.

	Contra-			Ipsi-		
	SW	Mean	S.E.M	SW	Mean	S.E.M
		Density (μm^2)				
LMol		0.00010	0.00000		0.00010	0.00000
Rad		0.00010	0.00000		0.00020	0.00000
Py	Y	0.00010	0.00000	Y	0.00020	0.00000
Or		0.00010	0.00000		0.00010	0.00000
CA1		0.00020	0.00000		0.00020	0.00000
		Cluster density (μm^2)				
LMol	N	0.00	0.00	N	0.00	0.00
CA1		0.00	0.00	Y	0.00	0.00
		NND (a.u.)				

		53.20	2.20			53.50	2.57		
LMol									
		53.30	1.41			50.40	2.45		
Rad									
		73.70	2.54			69.00	0.68		
Py	Y				Y				
		56.50	2.67			54.90	4.21		
Or									
		68.00	4.38			61.90	8.59		
CA1									
Spacing index (a.u.)									
		0.35	0.01			0.37	0.01		
LMol									
		0.41	0.03			0.39	0.01		
Rad									
		0.53	0.03			0.49	0.08		
Py	Y				Y				
		0.40	0.02			0.45	0.04		
Or									
		0.76	0.06			0.64	0.12		
CA1									

Mixed effects 2-way ANOVA				Šídák's multiple comparisons test					
				1 h *vs* 24 h			Contra- *vs* Ipsi-		
	p	f	H	p	t	df	T	p	t	df
Density (μm^2)									

T	0.13	3.6	C	0.58	0.99		1	0.28	1.78	
H	0.22	2.1	I	0.12	2.17		24	0.96	0.27	4
TxH	0.35	1.1								
T	0.28	1.3	C	1.00	0.07		1	0.24	1.70	
H	0.28	1.3	I	0.24	1.70		24	1.00	0.07	
TxH	0.25	1.6								
T	0.35	1.0	C	0.81	0.59		1	0.90	0.42	
H	0.67	0.2	I	0.69	0.80	8	24	0.97	0.21	
TxH	0.89	0.0								
T	0.22	2.1	C	0.91	0.40		1	0.69	0.85	8
H	0.78	0.1	I	0.25	1.67		24	0.90	0.43	
TxH	0.42	0.8								
T	0.16	2.4	C	0.54	1.05		1	0.92	0.37	
H	0.66	0.2	I	0.49	1.14		24	0.96	0.28	
TxH	0.95	0.0								
Cluster density (μm^2)										
T	0.50	0.5	C	0.75	0.71		1	0.08	2.42	
H	0.13	2.9	I	0.24	1.71		24	>0.9999	0.00	
TxH	0.13	2.9				8				8
T	0.82	0.1	C	0.66	0.85		1	0.24	1.70	
H	0.19	2.1	I	0.86	0.51		24	0.93	0.34	
TxH	0.36	0.9								
NND (a.u.)										
T	0.71	0.2	C	0.61	0.94		1	*0.07*	3.18	
H	0.13	3.6	I	0.26	1.64		24	0.88	0.49	
TxH	*0.06*	6.8								4
T	0.18	2.7	C	0.49	1.15		1	0.55	1.11	
H	0.47	0.6	I	0.20	1.81		24	1.00	0.02	
TxH	0.49	0.6								
T	0.12	3.0	C	0.68	0.83	8	1	0.59	0.97	
H	0.44	0.7	I	0.27	1.62		24	0.98	0.18	
TxH	0.59	0.3								
T	0.81	0.1	C	0.95	0.28		1	0.99	0.15	8
H	0.72	0.1	I	1.00	0.08		24	0.93	0.36	
TxH	0.89	0.0								
T	**0.05**	5.5	C	0.30	1.53		1	1.00	0.03	

H	0.89	0.0	I	0.21	1.79		24	0.97	0.23	
TxH	0.86	0.0								
Spacing index (a.u.)										
T	0.31	1.3	C	0.34	1.44		1	0.59	1.04	
H	0.58	0.4	I	0.95	0.29		24	0.98	0.19	
TxH	0.43	0.8								4
T	0.18	2.6	C	0.04	1.01		1	0.22	2.00	
H	0.10	4.7	I	0.08	1.71		24	0.57	1.08	
TxH	0.55	0.4								
T	0.61	2.6	C	0.92	0.37		1	0.54	1.06	
H	0.67	4.7	I	0.50	1.13	8	24	0.89	0.44	
TxH	0.32	0.4								
T	0.39	0.8	C	0.90	0.42		1	0.97	0.24	
H	0.53	0.4	I	0.66	0.86		24	0.76	0.68	8
TxH	0.76	0.1								
T	0.07	4.2	C	0.63	0.90		1	0.63	0.90	
H	0.19	2.1	I	0.49	1.15		24	0.49	1.15	
TxH	0.87	0.0								

Table 3. Microglial morphology descriptive statistics.

p values are given after a mixed-effects 2-way ANOVA with Šídák's multiple comparisons test comparing averages per animal across the ipsi- and contra- *LMol* across the two timepoints (1 and 24 h). For each data, SW results, mean and S.E.M of n = 3 animals/timepoint are given. ANOVA: analysis of variance, a.u.: arbitrary unit, #: number, *LMol*: *stratum lacunosum moleculare*, C or Contra-: contra-, I or Ipsi-: ipsi-, SW: Shapiro-Wilk normality test, *: N too small for normality assessment, p: p value, f: f value, t: t distribution, df: degrees of freedom, T: timepoint, H: hemisphere, h: hours and S.E.M. standard error of the mean.

	Contra-		Ipsi-		Mixed effects 2-way ANOVA		
	Mean	S.E.M	Mean	S.E.M		f	p
Soma							
Area (μm^2)	43.31	3.79	63.72	20.89	T	3.53	0.13
					H	3.35	0.14
					TxH	2.35	0.20
Aspect Ratio (a.u.)	1.88	0.11	1.93	0.08	T	4.76	0.06
					H	0.30	0.60
					TxH	0.11	0.75

Perimeter (a.u.)	29.46	0.13	39.58	7.15	T	1.82	0.25
					H	15.43	0.02
					TxH	8.01	0.05
Roundness (a.u.)	0.58	0.03	0.58	0.02	T	11.17	0.01
					H	0.11	0.75
					TxH	0.48	0.51
Circularity (a.u.)	0.57	0.02	0.54	0.05	T	3.06	0.16
					H	4.63	0.10
					TxH	4.63	0.10
Solidity (a.u.)	0.82	0.00	0.80	0.01	T	0.39	0.56
					H	1.68	0.26
					TxH	0.57	0.49
Convex							
Area (μm^2)	1084.00	24.79	1138.00	151.90	T	1.86	0.21
					H	0.18	0.69
					TxH	0.96	0.36
Aspect Ratio (a.u.)	1.69	0.01	1.67	0.01	T	0.00	0.99
					H	0.07	0.81
					TxH	0.07	0.81
Perimeter (a.u.)	144.20	1.13	145.80	6.65	T	0.34	0.58
					H	0.03	0.87
					TxH	0.67	0.44
Roundness (a.u.)	0.67	0.01	0.65	0.02	T	1.08	0.36
					H	1.48	0.29
					TxH	4.11	0.11
Circularity (a.u.)	0.64	0.01	0.64	0.00	T	0.07	0.79
					H	0.02	0.88
					TxH	0.01	0.91
Solidity (a.u.)	0.89	0.01	0.90	0.01	T	4.48	0.07
					H	1.62	0.24
					TxH	0.02	0.88
Automated cell mask							
Area (μm^2)	261.60	6.73	288.50	46.17	T	3.76	0.12
					H	1.17	0.34
					TxH	2.52	0.19
Aspect Ratio (a.u.)	1.84	0.04	1.90	0.03	T	0.01	0.91
					H	0.14	0.72
					TxH	0.22	0.65
Roundness (a.u.)	0.60	0.00	0.59	0.00	T	0.00	0.99
					H	0.22	0.65
					TxH	0.01	0.92
Fractal dimension (a.u.)	1.39	0.01	1.38	0.01	T	0.00	0.99
					H	0.05	0.83
					TxH	0.56	0.48

Lacunarity (a.u.)	0.25	0.00	0.27	0.01	T	0.76	0.41
					H	1.56	0.25
					TxH	0.17	0.69
Circularity (a.u.)	0.03	0.01	0.03	0.00	T	0.63	0.45
					H	0.01	0.91
					TxH	0.47	0.51
Perimeter (μm)	388.60	3.95	386.20	29.25	T	0.31	0.59
					H	0.00	0.96
					TxH	0.53	0.49
Solidity (a.u.)	0.25	0.00	0.27	0.01	T	0.76	0.41
					H	1.56	0.25
					TxH	0.17	0.69
Arborization							
Branches (#)	61.81	0.84	63.78	5.29	T	0.30	0.61
					H	0.08	0.79
					TxH	0.78	0.43
Junctions (#)	30.33	0.34	31.49	2.60	T	0.30	0.61
					H	0.11	0.76
					TxH	0.68	0.46
Longest Shortest Path (μm)	69.91	1.09	71.80	3.72	T	0.39	0.55
					H	0.20	0.67
					TxH	1.30	0.29
Max branch length (μm)	14.43	0.10	15.32	0.19	T	0.20	0.66
					H	1.88	0.21
					TxH	0.02	0.90

Šídák's multiple comparisons test

	1 h *vs* 24 h				Contra- *vs* Ipsi-		
H	p	t	df	T	p	t	df
Soma							
C	0.89	0.44	8	1	0.98	0.21	4
I	0.08	2.42		24	0.15	2.38	
C	0.22	1.77		1	0.22	1.77	8
I	0.40	1.31		24	0.40	1.31	
C	1.00	0.05		1	0.73	0.78	4
I	0.08	2.47		24	0.02	4.78	
C	0.04	2.85		1	0.74	0.73	8
I	0.19	1.87		24	0.96	0.25	
C	0.67	0.84		1	>0.9999	0.00	4
I	0.08	2.42		24	0.08	3.04	
C	0.39	0.19		1	0.92	0.38	
I	1.68	0.91		24	0.39	1.45	8
Convex							
C	0.96	0.27	8	1	0.91	0.40	8

I	0.25	1.66	24	0.58	0.99	
C	0.99	0.13	1	>0.9999	0.00	4
I	0.99	0.15	24	0.93	0.37	
C	0.98	0.17	1	0.88	0.46	8
I	0.58	0.99	24	0.75	0.70	
C	0.85	0.53	1	0.16	2.30	4
I	0.13	2.11	24	0.84	0.57	
C	0.96	0.27	1	1.00	0.03	8
I	0.99	0.11	24	0.98	0.19	
C	0.27	1.60	1	0.57	1.01	
I	0.36	1.39	24	0.70	0.79	8
			Automated mask			
C	0.92	0.36	1	0.93	0.36	4
I	0.07	2.50	24	0.25	1.89	
C	0.90	0.41	1	0.81	0.60	
I	0.96	0.26	24	1.00	0.07	
C	1.00	0.08	1	0.91	0.40	
I	1.00	0.06	24	0.96	0.26	
C	0.84	0.54	1	0.76	0.68	
I	0.85	0.52	24	0.92	0.37	
C	0.94	0.32	8 1	0.82	0.59	
I	0.63	0.91	24	0.47	1.18	8
C	0.55	1.05	1	0.83	0.57	
I	1.00	0.07	24	0.91	0.40	
C	0.99	0.12	1	0.84	0.55	
I	0.63	0.91	24	0.87	0.48	
C	0.94	0.32	1	0.82	0.59	
I	0.63	0.91	24	0.47	1.18	
			Arborization			
C	0.99	0.16	1	0.91	0.42	
I	0.58	0.99	24	0.70	0.83	4
C	0.99	0.12	1	0.93	0.35	
I	0.60	0.95	24	0.71	0.81	
C	0.92	0.36	8 1	0.87	0.49	
I	0.43	1.25	24	0.50	1.12	
C	0.97	0.23	1	0.65	0.88	8
I	0.90	0.41	24	0.54	1.06	

Table 4. Nonlinear regression parameters.

p values are given after paired Wilcoxon test of Contra- *vs* Ipsi- nonlinear regression curve fits. These were modeled after the relative distribution of each parameter in the two *LMol* (contra- and ipsi-) nested into the two timepoints (1 and 24 h). For each data, Amplitude, Mean and p value of n = 3 animals/timepoint/hemisphere are given. a.u.: arbitrary unit, #: number, p: p value, *LMol*: *stratum lacunosum moleculare*, Contra-: contra-, Ipsi-: ipsi- and h: hours.

Nonlinear regression		1 h		24 h	
		Contra-	Ipsi-	Contra-	Ipsi-
Soma					
Area (μm^2)	Amplitude	60.20	62.57	36.40	20.91
	Mean	37.09	38.20	34.36	59.99
	p	<0.0001		<0.0001	
Aspect Ratio (a.u.)	Amplitude	47.24	58.09	32.00	37.24
	Mean	1.55	1.55	1.86	1.72
	p	<0.0001		<0.0001	
Circularity (a.u.)	Amplitude	13.82	13.59	15.02	16.62
	Mean	0.59	0.57	0.57	0.49
	p	<0.0001		0.58	
Perimeter (µm)	Amplitude	61.38	46.52	47.87	28.05
	Mean	28.17	28.36	24.25	40.68
	p	<0.0001		<0.0001	
Roundness (a.u.)	Amplitude	13.17	14.80	12.38	11.77
	Mean	0.62	0.63	0.53	0.55
	p	<0.0001		<0.0001	
Solidity (a.u.)	Amplitude	21.81	23.14	27.40	23.78
	Mean	0.85	0.85	0.84	0.81
	p	<0.0001		<0.0001	
Convex arbor					
Area (μm^2)	Amplitude	18.97	17.54	17.89	16.03
	Mean	988.40	912.80	969.20	1083.00
	p	<0.0001		0.00	
Aspect Ratio (a.u.)	Amplitude	20.40	18.19	22.24	20.15
	Mean	1.49	1.51	1.42	1.52
	p	<0.0001		<0.0001	
Circularity (a.u.)	Amplitude	14.45	14.76	17.06	17.90
	Mean	0.63	0.64	0.70	0.67
	p	<0.0001		<0.0001	
Perimeter (µm)	Amplitude	18.97	20.54	21.53	21.59
	Mean	140.10	137.00	138.30	145.30
	p	0.00		0.36	
Roundness	Area	5.28	5.12	5.39	5.25

(a.u.)	Mean	0.18		0.18	0.20		0.17
	p		<0.0001			<0.0001	
Solidity	Amplitude	11.46		9.73	10.92		13.77
(a.u.)	Mean	0.89		0.98	0.95		0.93
	p		0.73			0.20	
				Automatic arbor			
Aspect Ratio	Amplitude	711.70		18.35	16.86		22.36
(a.u.)	Mean	1.65		1.47	1.49		1.61
	p		<0.0001			<0.0001	
Circularity	Amplitude						
(a.u.)	Mean						
	p						
Perimeter	Amplitude	15.09		13.70	10.51		15.08
(μm)	Mean	367.00		359.20	349.10		334.70
	p		<0.0001			<0.0001	
Roundness	Amplitude	11.55		9.31	9.34		10.71
(a.u.)	Mean	0.63		0.60	0.62		0.58
	p		0.00			0.00	
Solidity	Amplitude	20.36		17.41	22.63		16.83
(a.u.)	Mean	0.25		0.25	0.25		0.27
	p		<0.0001			<0.0001	
Area	Amplitude	24.02		26.54	14.62		15.69
(μm^2)	Mean	241.80		187.30	223.00		231.80
	p		<0.0001			0.00	
Fractal Dimension	Amplitude	17.00		13.00	10.70		11.36
(a.u.)	Mean	1.40		1.38	1.38		1.39
	p		0.02			0.00	
Lacunarity	Amplitude	26.83		19.28	22.77		17.35
(a.u.)	Mean	0.32		0.32	0.32		0.32
	p		<0.0001			<0.0001	
				Arborization			
Branches	Amplitude	35.04		28.32	25.84		24.95
(#)	Mean	56.75		57.23	59.33		53.89
	p		<0.0001			<0.0001	
Junctions	Amplitude	34.47		27.79	25.04		25.12
(#)	Mean	28.04		27.86	29.37		26.37
	p		<0.0001			<0.0001	
Longest Shortest Path	Amplitude	20.87		24.23	20.65		21.86
(μm)	Mean	70.54		69.25	64.74		71.46
	p		<0.0001			0.05	

Max Branch Length (μm)	Amplitude	26.37	26.04	20.26	33.79
	Mean	13.65	13.54	13.07	12.60
	p	<0.0001		<0.0001	

Table 5. Microglia density and distribution correlation with BBB permeability descriptive statistics.

p values are given after Spearman r correlation between contrast enhancement and density, NND, spacing index, cluster density and optical density in the ipsi- *LMol*. For each data, SW results, mean, S.E.M, r and p of n = 3 animals/timepoint/hemisphere are given. NND: nearest neighbour distance, SW: Shapiro-Wilk normality test, N: no, Y: yes, p: p value, r: r coefficient and S.E.M. standard error of the mean.

				Density		NND		Spacing Index		Cluster density	
	SW	Mean	S.E.M	r	p	r	p	r	p	r	p
Density	Y	0.00	0.00	1.00		-0.94	0.02	0.20	0.71	0.38	0.47
NND		53.46	1.41	-0.94	0.02	1.00		-0.14	0.80	-0.49	0.33
Spacing Index		0.37	0.01	0.20	0.71	-0.14	0.80	1.00		-0.70	0.14
Cluster density		0.00	0.00	0.38	0.47	-0.49	0.33	-0.70	0.14	1.00	
Optical density		1.17	0.07	-0.94	0.02	0.89	0.03	-0.09	0.92	-0.52	0.30

Table 6. Morphology correlation with BBB permeability.

p values are given after Spearman r correlation between optical density and morphology parameters in the ipsi- *LMol*. For each data, r and p of n = 3 animals/timepoint are given. p: p value, r: r coefficient.

	Optical density	
	p	r
Soma Area	0.24	0.60
Soma Perimeter	0.14	0.71
Soma Circularity	0.14	-0.71
Soma Aspect Ratio	0.42	0.43

Soma Roundness	0.30	-0.54
Soma Solidity	0.30	-0.54
Convex Area	0.06	0.83
Convex Perimeter	0.10	0.77
Convex Circularity	0.92	0.09
Convex Aspect Ratio	0.92	0.09
Convex Roundness	0.92	-0.09
Convex Solidity	0.80	-0.14
Automatic Arbor Area	0.18	0.66
Automatic Arbor Perimeter	0.50	0.37
Automatic Arbor Circularity	0.50	-0.37
Automatic Arbor Aspect Ratio	1.00	-0.03
Automatic Arbor Roundness	0.92	-0.09
Automatic Arbor Solidity	1.00	-0.03
Arborization Branches	0.42	0.43
Arborization Junctions	0.42	0.43
Maximum Branch length	0.42	0.43
Arborization Longest Shortest Path	0.10	0.77

Table 7. Microglia morphology principal component analysis.

For each PC, eigenvalue, proportion of variance, cumulative proportion of variance and loadings for each morphology parameter of n = 21 cells, N = 3 animals/timepoint are given. PC: principal components.

PC summary	PC1	PC2	PC3	PC4	PC5	PC6
Eigenvalue	11.77	4.172	3.04	1.951	1.887	1.556
Proportion of variance	39.23%	13.91%	10.13%	6.50%	6.29%	5.19%
Cumulative proportion of variance	39.23%	53.13%	63.27%	69.77%	76.06%	81.24%
Loadings						
Soma Area	-0.29	0.44	-0.49	0.18	-0.02	0.09
Soma Perimeter	-0.25	0.60	-0.65	0.04	-0.17	0.05

Soma Circularity	0.22	-0.56	0.60	0.26	0.01	-0.08
Soma Aspect Ratio	-0.09	0.47	-0.34	-0.26	0.62	-0.03
Soma Round	0.06	-0.41	0.32	0.27	-0.63	0.02
Soma Solidity	0.15	-0.47	0.59	0.22	0.24	-0.03
Convex Area	-0.92	0.10	0.02	0.02	-0.13	-0.22
Convex Perimeter	-0.88	0.23	0.21	-0.15	-0.15	0.04
Convex Circularity	0.10	-0.44	-0.48	0.34	0.18	-0.58
Convex Aspect Ratio	0.35	0.76	0.44	0.23	0.02	-0.08
Convex Round	-0.36	-0.73	-0.44	-0.27	-0.07	0.13
Convex Solidity	0.24	-0.19	-0.42	0.46	0.08	-0.66
Automatic Arbor Area	-0.90	0.13	-0.07	0.24	-0.12	0.11
Automatic Arbor Perimeter	-0.97	0.02	0.11	-0.01	-0.06	-0.10
Automatic Arbor Circularity	0.38	0.03	-0.20	0.46	-0.20	0.47
Automatic Arbor Aspect Ratio	0.42	0.75	0.36	0.24	0.04	-0.14
Automatic Arbor Round	-0.44	-0.71	-0.35	-0.27	-0.11	0.19
Automatic Arbor Solidity	0.29	0.00	-0.33	0.69	-0.05	0.46
Arborization Branches	-0.97	0.02	0.06	0.13	0.08	0.00
Arborization Junctions	-0.96	0.02	0.06	0.13	0.08	0.00
Maximum Branch length	-0.18	0.14	-0.02	-0.21	-0.59	-0.31
Arborization Longest Shortest Path	-0.84	0.22	0.19	0.01	-0.14	-0.13
Automatic Arbor Fractal Dimension	-0.76	-0.22	0.07	0.20	0.13	0.09
Automatic Arbor Lacunarity	-0.01	0.17	0.27	-0.30	0.00	0.13

Table 8. Microglial ultrastructure descriptive statistics.

p values are given after a mixed-effects 2-way ANOVA with Šídák's multiple comparisons test comparing averages per animal across the ipsi- and contra- Lmol across the two timepoints (1 and 24 h). For each data, SW results, mean and S.E.M of n = 3 animals/timepoint are given. ANOVA: analysis of variance#: number, Lmol: *stratum lacunosum moleculare*, C or Contra-:

contra-, I or Ipsi-: ipsi-, SW: Shapiro-Wilk normality test, *: N too small for normality assessment, p: p value, f: f value, t: t distribution, df: degrees of freedom, T: timepoint, H: hemisphere, h: hours and S.E.M. standard error of the mean.

		Contra-		Ipsi-		Mixed effects 2-way ANOVA		
Parameter	unit	Mean	S.E.M	Mean	S.E.M		f	p
BBB contacts								
Astrocytic endfeet containing mitochondria		0.17	0.12	0.24	0.04	T	0.65	0.45
						H	0.55	0.48
						TxH	2.48	0.15
Astrocytic endfeet		0.24	0.13	0.51	0.08	T	1.36	0.31
						H	2.67	0.18
						TxH	0.11	0.76
Swollen astrocytic endfeet	#/ cell	0.04	0.04	1.15	0.10	T	0.03	0.87
						H	16.48	0.02
						TxH	0.26	0.64
Endothelial cell containing mitochondria		0.05	0.05	0.08	0.03	T	0.53	0.51
						H	1.00	0.37
						TxH	1.00	0.37
Basement membrane		0.09	0.04	0.09	0.04	T	0.00	0.98
						H	0.00	0.96
						TxH	12.31	0.02
Microglial blood vessel distance	µm	6.82	1.20	7.34	0.13	T	0.36	0.56
						H	0.09	0.77
						TxH	0.56	0.47
Density of microglia associated with vessels	$\#/\mu m^2$	0.17	0.07	0.24	0.02		0.97	0.38
							1.09	0.36
							0.62	0.47
Red blood cells contacts	#/cell	0.00	0.00	0.05	0.05		1.00	0.37
							1.00	0.37
							1.00	0.37
Synaptic plasticity contact								
Synapse containing mitochondria contact		0.78	0.44	0.79	0.35	T	9.68	0.04
						H	0.01	0.94
						TxH	0.24	0.65
Post-synaptic element	#/cell	0.84	0.17	0.97	0.30	T	3.41	0.14
						H	0.35	0.59
						TxH	0.35	0.59
Pre-synaptic element		2.82	1.11	2.74	1.02	T	33.06	0.00
						H	0.05	0.82
						TxH	0.05	0.82
Satellite		0.09	0.01	0.11	0.01	T	0.01	0.91

						H	0.09	0.77
						TxH	0.09	0.77
Myelinated axon		0.13	0.03	0.20	0.06	T	1.16	0.31
						H	0.74	0.41
						TxH	0.19	0.68
Degenerating myelin		0.07	0.01	0.08	0.03	T	0.56	0.47
						H	0.06	0.82
						TxH	0.08	0.79
Extracellular digestion		0.17	0.02	0.27	0.07	T	0.75	0.41
						H	2.87	0.13
						TxH	1.90	0.21
Extracellular space		0.27	0.09	0.03	0.03	T	0.95	0.36
						H	4.35	0.07
						TxH	0.29	0.61
Proximity to dark cells		0.16	0.00	0.05	0.00	T	0.00	0.97
						H	1.75	0.22
						TxH	0.00	0.97
Intracellular organelles								
ER/Golgi		7.79	1.63	7.85	0.13	T	1.75	0.26
						H	0.00	0.95
						TxH	3.66	0.13
Dilated ER		0.87	0.00	0.89	0.37	T	2.24	0.17
						H	0.00	0.95
						TxH	2.24	0.17
Mitochondria/ER		0.97	0.38	1.03	0.02	T	1.59	0.28
						H	0.10	0.77
						TxH	4.38	0.10
Mitochondria		3.41	0.00	2.78	0.00	T	0.00	>0.9999
						H	17.32	0.01
						TxH	0.00	>0.9999
Elongated mitochondria	#/cell	0.33	0.04	0.46	0.17	T	3.18	0.15
						H	1.94	0.24
						TxH	1.94	0.24
Dystrophic mitochondria		0.08	0.00	0.32	0.09	T	0.75	0.41
						H	5.59	0.05
						TxH	0.78	0.40
Primary lysosome		0.37	0.11	0.22	0.17	T	0.12	0.74
						H	3.45	0.14
						TxH	12.72	0.02
Secondary lysosome		0.22	0.06	0.18	0.08	T	0.05	0.83
						H	0.64	0.47
						TxH	8.64	0.04
Tertiary lysosome		0.31	0.11	0.41	0.05	T	4.35	0.07

					H	1.55	0.25
					TxH	0.60	0.46
Empty phagosome		0.34	0.07	0.53	0.01	T	0.80	0.40
						H	4.26	0.07
						TxH	0.46	0.52
		0.06	0.01	0.10	0.06	T	0.64	0.47
Filled phagosome						H	0.36	0.58
						TxH	1.88	0.24
		0.04	0.01	0.04	0.04	T	0.36	0.56
Autophagosome						H	0.00	>0.9999
						TxH	1.46	0.26

	Šídák's multiple comparisons test							
		1 h *vs* 24 h				Contra- *vs* Ipsi-		
Parameter	H	p	t	df	T	p	t	df
BBB contacts								
Astrocytic endfeet containing mitochondria	C	0.25	1.68	8	1.00	0.82	0.59	8
	I	0.84	0.55		24.00	0.26	1.64	
Astrocytic endfeet	C	0.53	1.07		1.00	0.65	0.92	
	I	0.80	0.62		24.00	0.42	1.39	
Swollen astrocytic endfeet	C	0.98	0.20		1.00	0.13	2.51	
	I	0.88	0.46		24.00	0.06	3.23	
Endothelial cell containing mitochondria	C	0.61	0.94		1.00	>0.9999	0.00	4
	I	0.88	0.47		24.00	0.41	1.41	
Basement membrane	C	0.36	1.39		1.00	0.13	2.52	
	I	0.38	1.35		24.00	0.14	2.45	
Microglial blood vessel distance	C	0.60	0.96		1.00	0.73	0.74	8
	I	0.99	0.10		24.00	0.94	0.32	

Density of microglia associated with vessels	C	0.43	1.26		1.00	0.98	0.18	4
	I	0.92	0.37		24.00	0.46	1.30	
Red blood cells contacts	C	>0.9999	0.00		1.00	>0.9999	0.00	
	I	0.35	1.41		24.00	0.41	1.41	
Synaptic plasticity contacts								
Synapse containing mitochondria contact	C	0.04	2.83		1.00	0.96	0.29	4
	I	0.10	2.27		24.00	0.91	0.40	
Post-synaptic element	C	0.57	1.00		1.00	0.70	0.83	
	I	0.21	1.78		24.00	>0.9999	0.00	
Pre-synaptic element	C	0.01	4.23		1.00	0.94	0.33	
	I	0.01	3.90		24.00	>0.9999	0.00	
Satellite	C	0.95	0.29		1.00	0.90	0.42	
	I	0.99	0.13		24.00	>0.9999	0.00	
Myelinated axon	C	0.88	0.46	8	1.00	0.95	0.30	
	I	0.54	1.06		24.00	0.63	0.91	
Degenerating myelin	C	0.94	0.33		1.00	1.00	0.03	8
	I	0.74	0.73		24.00	0.92	0.36	
Extracellular digestion	C	0.93	0.36		1.00	0.97	0.22	
	I	0.28	1.59		24.00	0.12	2.17	
Extracellular space	C	0.53	1.07		1.00	0.52	1.10	
	I	0.94	0.31		24.00	0.19	1.86	
	C	1.00	0.06		1.00	0.59	0.96	

Proximity to dark cells	I	>0.9999	0.00		24.00	0.63	0.91	
Intracellular organelles								
ER/Golgi	C	0.45	1.31	4	1.00	0.45	1.31	4
	I	0.41	1.40		24.00	0.41	1.40	
Dilated ER	C	>0.9999	0.00		1.00	0.57	1.01	8
	I	0.13	2.12		24.00	0.51	1.11	
Mitochondria/ER	C	0.11	2.21		1.00	0.48	1.26	
	I	0.99	0.11		24.00	0.30	1.70	
Mitochondria	C	>0.9999	0.00		1.00	0.08	2.94	4
	I	>0.9999	0.00		24.00	0.08	2.94	
Elongated mitochondria	C	0.83	0.57		1.00	0.23	1.97	
	I	0.10	2.26		24.00	>0.9999	0.00	
Dystrophic mitochondria	C	1.00	0.01		1.00	0.55	1.05	8
	I	0.44	1.24		24.00	0.10	2.30	
Primary lysosome	C	0.43	1.25	8	1.00	0.50	1.21	
	I	0.18	1.88		24.00	0.04	3.83	
Secondary lysosome	C	0.49	1.15		1.00	0.37	1.51	4
	I	0.29	1.56		24.00	0.11	2.65	
Tertiary lysosome	C	0.15	2.02		1.00	0.94	0.33	
	I	0.62	0.93		24.00	0.35	1.43	
Empty phagosome	C	0.51	1.11		1.00	0.17	1.94	8
	I	0.99	0.15		24.00	0.58	0.98	
Filled phagosome	C	0.94	0.33		1.00	0.85	0.54	
	I	0.31	1.52		24.00	0.42	1.40	4
Autophagosome	C	0.90	0.43		1.00	0.66	0.85	8
	I	0.42	1.28		24.00	0.66	0.85	

Table 9. Microglia ultrastructural nonlinear regression statistics.

p values are given after paired Wilcoxon test of Contra- *vs* Ipsi- nonlinear regression curve fits. These were modeled after the relative distribution of each parameter in the two *LMol* (contra- and ipsi-) nested into the two timepoints (1 and 24 h). For each data, Amplitude, Mean and p value of n = 3 animals/timepoint/hemisphere are given. a.u.: arbitrary unit, *LMol*: *stratum lacunosum moleculare*, #: number, p: p value, Contra-: contra-, Ipsi-: ipsi- and h: hours.

			1 h		24 h	
			Contra-	Ipsi-	Contra-	Ipsi-
Synaptic plasticity contacts						
Synapse containing mitochondria contact	#/cell	Amplitude	40.84	71.21	70.98	72.36
		Mean	-0.46	-3.54	-0.14	-0.21
		p	0.18		<0.0001	
Post-synaptic element		Amplitude	47.54	39.60	62.38	110.50
		Mean	0.96	0.20	0.61	0.44
		p	<0.0001		<0.0001	
Pre-synaptic element		Amplitude	29.22	39.60	28.87	27.76
		Mean	2.78	0.20	1.18	0.88
		p	<0.0001		<0.0001	
Intracellular organelles						
ER/Golgi	#/cell	Amplitude	12.21	21.05	32.36	20.92
		Mean	7.43	4.29	3.97	4.41
		p	<0.0001		<0.0001	
Mitochondria		Amplitude	15.50	28.00	29.44	33.34
		Mean	0.11	-4.58	1.58	-0.12
		p	<0.0001		<0.0001	
Elongated mitochondria		Amplitude	89.95	56.09	65.89	106.40
		Mean	-0.89	-0.15	-0.25	-0.90

	p	<0.0001	<0.0001

Table 10. Microglial ultrastructural principal component analysis.

For each PC, eigenvalue, proportion of variance, cumulative proportion of variance and loadings for each morphology parameter of n = 21 cells, N = 3 animals/timepoint/hemisphere are given. PC: principal components

PC summary	PC1	PC2	PC3
Eigenvalue	3.252	3.026	2.363
Proportion of variance	12.51%	11.64%	9.09%
Cumulative proportion of variance	12.51%	24.14%	33.23%
Component selection	Selected	Selected	Selected
Loadings			
Astrocytic endfeet containing mitochondria contact	0.77	-0.07	0.19
Astrocytic endfeet contact	0.85	-0.15	0.14
Swollen astrocytic endfeet contact	0.62	-0.15	-0.14
Basement membrane contact	0.61	-0.07	0.10
Endothelial cell containing mitochondria contact	0.37	-0.13	0.15
Microglial blood vessel distance	-0.64	0.23	-0.10
Red blood cell contact	0.00	-0.07	-0.52
Synaptic element containing mitochondria contact	-0.38	0.09	0.61
Post-synaptic element contact	-0.28	-0.20	0.62
Pre-synaptic element contact	-0.15	-0.22	0.58
Myelinated axon contact	-0.23	-0.02	-0.20
Degenerating myelin contact	-0.03	0.00	-0.31
Satellite microglia	-0.03	-0.01	-0.39
Extracellular digestion	-0.13	-0.02	-0.35
Extracellular space contact	-0.02	-0.28	-0.17
ER/Golgi	-0.33	-0.77	0.03
Dilated ER	0.02	-0.49	-0.39
Mitochondria	-0.21	-0.69	0.06
Elongated mitochondria	-0.11	-0.63	0.27

Dystrophic mitochondria	-0.11	-0.45	-0.39
Primary lysosome	-0.15	0.04	-0.22
Secondary lysosome	-0.14	0.01	0.05
Tertiary lysosome	0.07	-0.66	0.06
Empty phagosome	0.20	-0.42	-0.06
Filled phagosome	-0.23	-0.44	-0.07
Autophagosome	-0.10	0.10	0.09

Table 11. Microglial ultrastructural correlation with blood vessel proximity and blood vessel area descriptive statistics.

p-values are given after Spearman r correlation between contrast enhancement and morphology parameters in the ipsi- *LMol*. For each data, r and p of n = 3 animals/timepoint/hemisphere are given. p: p value, r: r coefficient.

	Blood vessel distance	Vessel area
Microglia-blood vessel distance		0.5173
Blood vessel area	0.5173	
Astrocytic endfeet containing mitochondria contact	0.0000	0.0001
Astrocytic endfeet contact	0.0000	0.0000
Swollen astrocytic endfeet contact	0.0019	0.0001
Basement membrane contact	0.0000	0.0276
Endothelial cell containing mitochondria contact	0.0146	0.0270
Red blood cell contact	0.5216	0.2606
Post-synaptic element contact	0.4533	0.3246
Pre-synaptic element contact	0.9370	0.5768
Myelinated axon contact	0.5787	0.4383
Degenerating myelin contact	0.5244	0.7878

Satellite microglia	0.7274	0.1442
Extracellular digestion	0.1231	0.5097
Extracellular space contact	0.3380	0.7436
ER/Golgi	0.7819	0.8215
Dilated ER/Golgi	0.8906	0.9398
Mitochondria	0.7585	0.4814
Elongated mitochondria	0.7453	0.1432
Dystrophic mitochondria	0.8060	0.7034
Primary lysosome	0.9096	0.2686
Secondary lysosome	0.5248	0.9722
Tertiary lysosome	0.6204	0.7492
Empty phagosome	0.4088	0.6948
Filled phagosome	0.8533	0.4241
Autophagosome	0.8970	0.2487

REFERENCES

Abbott, N. J., Rönnbäck, L., & Hansson, E. (2006). Astrocyte–endothelial interactions at the blood–brain barrier. *Nature Reviews Neuroscience*, *7*(1), Article 1. https://doi.org/10.1038/nrn1824

Abrahao, A., Meng, Y., Llinas, M., Huang, Y., Hamani, C., Mainprize, T., Aubert, I., Heyn, C., Black, S. E., Hynynen, K., Lipsman, N., & Zinman, L. (2019). First-in-human trial of blood–brain barrier opening in amyotrophic lateral sclerosis using MR-guided focused ultrasound. *Nature Communications*, *10*, 4373. https://doi.org/10.1038/s41467-019-12426-9

Alonso, A., Reinz, E., Fatar, M., Hennerici, M. G., & Meairs, S. (2011). Clearance of albumin following ultrasound-induced blood–brain barrier opening is mediated by glial but not neuronal cells. *Brain Research*, *1411*, 9–16. https://doi.org/10.1016/j.brainres.2011.07.006

Armulik, A., Genové, G., Mäe, M., Nisancioglu, M. H., Wallgard, E., Niaudet, C., He, L., Norlin, J., Lindblom, P., Strittmatter, K., Johansson, B. R., & Betsholtz, C. (2010). Pericytes regulate the blood–brain barrier. *Nature*, *468*(7323), Article 7323. https://doi.org/10.1038/nature09522

Baek, H., Pahk, K. J., Kim, M.-J., Youn, I., & Kim, H. (2018). Modulation of Cerebellar Cortical Plasticity Using Low-Intensity Focused Ultrasound for Poststroke Sensorimotor Function Recovery. *Neurorehabilitation and Neural Repair*, *32*(9), 777–787. https://doi.org/10.1177/1545968318790022

Bakay, L., Hueter, T. F., Ballantine, H. T., JR., & Sosa, D. (1956). Ultrasonically Produced Changes in the Blood-Brain Barrier. *A.M.A. Archives of Neurology & Psychiatry*, *76*(5), 457–467. https://doi.org/10.1001/archneurpsyc.1956.02330290001001

Ballantine, H. T., Bell, E., & Manlapaz, J. (1960). Progress and Problems in the Neurological Applications of Focused Ultrasound. *Journal of Neurosurgery*, *17*(5), 858–876. https://doi.org/10.3171/jns.1960.17.5.0858

Bandyopadhyay, S., Quinn, T. J., Scandiuzzi, L., Basu, I., Partanen, A., Tomé, W. A., Macian, F., & Guha, C. (2016). Low-Intensity Focused Ultrasound Induces Reversal of Tumor-Induced T Cell Tolerance and Prevents Immune Escape. *Journal of Immunology (Baltimore, Md.: 1950)*, *196*(4), 1964–1976. https://doi.org/10.4049/jimmunol.1500541

Bankhead, P., Loughrey, M. B., Fernández, J. A., Dombrowski, Y., McArt, D. G., Dunne, P. D., McQuaid, S., Gray, R. T., Murray, L. J., Coleman, H. G., James, J. A., Salto-Tellez, M., & Hamilton, P. W. (2017). QuPath: Open source software for digital pathology image analysis. *Scientific Reports*, *7*, 16878. https://doi.org/10.1038/s41598-017-17204-5

Bard, F., Cannon, C., Barbour, R., Burke, R.-L., Games, D., Grajeda, H., Guido, T., Hu, K., Huang, J., Johnson-Wood, K., Khan, K., Kholodenko, D., Lee, M., Lieberburg, I., Motter, R., Nguyen, M., Soriano, F., Vasquez, N., Weiss, K., … Yednock, T. (2000). Peripherally administered antibodies against amyloid β-peptide enter the central nervous system and reduce pathology in a mouse model of Alzheimer disease. *Nature Medicine*, *6*(8), Article 8. https://doi.org/10.1038/78682

Bathini, P., Sun, T., Schenk, M., Schilling, S., McDannold, N. J., & Lemere, C. A. (2022). Acute Effects of Focused Ultrasound-Induced Blood-Brain Barrier Opening on Anti-Pyroglu3

Abeta Antibody Delivery and Immune Responses. *Biomolecules*, *12*(7), 951. https://doi.org/10.3390/biom12070951

Bisht, K., Okojie, K. A., Sharma, K., Lentferink, D. H., Sun, Y.-Y., Chen, H.-R., Uweru, J. O., Amancherla, S., Calcuttawala, Z., Campos-Salazar, A. B., Corliss, B., Jabbour, L., Benderoth, J., Friestad, B., Mills, W. A., Isakson, B. E., Tremblay, M.-È., Kuan, C.-Y., & Eyo, U. B. (2021). Capillary-associated microglia regulate vascular structure and function through PANX1-P2RY12 coupling in mice. *Nature Communications*, *12*(1), Article 1. https://doi.org/10.1038/s41467-021-25590-8

Bisht, K., Sharma, K. P., Lecours, C., Sánchez, M. G., El Hajj, H., Milior, G., Olmos-Alonso, A., Gómez-Nicola, D., Luheshi, G., Vallières, L., Branchi, I., Maggi, L., Limatola, C., Butovsky, O., & Tremblay, M.-È. (2016). Dark microglia: A new phenotype predominantly associated with pathological states. *Glia*, *64*(5), 826–839. https://doi.org/10.1002/glia.22966

Blackmore, D. G., Razansky, D., & Götz, J. (2023). Ultrasound as a versatile tool for short- and long-term improvement and monitoring of brain function. *Neuron*, *111*(8), 1174–1190. https://doi.org/10.1016/j.neuron.2023.02.018

Bobola, M., Chen, L., Ezeokeke, C., Olmstead, T., Nguyen, C., Sahota, A., Williams, R., & Mourad, P. (2020). Transcranial focused ultrasound, pulsed at 40 Hz, activates microglia acutely and reduces Aβ load, chronically, as demonstrated in vivo. *Brain Stimulation*, *13*(4), 1014–1023. https://doi.org/10.1016/j.brs.2020.03.016

Bolasco, G., Weinhard, L., Boissonnet, T., Neujahr, R., & Gross, C. T. (2018). Three-Dimensional Nanostructure of an Intact Microglia Cell. *Frontiers in Neuroanatomy*, *12*, 105. https://doi.org/10.3389/fnana.2018.00105

Bond, A. E., Shah, B. B., Huss, D. S., Dallapiazza, R. F., Warren, A., Harrison, M. B., Sperling, S. A., Wang, X.-Q., Gwinn, R., Witt, J., Ro, S., & Elias, W. J. (2017). Safety and Efficacy of Focused Ultrasound Thalamotomy for Patients With Medication-Refractory, Tremor-Dominant Parkinson Disease. *JAMA Neurology*, *74*(12), 1412–1418. https://doi.org/10.1001/jamaneurol.2017.3098

Bordeleau, M., Carrier, M., Luheshi, G. N., & Tremblay, M.-È. (2019). Microglia along sex lines: From brain colonization, maturation and function, to implication in neurodevelopmental disorders. *Seminars in Cell & Developmental Biology*, *94*, 152–163. https://doi.org/10.1016/j.semcdb.2019.06.001

Bordeleau, M., Fernández de Cossío, L., Lacabanne, C., Savage, J. C., Vernoux, N., Chakravarty, M., & Tremblay, M.-È. (2021). Maternal high-fat diet modifies myelin organization, microglial interactions, and results in social memory and sensorimotor gating deficits in adolescent mouse offspring. *Brain, Behavior, & Immunity - Health*, *15*, 100281. https://doi.org/10.1016/j.bbih.2021.100281

Bordeleau, M., Lacabanne, C., Fernández de Cossío, L., Vernoux, N., Savage, J. C., González-Ibáñez, F., & Tremblay, M.-È. (2020). Microglial and peripheral immune priming is partially sexually dimorphic in adolescent mouse offspring exposed to maternal high-fat diet. *Journal of Neuroinflammation*, *17*(1), 264. https://doi.org/10.1186/s12974-020-01914-1

Bosch, L. F. P., & Kierdorf, K. (2022). The Shape of μ—How Morphological Analyses Shape the Study of Microglia. *Frontiers in Cellular Neuroscience*, *16*, 942462. https://doi.org/10.3389/fncel.2022.942462

Bowyer, J. F., Sarkar, S., Burks, S. M., Hess, J. N., Tolani, S., O'Callaghan, J. P., & Hanig, J. P. (2020). Microglial activation and responses to vasculature that result from an acute LPS exposure. *Neurotoxicology*, *77*, 181–192. https://doi.org/10.1016/j.neuro.2020.01.014

Brazil, M. I., Chung, H., & Maxfield, F. R. (2000). Effects of Incorporation of Immunoglobulin G and Complement Component C1q on Uptake and Degradation of Alzheimer's Disease Amyloid Fibrils by Microglia *. *Journal of Biological Chemistry*, *275*(22), 16941–16947. https://doi.org/10.1074/jbc.M000937200

Burgess, A., Dubey, S., Yeung, S., Hough, O., Eterman, N., Aubert, I., & Hynynen, K. (2014). Alzheimer Disease in a Mouse Model: MR Imaging–guided Focused Ultrasound Targeted to the Hippocampus Opens the Blood-Brain Barrier and Improves Pathologic Abnormalities and Behavior. *Radiology*, *273*(3), 736–745. https://doi.org/10.1148/radiol.14140245

Burks, S. R., Ziadloo, A., Hancock, H. A., Chaudhry, A., Dean, D. D., Lewis, B. K., Frenkel, V., & Frank, J. A. (2011). Investigation of Cellular and Molecular Responses to Pulsed Focused Ultrasound in a Mouse Model. *PLOS ONE*, *6*(9), e24730. https://doi.org/10.1371/journal.pone.0024730

Cammalleri, A., Croce, P., Lee, W., Yoon, K., & Yoo, S.-S. (2020). Therapeutic potentials of localized blood-brain barrier disruption by non-invasive transcranial focused ultrasound: A technical review. *Journal of Clinical Neurophysiology : Official Publication of the American Electroencephalographic Society*, *37*(2), 104–117. https://doi.org/10.1097/WNP.0000000000000488

Carrier, M., Robert, M.-È., González Ibáñez, F., Desjardins, M., & Tremblay, M.-È. (2020). Imaging the Neuroimmune Dynamics Across Space and Time. *Frontiers in Neuroscience*, *14*, 903. https://doi.org/10.3389/fnins.2020.00903

Cartier, L., Hartley, O., Dubois-Dauphin, M., & Krause, K.-H. (2005). Chemokine receptors in the central nervous system: Role in brain inflammation and neurodegenerative diseases. *Brain Research. Brain Research Reviews*, *48*(1), 16–42. https://doi.org/10.1016/j.brainresrev.2004.07.021

Castle, M. J., Baltanás, F. C., Kovacs, I., Nagahara, A. H., Barba, D., & Tuszynski, M. H. (2020). Postmortem Analysis in a Clinical Trial of AAV2-NGF Gene Therapy for Alzheimer's Disease Identifies a Need for Improved Vector Delivery. *Human Gene Therapy*, *31*(7–8), 415–422. https://doi.org/10.1089/hum.2019.367

Chang, E.-L., Ting, C.-Y., Hsu, P.-H., Lin, Y.-C., Liao, E.-C., Huang, C.-Y., Chang, Y.-C., Chan, H.-L., Chiang, C.-S., Liu, H.-L., Wei, K.-C., Fan, C.-H., & Yeh, C.-K. (2017). Angiogenesis-targeting microbubbles combined with ultrasound-mediated gene therapy in brain tumors. *Journal of Controlled Release: Official Journal of the Controlled Release Society*, *255*, 164–175. https://doi.org/10.1016/j.jconrel.2017.04.010

Chen, H., & Konofagou, E. E. (2014). The size of blood–brain barrier opening induced by focused ultrasound is dictated by the acoustic pressure. *Journal of Cerebral Blood Flow & Metabolism*, *34*(7), 1197–1204. https://doi.org/10.1038/jcbfm.2014.71

Chen, Y., Hong, T., Chen, F., Sun, Y., Wang, Y., & Cui, L. (2021). Interplay Between Microglia and Alzheimer's Disease—Focus on the Most Relevant Risks: APOE Genotype, Sex and Age. *Frontiers in Aging Neuroscience*, *13*, 631827. https://doi.org/10.3389/fnagi.2021.631827

Cho, H., Lee, H.-Y., Han, M., Choi, J.-R., Ahn, S., Lee, T., Chang, Y., & Park, J. (2016). Localized Down-regulation of P-glycoprotein by Focused Ultrasound and Microbubbles induced Blood-Brain Barrier Disruption in Rat Brain. *Scientific Reports*, *6*, 31201. https://doi.org/10.1038/srep31201

Choi, H. J., Han, M., Seo, H., Park, C. Y., Lee, E.-H., & Park, J. (2022). The new insight into the inflammatory response following focused ultrasound-mediated blood–brain barrier disruption. *Fluids and Barriers of the CNS*, *19*(1), 103. https://doi.org/10.1186/s12987-022-00402-3

Choi, I., Wang, M., Yoo, S., Xu, P., Seegobin, S. P., Li, X., Han, X., Wang, Q., Peng, J., Zhang, B., & Yue, Z. (2023). Autophagy enables microglia to engage amyloid plaques and prevents microglial senescence. *Nature Cell Biology*, 1–12. https://doi.org/10.1038/s41556-023-01158-0

Choi, J. J., Wang, S., Tung, Y.-S., Morrison, B., & Konofagou, E. E. (2010). Molecules of various pharmacologically-relevant sizes can cross the ultrasound-induced blood-brain barrier opening in vivo. *Ultrasound in Medicine & Biology*, *36*(1), 58–67. https://doi.org/10.1016/j.ultrasmedbio.2009.08.006

Colombo, G., Cubero, R. J. A., Kanari, L., Venturino, A., Schulz, R., Scolamiero, M., Agerberg, J., Mathys, H., Tsai, L.-H., Chachólski, W., Hess, K., & Siegert, S. (2022). A tool for mapping microglial morphology, morphOMICs, reveals brain-region and sex-dependent phenotypes. *Nature Neuroscience*, *25*(10), Article 10. https://doi.org/10.1038/s41593-022-01167-6

Cooper, M. D., & Alder, M. N. (2006). The Evolution of Adaptive Immune Systems. *Cell*, *124*(4), 815–822. https://doi.org/10.1016/j.cell.2006.02.001

Császár, E., Lénárt, N., Cserép, C., Környei, Z., Fekete, R., Pósfai, B., Balázsfi, D., Hangya, B., Schwarcz, A. D., Szabadits, E., Szöllősi, D., Szigeti, K., Máthé, D., West, B. L., Sviatkó, K., Brás, A. R., Mariani, J.-C., Kliewer, A., Lenkei, Z., … Dénes, Á. (2022). Microglia modulate blood flow, neurovascular coupling, and hypoperfusion via purinergic actions. *The Journal of Experimental Medicine*, *219*(3), e20211071. https://doi.org/10.1084/jem.20211071

Cserép, C., Pósfai, B., Lénárt, N., Fekete, R., László, Z. I., Lele, Z., Orsolits, B., Molnár, G., Heindl, S., Schwarcz, A. D., Ujvári, K., Környei, Z., Tóth, K., Szabadits, E., Sperlágh, B., Baranyi, M., Csiba, L., Hortobágyi, T., Maglóczky, Z., … Dénes, Á. (2020). Microglia monitor and protect neuronal function through specialized somatic purinergic junctions. *Science (New York, N.Y.)*, *367*(6477), 528–537. https://doi.org/10.1126/science.aax6752

De Felice, E., Gonçalves de Andrade, E., Golia, M. T., González Ibáñez, F., Khakpour, M., Di Castro, M. A., Garofalo, S., Di Pietro, E., Benatti, C., Brunello, N., Tascedda, F., Kaminska, B., Limatola, C., Ragozzino, D., Tremblay, M. E., Alboni, S., & Maggi, L. (2022). Microglial diversity along the hippocampal longitudinal axis impacts synaptic plasticity in adult male mice under homeostatic conditions. *Journal of Neuroinflammation*, *19*(1), 292. https://doi.org/10.1186/s12974-022-02655-z

De Santis, P., Sette, D., & Wanderlingh, F. (2005). Cavitation Detection: The Use of the Subharmonics. *The Journal of the Acoustical Society of America*, *42*(2), 514–516. https://doi.org/10.1121/1.1910611

De Schepper, S., Ge, J. Z., Crowley, G., Ferreira, L. S. S., Garceau, D., Toomey, C. E., Sokolova, D., Rueda-Carrasco, J., Shin, S.-H., Kim, J.-S., Childs, T., Lashley, T.,

Burden, J. J., Sasner, M., Sala Frigerio, C., Jung, S., & Hong, S. (2023). Perivascular cells induce microglial phagocytic states and synaptic engulfment via SPP1 in mouse models of Alzheimer's disease. *Nature Neuroscience*, *26*(3), Article 3. https://doi.org/10.1038/s41593-023-01257-z

Deczkowska, A., Keren-Shaul, H., Weiner, A., Colonna, M., Schwartz, M., & Amit, I. (2018). Disease-Associated Microglia: A Universal Immune Sensor of Neurodegeneration. *Cell*, *173*(5), 1073–1081. https://doi.org/10.1016/j.cell.2018.05.003

Deng, J., Huang, Q., Wang, F., Liu, Y., Wang, Z., Wang, Z., Zhang, Q., Lei, B., & Cheng, Y. (2012). The role of caveolin-1 in blood-brain barrier disruption induced by focused ultrasound combined with microbubbles. *Journal of Molecular Neuroscience: MN*, *46*(3), 677–687. https://doi.org/10.1007/s12031-011-9629-9

Dubey, S., Heinen, S., Krantic, S., McLaurin, J., Branch, D. R., Hynynen, K., & Aubert, I. (2020). Clinically approved IVIg delivered to the hippocampus with focused ultrasound promotes neurogenesis in a model of Alzheimer's disease. *Proceedings of the National Academy of Sciences*, *117*(51), 32691–32700. https://doi.org/10.1073/pnas.1908658117

Dumas, A. A., Borst, K., & Prinz, M. (2021). Current tools to interrogate microglial biology. *Neuron*, *109*(18), 2805–2819. https://doi.org/10.1016/j.neuron.2021.07.004

Dungrawala, H., Manukyan, A., & Schneider, B. L. (2010). Gene Regulation: Global Transcription Rates Scale with Size. *Current Biology*, *20*(22), R979–R981. https://doi.org/10.1016/j.cub.2010.09.064

Dyne, E., Cawood, M., Suzelis, M., Russell, R., & Kim, M.-H. (2022). Ultrastructural analysis of the morphological phenotypes of microglia associated with neuroinflammatory cues.

Journal of Comparative Neurology, *530*(8), 1263–1275. https://doi.org/10.1002/cne.25274

Efthymiou, A. G., & Goate, A. M. (2017). Late onset Alzheimer's disease genetics implicates microglial pathways in disease risk. *Molecular Neurodegeneration*, *12*, 43. https://doi.org/10.1186/s13024-017-0184-x

El Hajj, H., Savage, J. C., Bisht, K., Parent, M., Vallières, L., Rivest, S., & Tremblay, M.-È. (2019). Ultrastructural evidence of microglial heterogeneity in Alzheimer's disease amyloid pathology. *Journal of Neuroinflammation*, *16*(1), 87. https://doi.org/10.1186/s12974-019-1473-9

Elias, W. J., Huss, D., Voss, T., Loomba, J., Khaled, M., Zadicario, E., Frysinger, R. C., Sperling, S. A., Wylie, S., Monteith, S. J., Druzgal, J., Shah, B. B., Harrison, M., & Wintermark, M. (2013). A Pilot Study of Focused Ultrasound Thalamotomy for Essential Tremor. *New England Journal of Medicine*, *369*(7), 640–648. https://doi.org/10.1056/NEJMoa1300962

Elmore, M. R. P., Najafi, A. R., Koike, M. A., Dagher, N. N., Spangenberg, E. E., Rice, R. A., Kitazawa, M., Matusow, B., Nguyen, H., West, B. L., & Green, K. N. (2014). Colony-stimulating factor 1 receptor signaling is necessary for microglia viability, unmasking a microglia progenitor cell in the adult brain. *Neuron*, *82*(2), 380–397. https://doi.org/10.1016/j.neuron.2014.02.040

Engelhardt, B. (2003). Development of the blood-brain barrier. *Cell and Tissue Research*, *314*(1), 119–129. https://doi.org/10.1007/s00441-003-0751-z

Enlow, W., Bordeleau, M., Piret, J., Ibáñez, F. G., Uyar, O., Venable, M.-C., Goyette, N., Carbonneau, J., Tremblay, M.-E., & Boivin, G. (2021). Microglia are involved in

phagocytosis and extracellular digestion during Zika virus encephalitis in young adult immunodeficient mice. *Journal of Neuroinflammation*, *18*, 178. https://doi.org/10.1186/s12974-021-02221-z

Erickson, M. A., Shulyatnikova, T., Banks, W. A., & Hayden, M. R. (2023). Ultrastructural Remodeling of the Blood–Brain Barrier and Neurovascular Unit by Lipopolysaccharide-Induced Neuroinflammation. *International Journal of Molecular Sciences*, *24*(2), 1640. https://doi.org/10.3390/ijms24021640

Eyo, U. B., Mo, M., Yi, M.-H., Murugan, M., Liu, J., Yarlagadda, R., Margolis, D. J., Xu, P., & Wu, L.-J. (2018). P2Y12R-Dependent Translocation Mechanisms Gate the Changing Microglial Landscape. *Cell Reports*, *23*(4), 959–966. https://doi.org/10.1016/j.celrep.2018.04.001

Ezan, P., André, P., Cisternino, S., Saubaméa, B., Boulay, A.-C., Doutremer, S., Thomas, M.-A., Quenech'du, N., Giaume, C., & Cohen-Salmon, M. (2012). Deletion of astroglial connexins weakens the blood–brain barrier. *Journal of Cerebral Blood Flow & Metabolism*, *32*(8), 1457–1467. https://doi.org/10.1038/jcbfm.2012.45

Fanselow, M. S., & Dong, H.-W. (2010). Are The Dorsal and Ventral Hippocampus functionally distinct structures? *Neuron*, *65*(1), 7. https://doi.org/10.1016/j.neuron.2009.11.031

Fattorelli, N., Martinez-Muriana, A., Wolfs, L., Geric, I., De Strooper, B., & Mancuso, R. (2021). Stem-cell-derived human microglia transplanted into mouse brain to study human disease. *Nature Protocols*, *16*(2), 1013–1033. https://doi.org/10.1038/s41596-020-00447-4

Faul, F., Erdfelder, E., Lang, A.-G., & Buchner, A. (2007). G*Power 3: A flexible statistical power analysis program for the social, behavioral, and biomedical sciences. *Behavior Research Methods*, *39*(2), 175–191. https://doi.org/10.3758/bf03193146

Feigin, V. L., Vos, T., Nichols, E., Owolabi, M. O., Carroll, W. M., Dichgans, M., Deuschl, G., Parmar, P., Brainin, M., & Murray, C. (2020). The global burden of neurological disorders: Translating evidence into policy. *The Lancet. Neurology*, *19*(3), 255–265. https://doi.org/10.1016/S1474-4422(19)30411-9

Fini, M., & Tyler, W. J. (2017). Transcranial focused ultrasound: A new tool for non-invasive neuromodulation. *International Review of Psychiatry (Abingdon, England)*, *29*(2), 168–177. https://doi.org/10.1080/09540261.2017.1302924

Fontana, F., Iberite, F., Cafarelli, A., Aliperta, A., Baldi, G., Gabusi, E., Dolzani, P., Cristino, S., Lisignoli, G., Pratellesi, T., Dumont, E., & Ricotti, L. (2021). Development and validation of low-intensity pulsed ultrasound systems for highly controlled in vitro cell stimulation. *Ultrasonics*, *116*, 106495. https://doi.org/10.1016/j.ultras.2021.106495

Fuhrmann, M., Bittner, T., Jung, C. K. E., Burgold, S., Page, R. M., Mitteregger, G., Haass, C., LaFerla, F. M., Kretzschmar, H., & Herms, J. (2010). Microglial Cx3cr1 knockout prevents neuron loss in a mouse model of Alzheimer's disease. *Nature Neuroscience*, *13*(4), 411–413. https://doi.org/10.1038/nn.2511

Galloway, D. A., Phillips, A. E. M., Owen, D. R. J., & Moore, C. S. (2019). Phagocytosis in the Brain: Homeostasis and Disease. *Frontiers in Immunology*, *10*. https://www.frontiersin.org/articles/10.3389/fimmu.2019.00790

Gerstenblith, M. R., Antony, A. K., Junkins-Hopkins, J. M., & Abuav, R. (2012). Pompholyx and eczematous reactions associated with intravenous immunoglobulin therapy. *Journal*

of the American Academy of Dermatology, *66*(2), 312–316. https://doi.org/10.1016/j.jaad.2010.12.034

Gomes, L. C., Di Benedetto, G., & Scorrano, L. (2011). During autophagy mitochondria elongate, are spared from degradation and sustain cell viability. *Nature Cell Biology*, *13*(5), 589–598. https://doi.org/10.1038/ncb2220

Gonçalves de Andrade, E., González Ibáñez, F., & Tremblay, M.-È. (2022). Microglia as a Hub for Suicide Neuropathology: Future Investigation and Prevention Targets. *Frontiers in Cellular Neuroscience*, *16*. https://www.frontiersin.org/articles/10.3389/fncel.2022.839396

González Ibanez, F., Picard, K., Bordeleau, M., Sharma, K., Bisht, K., & Tremblay, M.-È. (2019). Immunofluorescence Staining Using IBA1 and TMEM119 for Microglial Density, Morphology and Peripheral Myeloid Cell Infiltration Analysis in Mouse Brain. *Journal of Visualized Experiments: JoVE*, *152*. https://doi.org/10.3791/60510

Goyal, M. S., Blazey, T., Metcalf, N. V., McAvoy, M. P., Strain, J. F., Rahmani, M., Durbin, T. J., Xiong, C., Benzinger, T. L.-S., Morris, J. C., Raichle, M. E., & Vlassenko, A. G. (2023). Brain aerobic glycolysis and resilience in Alzheimer disease. *Proceedings of the National Academy of Sciences*, *120*(7), e2212256120. https://doi.org/10.1073/pnas.2212256120

Green, K. N., Crapser, J. D., & Hohsfield, L. A. (2020). To Kill a Microglia: A Case for CSF1R Inhibitors. *Trends in Immunology*, *41*(9), 771–784. https://doi.org/10.1016/j.it.2020.07.001

Hammond, B. P., Manek, R., Kerr, B. J., Macauley, M. S., & Plemel, J. R. (2021). Regulation of microglia population dynamics throughout development, health, and disease. *Glia*, *69*(12), 2771–2797. https://doi.org/10.1002/glia.24047

Haruwaka, K., Ikegami, A., Tachibana, Y., Ohno, N., Konishi, H., Hashimoto, A., Matsumoto, M., Kato, D., Ono, R., Kiyama, H., Moorhouse, A. J., Nabekura, J., & Wake, H. (2019). Dual microglia effects on blood brain barrier permeability induced by systemic inflammation. *Nature Communications*, *10*, 5816. https://doi.org/10.1038/s41467-019-13812-z

Hoffman, B. U., Baba, Y., Lee, S. A., Tong, C.-K., Konofagou, E. E., & Lumpkin, E. A. (2022). Focused ultrasound excites action potentials in mammalian peripheral neurons in part through the mechanically gated ion channel PIEZO2. *Proceedings of the National Academy of Sciences of the United States of America*, *119*(21), e2115821119. https://doi.org/10.1073/pnas.2115821119

Hong, I., & Kaang, B.-K. (2022). The complexity of ventral CA1 and its multiple functionalities. *Genes, Brain and Behavior*, *21*(7), e12826. https://doi.org/10.1111/gbb.12826

Hristovska, I., Robert, M., Combet, K., Honnorat, J., Comte, J.-C., & Pascual, O. (2022). Sleep decreases neuronal activity control of microglial dynamics in mice. *Nature Communications*, *13*(1), Article 1. https://doi.org/10.1038/s41467-022-34035-9

Hui, C. W., St-Pierre, A., El Hajj, H., Remy, Y., Hébert, S. S., Luheshi, G. N., Srivastava, L. K., & Tremblay, M.-È. (2018). Prenatal Immune Challenge in Mice Leads to Partly Sex-Dependent Behavioral, Microglial, and Molecular Abnormalities Associated with Schizophrenia. *Frontiers in Molecular Neuroscience*, *11*, 13. https://doi.org/10.3389/fnmol.2018.00013

Hynynen, K., McDannold, N., Sheikov, N. A., Jolesz, F. A., & Vykhodtseva, N. (2005). Local and reversible blood-brain barrier disruption by noninvasive focused ultrasound at frequencies suitable for trans-skull sonications. *NeuroImage*, *24*(1), 12–20. https://doi.org/10.1016/j.neuroimage.2004.06.046

Hynynen, K., McDannold, N., Vykhodtseva, N., & Jolesz, F. A. (2001). Noninvasive MR imaging-guided focal opening of the blood-brain barrier in rabbits. *Radiology*, *220*(3), 640–646. https://doi.org/10.1148/radiol.2202001804

Iacoponi, F., Cafarelli, A., Fontana, F., Pratellesi, T., Dumont, E., Barravecchia, I., Angeloni, D., & Ricotti, L. (2023). Optimal low-intensity pulsed ultrasound stimulation for promoting anti-inflammatory effects in macrophages. *APL Bioengineering*, *7*(1), 016114. https://doi.org/10.1063/5.0137881

Jalali, S., Huang, Y., Dumont, D. J., & Hynynen, K. (2010). Focused ultrasound-mediated bbb disruption is associated with an increase in activation of AKT: Experimental study in rats. *BMC Neurology*, *10*, 114. https://doi.org/10.1186/1471-2377-10-114

Janda, E., Boi, L., & Carta, A. R. (2018). Microglial Phagocytosis and Its Regulation: A Therapeutic Target in Parkinson's Disease? *Frontiers in Molecular Neuroscience*, *11*. https://www.frontiersin.org/articles/10.3389/fnmol.2018.00144

Jäntti, H., Sitnikova, V., Ishchenko, Y., Shakirzyanova, A., Giudice, L., Ugidos, I. F., Gómez-Budia, M., Korvenlaita, N., Ohtonen, S., Belaya, I., Fazaludeen, F., Mikhailov, N., Gotkiewicz, M., Ketola, K., Lehtonen, Š., Koistinaho, J., Kanninen, K. M., Hernández, D., Pébay, A., … Malm, T. (2022). Microglial amyloid beta clearance is driven by PIEZO1 channels. *Journal of Neuroinflammation*, *19*, 147. https://doi.org/10.1186/s12974-022-02486-y

Ji, R., Karakatsani, M. E., Burgess, M., Smith, M., Murillo, M. F., & Konofagou, E. E. (2021). Cavitation-modulated inflammatory response following focused ultrasound blood-brain barrier opening. *Journal of Controlled Release*, *337*, 458–471. https://doi.org/10.1016/j.jconrel.2021.07.042

Jia, J., Yang, L., Chen, Y., Zheng, L., Chen, Y., Xu, Y., & Zhang, M. (2022). The Role of Microglial Phagocytosis in Ischemic Stroke. *Frontiers in Immunology*, *12*. https://www.frontiersin.org/articles/10.3389/fimmu.2021.790201

Jinno, S., Klausberger, T., Marton, L. F., Dalezios, Y., Roberts, J. D. B., Fuentealba, P., Bushong, E. A., Henze, D., Buzsáki, G., & Somogyi, P. (2007). Neuronal Diversity in GABAergic Long-Range Projections from the Hippocampus. *Journal of Neuroscience*, *27*(33), 8790–8804. https://doi.org/10.1523/JNEUROSCI.1847-07.2007

Joost, E., Jordão, M. J. C., Mages, B., Prinz, M., Bechmann, I., & Krueger, M. (2019). Microglia contribute to the glia limitans around arteries, capillaries and veins under physiological conditions, in a model of neuroinflammation and in human brain tissue. *Brain Structure & Function*, *224*(3), 1301–1314. https://doi.org/10.1007/s00429-019-01834-8

Jordão, J. F., Ayala-Grosso, C. A., Markham, K., Huang, Y., Chopra, R., McLaurin, J., Hynynen, K., & Aubert, I. (2010). Antibodies Targeted to the Brain with Image-Guided Focused Ultrasound Reduces Amyloid-β Plaque Load in the TgCRND8 Mouse Model of Alzheimer's Disease. *PLoS ONE*, *5*(5), e10549. https://doi.org/10.1371/journal.pone.0010549

Jordão, J. F., Thévenot, E., Markham-Coultes, K., Scarcelli, T., Weng, Y.-Q., Xhima, K., O'Reilly, M., Huang, Y., McLaurin, J., Hynynen, K., & Aubert, I. (2013). Amyloid-β plaque reduction, endogenous antibody delivery and glial activation by brain-targeted,

transcranial focused ultrasound. *Experimental Neurology*, *248*, 16–29. https://doi.org/10.1016/j.expneurol.2013.05.008

Ju, F., Ran, Y., Zhu, L., Cheng, X., Gao, H., Xi, X., Yang, Z., & Zhang, S. (2018). Increased BBB Permeability Enhances Activation of Microglia and Exacerbates Loss of Dendritic Spines After Transient Global Cerebral Ischemia. *Frontiers in Cellular Neuroscience*, *12*, 236. https://doi.org/10.3389/fncel.2018.00236

Jung, S., & Schwartz, M. (2012). Non-Identical Twins – Microglia and Monocyte-Derived Macrophages in Acute Injury and Autoimmune Inflammation. *Frontiers in Immunology*, *3*, 89. https://doi.org/10.3389/fimmu.2012.00089

Karakatsani, M. E., Kugelman, T., Ji, R., Murillo, M., Wang, S., Niimi, Y., Small, S. A., Duff, K. E., & Konofagou, E. E. (2019). Unilateral Focused Ultrasound-Induced Blood-Brain Barrier Opening Reduces Phosphorylated Tau from The rTg4510 Mouse Model. *Theranostics*, *9*(18), 5396–5411. https://doi.org/10.7150/thno.28717

Karperien, A., Ahammer, H., & Jelinek, H. (2013). Quantitating the subtleties of microglial morphology with fractal analysis. *Frontiers in Cellular Neuroscience*, *7*. https://www.frontiersin.org/articles/10.3389/fncel.2013.00003

Katoh, M., Wu, B., Nguyen, H. B., Thai, T. Q., Yamasaki, R., Lu, H., Rietsch, A. M., Zorlu, M. M., Shinozaki, Y., Saitoh, Y., Saitoh, S., Sakoh, T., Ikenaka, K., Koizumi, S., Ransohoff, R. M., & Ohno, N. (2017). Polymorphic regulation of mitochondrial fission and fusion modifies phenotypes of microglia in neuroinflammation. *Scientific Reports*, *7*(1), Article 1. https://doi.org/10.1038/s41598-017-05232-0

Keller, D., Erö, C., & Markram, H. (2018). Cell Densities in the Mouse Brain: A Systematic Review. *Frontiers in Neuroanatomy*, *12*. https://www.frontiersin.org/articles/10.3389/fnana.2018.00083

Khakpour, M., Ibáñez, F. G., Bordeleau, M., Picard, K., Mckee-Reid, L., Ben-Azu, B., Maggi, L., & Tremblay, M.-È. (2022). Manual versus automatic analysis of microglial density and distribution: A comparison in the hippocampus of healthy and lipopolysaccharide-challenged mature male mice. *Micron*, *161*, 103334. https://doi.org/10.1016/j.micron.2022.103334

Kinoshita, M., McDannold, N., Jolesz, F. A., & Hynynen, K. (2006). Targeted delivery of antibodies through the blood-brain barrier by MRI-guided focused ultrasound. *Biochemical and Biophysical Research Communications*, *340*(4), 1085–1090. https://doi.org/10.1016/j.bbrc.2005.12.112

Kofoed, R. H., Dibia, C. L., Noseworthy, K., Xhima, K., Vacaresse, N., Hynynen, K., & Aubert, I. (2022). Efficacy of gene delivery to the brain using AAV and ultrasound depends on serotypes and brain areas. *Journal of Controlled Release: Official Journal of the Controlled Release Society*, *351*, 667–680. https://doi.org/10.1016/j.jconrel.2022.09.048

Konofagou, E. E. (2012). Optimization of the Ultrasound-Induced Blood-Brain Barrier Opening. *Theranostics*, *2*(12), 1223–1237. https://doi.org/10.7150/thno.5576

Kovacs, Z. I., Kim, S., Jikaria, N., Qureshi, F., Milo, B., Lewis, B. K., Bresler, M., Burks, S. R., & Frank, J. A. (2017). Disrupting the blood-brain barrier by focused ultrasound induces sterile inflammation. *Proceedings of the National Academy of Sciences of the United States of America*, *114*(1), E75–E84. https://doi.org/10.1073/pnas.1614777114

Kozlowski, C., & Weimer, R. M. (2012). An Automated Method to Quantify Microglia Morphology and Application to Monitor Activation State Longitudinally In Vivo. *PLoS ONE*, *7*(2), e31814. https://doi.org/10.1371/journal.pone.0031814

Kozlowski, G. P., Sterzl, I., & Nilaver, G. (1992). Localization patterns for immunoglobulins and albumins in the brain suggest diverse mechanisms for their transport across the blood-brain barrier (BBB). *Progress in Brain Research*, *91*, 149–154. https://doi.org/10.1016/s0079-6123(08)62329-8

Krishna, V., Sammartino, F., & Rezai, A. (2018). A Review of the Current Therapies, Challenges, and Future Directions of Transcranial Focused Ultrasound Technology: Advances in Diagnosis and Treatment. *JAMA Neurology*, *75*(2), 246–254. https://doi.org/10.1001/jamaneurol.2017.3129

Lane, C. A., Hardy, J., & Schott, J. M. (2018). Alzheimer's disease. *European Journal of Neurology*, *25*(1), 59–70. https://doi.org/10.1111/ene.13439

Lau, V., Ramer, L., & Tremblay, M.-È. (2023). An aging, pathology burden, and glial senescence build-up hypothesis for late onset Alzheimer's disease. *Nature Communications*, *14*(1), Article 1. https://doi.org/10.1038/s41467-023-37304-3

Lauro, C., & Limatola, C. (2020). Metabolic Reprograming of Microglia in the Regulation of the Innate Inflammatory Response. *Frontiers in Immunology*, *11*. https://www.frontiersin.org/articles/10.3389/fimmu.2020.00493

Leclech, C., Natale, C. F., & Barakat, A. I. (2020). The basement membrane as a structured surface – role in vascular health and disease. *Journal of Cell Science*, *133*(18), jcs239889. https://doi.org/10.1242/jcs.239889

Lecours, C., St-Pierre, M.-K., Picard, K., Bordeleau, M., Bourque, M., Awogbindin, I. O., Benadjal, A., Ibanez, F. G., Gagnon, D., Cantin, L., Parent, M., Di Paolo, T., & Tremblay, M.-E. (2020). Levodopa partially rescues microglial numerical, morphological, and phagolysosomal alterations in a monkey model of Parkinson's disease. *Brain, Behavior, and Immunity*, *90*, 81–96. https://doi.org/10.1016/j.bbi.2020.07.044

Lee, E., Eo, J.-C., Lee, C., & Yu, J.-W. (2021). Distinct Features of Brain-Resident Macrophages: Microglia and Non-Parenchymal Brain Macrophages. *Molecules and Cells*, *44*(5), 281–291. https://doi.org/10.14348/molcells.2021.0060

Lee, W., Kim, H., Jung, Y., Song, I.-U., Chung, Y. A., & Yoo, S.-S. (2015). Image-Guided Transcranial Focused Ultrasound Stimulates Human Primary Somatosensory Cortex. *Scientific Reports*, *5*, 8743. https://doi.org/10.1038/srep08743

Leinenga, G., & Götz, J. (2015). Scanning ultrasound removes amyloid-β and restores memory in an Alzheimer's disease mouse model. *Science Translational Medicine*, *7*(278), 278ra33. https://doi.org/10.1126/scitranslmed.aaa2512

Lipsman, N., Meng, Y., Bethune, A. J., Huang, Y., Lam, B., Masellis, M., Herrmann, N., Heyn, C., Aubert, I., Boutet, A., Smith, G. S., Hynynen, K., & Black, S. E. (2018). Blood–brain barrier opening in Alzheimer's disease using MR-guided focused ultrasound. *Nature Communications*, *9*, 2336. https://doi.org/10.1038/s41467-018-04529-6

Lituma, P. J., Woo, E., O'Hara, B. F., Castillo, P. E., Sibinga, N. E. S., & Nandi, S. (2021). Altered synaptic connectivity and brain function in mice lacking microglial adapter protein Iba1. *Proceedings of the National Academy of Sciences of the United States of America*, *118*(46), e2115539118. https://doi.org/10.1073/pnas.2115539118

Liu, H.-L., Hsieh, H.-Y., Lu, L.-A., Kang, C.-W., Wu, M.-F., & Lin, C.-Y. (2012). Low-pressure pulsed focused ultrasound with microbubbles promotes an anticancer immunological response. *Journal of Translational Medicine*, *10*, 221. https://doi.org/10.1186/1479-5876-10-221

Liu, H.-L., Hua, M.-Y., Chen, P.-Y., Chu, P.-C., Pan, C.-H., Yang, H.-W., Huang, C.-Y., Wang, J.-J., Yen, T.-C., & Wei, K.-C. (2010). Blood-brain barrier disruption with focused ultrasound enhances delivery of chemotherapeutic drugs for glioblastoma treatment. *Radiology*, *255*(2), 415–425. https://doi.org/10.1148/radiol.10090699

Lou, N., Takano, T., Pei, Y., Xavier, A. L., Goldman, S. A., & Nedergaard, M. (2016). Purinergic receptor P2RY12-dependent microglial closure of the injured blood–brain barrier. *Proceedings of the National Academy of Sciences of the United States of America*, *113*(4), 1074–1079. https://doi.org/10.1073/pnas.1520398113

Lounas, A., Lebrun, A., Laflamme, I., Vernoux, N., Savage, J., Tremblay, M.-È., Germain, M., & Richard, F. J. (2022). A 3D analysis revealed complexe mitochondria morphologies in porcine cumulus cells. *Scientific Reports*, *12*(1), Article 1. https://doi.org/10.1038/s41598-022-19723-2

Lynn, J. G., Zwemer, R. L., Chick, A. J., & Miller, A. E. (1942). A NEW METHOD FOR THE GENERATION AND USE OF FOCUSED ULTRASOUND IN EXPERIMENTAL BIOLOGY. *The Journal of General Physiology*, *26*(2), 179–193.

Mainprize, T., Lipsman, N., Huang, Y., Meng, Y., Bethune, A., Ironside, S., Heyn, C., Alkins, R., Trudeau, M., Sahgal, A., Perry, J., & Hynynen, K. (2019). Blood-Brain Barrier Opening in Primary Brain Tumors with Non-invasive MR-Guided Focused Ultrasound:

A Clinical Safety and Feasibility Study. *Scientific Reports*, *9*, 321. https://doi.org/10.1038/s41598-018-36340-0

Man, V. H., Li, M. S., Wang, J., Derreumaux, P., & Nguyen, P. H. (2019). Interaction mechanism between the focused ultrasound and lipid membrane at the molecular level. *The Journal of Chemical Physics*, *150*(21), 215101. https://doi.org/10.1063/1.5099008

Marguerat, S., & Bähler, J. (2012). Coordinating genome expression with cell size. *Trends in Genetics*, *28*(11), 560–565. https://doi.org/10.1016/j.tig.2012.07.003

Masuda, T., Sankowski, R., Staszewski, O., & Prinz, M. (2020). Microglia Heterogeneity in the Single-Cell Era. *Cell Reports*, *30*(5), 1271–1281. https://doi.org/10.1016/j.celrep.2020.01.010

Mathiisen, T. M., Lehre, K. P., Danbolt, N. C., & Ottersen, O. P. (2010). The perivascular astroglial sheath provides a complete covering of the brain microvessels: An electron microscopic 3D reconstruction. *Glia*, *58*(9), 1094–1103. https://doi.org/10.1002/glia.20990

McMahon, D., & Hynynen, K. (2017). Acute Inflammatory Response Following Increased Blood-Brain Barrier Permeability Induced by Focused Ultrasound is Dependent on Microbubble Dose. *Theranostics*, *7*(16), 3989–4000. https://doi.org/10.7150/thno.21630

McMahon, D., Lassus, A., Gaud, E., Jeannot, V., & Hynynen, K. (2020). Microbubble formulation influences inflammatory response to focused ultrasound exposure in the brain. *Scientific Reports*, *10*(1), 21534. https://doi.org/10.1038/s41598-020-78657-9

Mead, B. P., Kim, N., Miller, G. W., Hodges, D., Mastorakos, P., Klibanov, A. L., Mandell, J. W., Hirsh, J., Suk, J. S., Hanes, J., & Price, R. J. (2017). Novel Focused Ultrasound Gene Therapy Approach Noninvasively Restores Dopaminergic Neuron Function in a Rat

Parkinson's Disease Model. *Nano Letters*, *17*(6), 3533–3542. https://doi.org/10.1021/acs.nanolett.7b00616

Mendell, J. R., Al-Zaidy, S., Shell, R., Arnold, W. D., Rodino-Klapac, L. R., Prior, T. W., Lowes, L., Alfano, L., Berry, K., Church, K., Kissel, J. T., Nagendran, S., L'Italien, J., Sproule, D. M., Wells, C., Cardenas, J. A., Heitzer, M. D., Kaspar, A., Corcoran, S., … Kaspar, B. K. (2017). Single-Dose Gene-Replacement Therapy for Spinal Muscular Atrophy. *The New England Journal of Medicine*, *377*(18), 1713–1722. https://doi.org/10.1056/NEJMoa1706198

Mendiola, A. S., Yan, Z., Dixit, K., Johnson, J. R., Bouhaddou, M., Meyer-Franke, A., Shin, M.-G., Yong, Y., Agrawal, A., MacDonald, E., Muthukumar, G., Pearce, C., Arun, N., Cabriga, B., Meza-Acevedo, R., Alzamora, M. del P. S., Zamvil, S. S., Pico, A. R., Ryu, J. K., … Akassoglou, K. (2023). Defining blood-induced microglia functions in neurodegeneration through multiomic profiling. *Nature Immunology*, 1–15. https://doi.org/10.1038/s41590-023-01522-0

Meng, Y., Hynynen, K., & Lipsman, N. (2021). Applications of focused ultrasound in the brain: From thermoablation to drug delivery. *Nature Reviews Neurology*, *17*(1), 7–22. https://doi.org/10.1038/s41582-020-00418-z

Mills, W. A., Woo, A. M., Jiang, S., Martin, J., Surendran, D., Bergstresser, M., Kimbrough, I. F., Eyo, U. B., Sofroniew, M. V., & Sontheimer, H. (2022). Astrocyte plasticity in mice ensures continued endfoot coverage of cerebral blood vessels following injury and declines with age. *Nature Communications*, *13*, 1794. https://doi.org/10.1038/s41467-022-29475-2

Mondo, E., Becker, S. C., Kautzman, A. G., Schifferer, M., Baer, C. E., Chen, J., Huang, E. J., Simons, M., & Schafer, D. P. (2020). A Developmental Analysis of Juxtavascular Microglia Dynamics and Interactions with the Vasculature. *The Journal of Neuroscience*, *40*(34), 6503–6521. https://doi.org/10.1523/JNEUROSCI.3006-19.2020

Morini, R., Bizzotto, M., Perrucci, F., Filipello, F., & Matteoli, M. (2021). Strategies and Tools for Studying Microglial-Mediated Synapse Elimination and Refinement. *Frontiers in Immunology*, *12*. https://www.frontiersin.org/articles/10.3389/fimmu.2021.640937

Morris, G. P., Foster, C. G., Courtney, J.-M., Collins, J. M., Cashion, J. M., Brown, L. S., Howells, D. W., DeLuca, G. C., Canty, A. J., King, A. E., Ziebell, J. M., & Sutherland, B. A. (2023). Microglia directly associate with pericytes in the central nervous system. *Glia*, *71*(8), 1847–1869. https://doi.org/10.1002/glia.24371

Motulsky, H. J., & Ransnas, L. A. (1987). Fitting curves to data using nonlinear regression: A practical and nonmathematical review. *The FASEB Journal*, *1*(5), 365–374. https://doi.org/10.1096/fasebj.1.5.3315805

Muñoz-Castro, C., Mejias-Ortega, M., Sanchez-Mejias, E., Navarro, V., Trujillo-Estrada, L., Jimenez, S., Garcia-Leon, J. A., Fernandez-Valenzuela, J. J., Sanchez-Mico, M. V., Romero-Molina, C., Moreno-Gonzalez, I., Baglietto-Vargas, D., Vizuete, M., Gutierrez, A., & Vitorica, J. (2023). Monocyte-derived cells invade brain parenchyma and amyloid plaques in human Alzheimer's disease hippocampus. *Acta Neuropathologica Communications*, *11*(1), 31. https://doi.org/10.1186/s40478-023-01530-z

Nahirney, P. C., & Tremblay, M.-E. (2021). Brain Ultrastructure: Putting the Pieces Together. *Frontiers in Cell and Developmental Biology*, *9*, 629503. https://doi.org/10.3389/fcell.2021.629503

Nelson, L. H., Warden, S., & Lenz, K. M. (2017). Sex differences in microglial phagocytosis in the neonatal hippocampus. *Brain, Behavior, and Immunity*, *64*, 11–22. https://doi.org/10.1016/j.bbi.2017.03.010

Nguyen, P. T., Dorman, L. C., Pan, S., Vainchtein, I. D., Han, R. T., Nakao-Inoue, H., Taloma, S. E., Barron, J. J., Molofsky, A. B., Kheirbek, M. A., & Molofsky, A. V. (2020). Microglial Remodeling of the Extracellular Matrix Promotes Synapse Plasticity. *Cell*, *182*(2), 388-403.e15. https://doi.org/10.1016/j.cell.2020.05.050

Nichols, E., Steinmetz, J. D., Vollset, S. E., Fukutaki, K., Chalek, J., Abd-Allah, F., Abdoli, A., Abualhasan, A., Abu-Gharbieh, E., Akram, T. T., Hamad, H. A., Alahdab, F., Alanezi, F. M., Alipour, V., Almustanyir, S., Amu, H., Ansari, I., Arabloo, J., Ashraf, T., … Vos, T. (2022). Estimation of the global prevalence of dementia in 2019 and forecasted prevalence in 2050: An analysis for the Global Burden of Disease Study 2019. *The Lancet Public Health*, *7*(2), e105–e125. https://doi.org/10.1016/S2468-2667(21)00249-8

Nimmerjahn, A., Kirchhoff, F., & Helmchen, F. (2005). Resting microglial cells are highly dynamic surveillants of brain parenchyma in vivo. *Science (New York, N.Y.)*, *308*(5726), 1314–1318. https://doi.org/10.1126/science.1110647

Ohm, D. T., Fought, A. J., Rademaker, A., Kim, G., Sridhar, J., Coventry, C., Gefen, T., Weintraub, S., Bigio, E., Mesulam, M. M., Rogalski, E., & Geula, C. (2019). Neuropathologic basis of in vivo cortical atrophy in the aphasic variant of Alzheimer's disease. *Brain Pathology*, *30*(2), 332–344. https://doi.org/10.1111/bpa.12783

O'Reilly, M. A., & Hynynen, K. (2012). Blood-Brain Barrier: Real-time Feedback-controlled Focused Ultrasound Disruption by Using an Acoustic Emissions–based Controller. *Radiology*, *263*(1), 96–106. https://doi.org/10.1148/radiol.11111417

Paolicelli, R. C., Sierra, A., Stevens, B., Tremblay, M.-E., Aguzzi, A., Ajami, B., Amit, I., Audinat, E., Bechmann, I., Bennett, M., Bennett, F., Bessis, A., Biber, K., Bilbo, S., Blurton-Jones, M., Boddeke, E., Brites, D., Brône, B., Brown, G. C., … Wyss-Coray, T. (2022). Microglia states and nomenclature: A field at its crossroads. *Neuron*, *110*(21), 3458–3483. https://doi.org/10.1016/j.neuron.2022.10.020

Pardridge, W. M. (2005). The Blood-Brain Barrier: Bottleneck in Brain Drug Development. *NeuroRx*, *2*(1), 3–14.

Park, S. H., Baik, K., Jeon, S., Chang, W. S., Ye, B. S., & Chang, J. W. (2021). Extensive frontal focused ultrasound mediated blood–brain barrier opening for the treatment of Alzheimer's disease: A proof-of-concept study. *Translational Neurodegeneration*, *10*, 44. https://doi.org/10.1186/s40035-021-00269-8

Paxinos, G., & Franklin, K. B. J. (2019). *Paxinos and Franklin's the Mouse Brain in Stereotaxic Coordinates*. Academic Press.

Peters, A. (1991). The fine structure of the nervous system. *Neurons and Their Supporting Cells*, 211–218.

Petrasch-Parwez, E., Schöbel, A., Benali, A., Moinfar, Z., Förster, E., Brüne, M., & Juckel, G. (2020). Lateralization of increased density of Iba1-immunopositive microglial cells in the anterior midcingulate cortex of schizophrenia and bipolar disorder. *European Archives of Psychiatry and Clinical Neuroscience*, *270*(7), 819–828. https://doi.org/10.1007/s00406-020-01107-0

Pivoriūnas, A., & Verkhratsky, A. (2021). Astrocyte–Endotheliocyte Axis in the Regulation of the Blood–Brain Barrier. *Neurochemical Research*, *46*(10), 2538–2550. https://doi.org/10.1007/s11064-021-03338-6

Plaza-Zabala, A., Sierra-Torre, V., & Sierra, A. (2017). Autophagy and Microglia: Novel Partners in Neurodegeneration and Aging. *International Journal of Molecular Sciences*, *18*(3), 598. https://doi.org/10.3390/ijms18030598

Poon, C., Pellow, C., & Hynynen, K. (2021). Neutrophil recruitment and leukocyte response following focused ultrasound and microbubble mediated blood-brain barrier treatments. *Theranostics*, *11*(4), 1655–1671. https://doi.org/10.7150/thno.52710

Pouliopoulos, A. N., Kwon, N., Jensen, G., Meaney, A., Niimi, Y., Burgess, M. T., Ji, R., McLuckie, A. J., Munoz, F. A., Kamimura, H. A. S., Teich, A. F., Ferrera, V. P., & Konofagou, E. E. (2021). Safety evaluation of a clinical focused ultrasound system for neuronavigation guided blood-brain barrier opening in non-human primates. *Scientific Reports*, *11*(1), Article 1. https://doi.org/10.1038/s41598-021-94188-3

Prinz, M., Masuda, T., Wheeler, M. A., & Quintana, F. J. (2021). Microglia and Central Nervous System–Associated Macrophages—From Origin to Disease Modulation. *Annual Review of Immunology*, *39*, 251–277. https://doi.org/10.1146/annurev-immunol-093019-110159

Ralay Ranaivo, H., & Wainwright, M. S. (2010). Albumin activates astrocytes and microglia through mitogen-activated protein kinase pathways. *Brain Research*, *1313*, 222–231. https://doi.org/10.1016/j.brainres.2009.11.063

Ransohoff, R. M., & Perry, V. H. (2009). Microglial physiology: Unique stimuli, specialized responses. *Annual Review of Immunology*, *27*, 119–145. https://doi.org/10.1146/annurev.immunol.021908.132528

Raymond, S. B., Skoch, J., Hynynen, K., & Bacskai, B. J. (2007). Multiphoton imaging of ultrasound/Optison mediated cerebrovascular effects in vivo. *Journal of Cerebral Blood*

Flow and Metabolism: Official Journal of the International Society of Cerebral Blood Flow and Metabolism, *27*(2), 393–403. https://doi.org/10.1038/sj.jcbfm.9600336

Raymond, S. B., Treat, L. H., Dewey, J. D., McDannold, N. J., Hynynen, K., & Bacskai, B. J. (2008). Ultrasound Enhanced Delivery of Molecular Imaging and Therapeutic Agents in Alzheimer's Disease Mouse Models. *PLoS ONE*, *3*(5), e2175. https://doi.org/10.1371/journal.pone.0002175

Readnower, R. D., Chavko, M., Adeeb, S., Conroy, M. D., Pauly, J. R., McCarron, R. M., & Sullivan, P. G. (2010). Increase in Blood Brain Barrier Permeability, Oxidative Stress, and Activated Microglia in a Rat Model of Blast Induced Traumatic Brain Injury. *Journal of Neuroscience Research*, *88*(16), 3530–3539. https://doi.org/10.1002/jnr.22510

Samiotaki, G., Vlachos, F., Tung, Y.-S., Feshitan, J., Borden, M., & Konofagou, E. E. (2012). Pressure and microbubble size dependence study of focused ultrasound-induced blood-brain barrier opening reversibility in vivo. *AIP Conference Proceedings*, *1481*(1), 300–306. https://doi.org/10.1063/1.4757352

Santos, L. E., Beckman, D., & Ferreira, S. T. (2016). Microglial dysfunction connects depression and Alzheimer's disease. *Brain, Behavior, and Immunity*, *55*, 151–165. https://doi.org/10.1016/j.bbi.2015.11.011

Savage, J. C., Carrier, M., & Tremblay, M.-È. (2019). Morphology of Microglia Across Contexts of Health and Disease. *Methods in Molecular Biology (Clifton, N.J.)*, *2034*, 13–26. https://doi.org/10.1007/978-1-4939-9658-2_2

Savage, J. C., Picard, K., González-Ibáñez, F., & Tremblay, M.-È. (2018). A Brief History of Microglial Ultrastructure: Distinctive Features, Phenotypes, and Functions Discovered

Over the Past 60 Years by Electron Microscopy. *Frontiers in Immunology*, *9*, 803. https://doi.org/10.3389/fimmu.2018.00803

Savage, J. C., St-Pierre, M.-K., Hui, C. W., & Tremblay, M.-E. (2019). Microglial Ultrastructure in the Hippocampus of a Lipopolysaccharide-Induced Sickness Mouse Model. *Frontiers in Neuroscience*, *13*, 1340. https://doi.org/10.3389/fnins.2019.01340

Schafer, D. P., Lehrman, E. K., Kautzman, A. G., Koyama, R., Mardinly, A. R., Yamasaki, R., Ransohoff, R. M., Greenberg, M. E., Barres, B. A., & Stevens, B. (2012). Microglia sculpt postnatal neural circuits in an activity and complement-dependent manner. *Neuron*, *74*(4), 691–705. https://doi.org/10.1016/j.neuron.2012.03.026

Schindelin, J., Arganda-Carreras, I., Frise, E., Kaynig, V., Longair, M., Pietzsch, T., Preibisch, S., Rueden, C., Saalfeld, S., Schmid, B., Tinevez, J.-Y., White, D. J., Hartenstein, V., Eliceiri, K., Tomancak, P., & Cardona, A. (2012). Fiji—An Open Source platform for biological image analysis. *Nature Methods*, *9*(7), 10.1038/nmeth.2019. https://doi.org/10.1038/nmeth.2019

Schregel, K., Baufeld, C., Palotai, M., Meroni, R., Fiorina, P., Wuerfel, J., Sinkus, R., Zhang, Y.-Z., McDannold, N., White, P. J., & Guttmann, C. R. G. (2021). Targeted Blood Brain Barrier Opening With Focused Ultrasound Induces Focal Macrophage/Microglial Activation in Experimental Autoimmune Encephalomyelitis. *Frontiers in Neuroscience*, *15*, 665722. https://doi.org/10.3389/fnins.2021.665722

Schreiber, R. D., Old, L. J., & Smyth, M. J. (2011). Cancer immunoediting: Integrating immunity's roles in cancer suppression and promotion. *Science (New York, N.Y.)*, *331*(6024), 1565–1570. https://doi.org/10.1126/science.1203486

Segarra, M., Aburto, M. R., & Acker-Palmer, A. (2021). Blood–Brain Barrier Dynamics to Maintain Brain Homeostasis. *Trends in Neurosciences*, *44*(5), 393–405. https://doi.org/10.1016/j.tins.2020.12.002

Seng, J. S., Low, L. K., Sperlich, M., Ronis, D. L., & Liberzon, I. (2011). Posttraumatic stress disorder, child abuse history, birth weight, and gestational age: A prospective cohort study. *BJOG : An International Journal of Obstetrics and Gynaecology*, *118*(11), 1329. https://doi.org/10.1111/j.1471-0528.2011.03071.x

Shahidehpour, R. K., Nelson, A. S., Sanders, L. G., Embry, C. R., Nelson, P. T., & Bachstetter, A. D. (2023). The localization of molecularly distinct microglia populations to Alzheimer's disease pathologies using QUIVER. *Acta Neuropathologica Communications*, *11*, 45. https://doi.org/10.1186/s40478-023-01541-w

Shapson-Coe, A., Januszewski, M., Berger, D. R., Pope, A., Wu, Y., Blakely, T., Schalek, R. L., Li, P. H., Wang, S., Maitin-Shepard, J., Karlupia, N., Dorkenwald, S., Sjostedt, E., Leavitt, L., Lee, D., Bailey, L., Fitzmaurice, A., Kar, R., Field, B., … Lichtman, J. W. (2021). *A connectomic study of a petascale fragment of human cerebral cortex* (p. 2021.05.29.446289). bioRxiv. https://doi.org/10.1101/2021.05.29.446289

Sheikov, N., McDannold, N., Jolesz, F., Zhang, Y.-Z., Tam, K., & Hynynen, K. (2006). Brain arterioles show more active vesicular transport of blood-borne tracer molecules than capillaries and venules after focused ultrasound-evoked opening of the blood-brain barrier. *Ultrasound in Medicine & Biology*, *32*(9), 1399–1409. https://doi.org/10.1016/j.ultrasmedbio.2006.05.015

Sheikov, N., McDannold, N., Sharma, S., & Hynynen, K. (2008). Effect of focused ultrasound applied with an ultrasound contrast agent on the tight junctional integrity of the brain

microvascular endothelium. *Ultrasound in Medicine & Biology*, *34*(7), 1093–1104. https://doi.org/10.1016/j.ultrasmedbio.2007.12.015

Sheikov, N., McDannold, N., Vykhodtseva, N., Jolesz, F., & Hynynen, K. (2004). Cellular mechanisms of the blood-brain barrier opening induced by ultrasound in presence of microbubbles. *Ultrasound in Medicine & Biology*, *30*(7), 979–989. https://doi.org/10.1016/j.ultrasmedbio.2004.04.010

Sierra, A., Encinas, J. M., Deudero, J. J. P., Chancey, J. H., Enikolopov, G., Overstreet-Wadiche, L. S., Tsirka, S. E., & Maletic-Savatic, M. (2010). Microglia shape adult hippocampal neurogenesis through apoptosis-coupled phagocytosis. *Cell Stem Cell*, *7*(4), 483–495. https://doi.org/10.1016/j.stem.2010.08.014

Sierra, A., Paolicelli, R. C., & Kettenmann, H. (2019). Cien Años de Microglía: Milestones in a Century of Microglial Research. *Trends in Neurosciences*, *42*(11), 778–792. https://doi.org/10.1016/j.tins.2019.09.004

Sik, A., Penttonen, M., Ylinen, A., & Buzsaki, G. (1995). Hippocampal CA1 interneurons: An in vivo intracellular labeling study. *Journal of Neuroscience*, *15*(10), 6651–6665. https://doi.org/10.1523/JNEUROSCI.15-10-06651.1995

Silburt, J., & Aubert, I. (2022). MORPHIOUS: An unsupervised machine learning workflow to detect the activation of microglia and astrocytes. *Journal of Neuroinflammation*, *19*(1), 24. https://doi.org/10.1186/s12974-021-02376-9

Šimončičová, E., Andrade, E. G. de, Vecchiarelli, H. A., Awogbindin, I. O., Delage, C. I., & Tremblay, M.-È. (2022). Present and future of microglial pharmacology. *Trends in Pharmacological Sciences*, *43*(8), 669–685. https://doi.org/10.1016/j.tips.2021.11.006

Sinharay, S., Tu, T.-W., Kovacs, Z. I., Schreiber-Stainthorp, W., Sundby, M., Zhang, X., Papadakis, G. Z., Reid, W. C., Frank, J. A., & Hammoud, D. A. (2019). In vivo imaging of sterile microglial activation in rat brain after disrupting the blood-brain barrier with pulsed focused ultrasound: [18F]DPA-714 PET study. *Journal of Neuroinflammation*, *16*(1), 155. https://doi.org/10.1186/s12974-019-1543-z

Smolders, J., Schuurman, K. G., van Strien, M. E., Melief, J., Hendrickx, D., Hol, E. M., van Eden, C., Luchetti, S., & Huitinga, I. (2013). Expression of vitamin D receptor and metabolizing enzymes in multiple sclerosis-affected brain tissue. *Journal of Neuropathology and Experimental Neurology*, *72*(2), 91–105. https://doi.org/10.1097/NEN.0b013e31827f4fcc

Song, Z., Wang, Z., Shen, J., Xu, S., & Hu, Z. (2017). Nerve growth factor delivery by ultrasound-mediated nanobubble destruction as a treatment for acute spinal cord injury in rats. *International Journal of Nanomedicine*, *12*, 1717–1729. https://doi.org/10.2147/IJN.S128848

Stewart, E. A., Rabinovici, J., Tempany, C. M. C., Inbar, Y., Regan, L., Gostout, B., Hesley, G., Kim, H. S., Hengst, S., & Gedroyc, W. M. (2006). Clinical outcomes of focused ultrasound surgery for the treatment of uterine fibroids. *Fertility and Sterility*, *85*(1), 22–29. https://doi.org/10.1016/j.fertnstert.2005.04.072

St-Pierre, M.-K., Bordeleau, M., & Tremblay, M.-È. (2019). Visualizing Dark Microglia. *Methods in Molecular Biology (Clifton, N.J.)*, *2034*, 97–110. https://doi.org/10.1007/978-1-4939-9658-2_8

St-Pierre, M.-K., Carrier, M., González Ibáñez, F., Šimončičová, E., Wallman, M.-J., Vallières, L., Parent, M., & Tremblay, M.-È. (2022). Ultrastructural characterization of dark

microglia during aging in a mouse model of Alzheimer's disease pathology and in human post-mortem brain samples. *Journal of Neuroinflammation*, *19*(1), 235. https://doi.org/10.1186/s12974-022-02595-8

St-Pierre, M.-K., Šimončičová, E., Bögi, E., & Tremblay, M.-È. (2020). Shedding Light on the Dark Side of the Microglia. *ASN Neuro*, *12*, 1759091420925335. https://doi.org/10.1177/1759091420925335

Stratoulias, V., Venero, J. L., Tremblay, M.-È., & Joseph, B. (2019). Microglial subtypes: Diversity within the microglial community. *The EMBO Journal*, *38*(17), e101997. https://doi.org/10.15252/embj.2019101997

Sun, T., Shi, Q., Zhang, Y., Power, C., Hoesch, C., Antonelli, S., Schroeder, M. K., Caldarone, B. J., Taudte, N., Schenk, M., Hettmann, T., Schilling, S., McDannold, N. J., & Lemere, C. A. (2021). Focused ultrasound with anti-pGlu3 Aβ enhances efficacy in Alzheimer's disease-like mice via recruitment of peripheral immune cells. *Journal of Controlled Release*, *336*, 443–456. https://doi.org/10.1016/j.jconrel.2021.06.037

Tan, Y.-L., Yuan, Y., & Tian, L. (2020). Microglial regional heterogeneity and its role in the brain. *Molecular Psychiatry*, *25*(2), 351–367. https://doi.org/10.1038/s41380-019-0609-8

Tay, T. L., Béchade, C., D'Andrea, I., St-Pierre, M.-K., Henry, M. S., Roumier, A., & Tremblay, M.-E. (2018). Microglia Gone Rogue: Impacts on Psychiatric Disorders across the Lifespan. *Frontiers in Molecular Neuroscience*, *10*, 421. https://doi.org/10.3389/fnmol.2017.00421

Touahri, Y., Dixit, R., Kofoed, R. H., Mikloska, K., Park, E., Raeisossadati, R., Markham-Coultes, K., David, L. A., Rijal, H., Zhao, J., Lynch, M., Hynynen, K., Aubert, I., & Schuurmans, C. (2020). Focused ultrasound as a novel strategy for noninvasive gene

delivery to retinal Müller glia. *Theranostics*, *10*(7), 2982–2999. https://doi.org/10.7150/thno.42611

Tremblay, M.-È., Lowery, R. L., & Majewska, A. K. (2010). Microglial Interactions with Synapses Are Modulated by Visual Experience. *PLOS Biology*, *8*(11), e1000527. https://doi.org/10.1371/journal.pbio.1000527

Tremblay, M.-È., Stevens, B., Sierra, A., Wake, H., Bessis, A., & Nimmerjahn, A. (2011). The role of microglia in the healthy brain. *The Journal of Neuroscience: The Official Journal of the Society for Neuroscience*, *31*(45), 16064–16069. https://doi.org/10.1523/JNEUROSCI.4158-11.2011

Vainchtein, I. D., & Molofsky, A. V. (2020). Astrocytes and Microglia: In Sickness and in Health. *Trends in Neurosciences*, *43*(3), 144–154. https://doi.org/10.1016/j.tins.2020.01.003

van Weering, H. R. J., Nijboer, T. W., Brummer, M. L., Boddeke, E. W. G. M., & Eggen, B. J. L. (2023). Microglia morphotyping in the adult mouse CNS using hierarchical clustering on principal components reveals regional heterogeneity but no sexual dimorphism. *Glia*. https://doi.org/10.1002/glia.24427

Vidal-Itriago, A., Radford, R. A. W., Aramideh, J. A., Maurel, C., Scherer, N. M., Don, E. K., Lee, A., Chung, R. S., Graeber, M. B., & Morsch, M. (2022). Microglia morphophysiological diversity and its implications for the CNS. *Frontiers in Immunology*, *13*, 997786. https://doi.org/10.3389/fimmu.2022.997786

Vykhodtseva, N., McDannold, N., & Hynynen, K. (2008). PROGRESS AND PROBLEMS IN THE APPLICATION OF FOCUSED ULTRASOUND FOR BLOOD-BRAIN

BARRIER DISRUPTION. *Ultrasonics*, *48*(4), 279–296. https://doi.org/10.1016/j.ultras.2008.04.004

Waldherr, S. (2018). Estimation methods for heterogeneous cell population models in systems biology. *Journal of the Royal Society Interface*, *15*(147), 20180530. https://doi.org/10.1098/rsif.2018.0530

Weber-Adrian, D., Thévenot, E., O'Reilly, M. A., Oakden, W., Akens, M. K., Ellens, N., Markham-Coultes, K., Burgess, A., Finkelstein, J., Yee, A. J. M., Whyne, C. M., Foust, K. D., Kaspar, B. K., Stanisz, G. J., Chopra, R., Hynynen, K., & Aubert, I. (2015). Gene delivery to the spinal cord using MRI-guided focused ultrasound. *Gene Therapy*, *22*(7), 568–577. https://doi.org/10.1038/gt.2015.25

Weinhard, L., di Bartolomei, G., Bolasco, G., Machado, P., Schieber, N. L., Neniskyte, U., Exiga, M., Vadisiute, A., Raggioli, A., Schertel, A., Schwab, Y., & Gross, C. T. (2018). Microglia remodel synapses by presynaptic trogocytosis and spine head filopodia induction. *Nature Communications*, *9*, 1228. https://doi.org/10.1038/s41467-018-03566-5

Wilkinson, K., & El Khoury, J. (2012). Microglial Scavenger Receptors and Their Roles in the Pathogenesis of Alzheimer's Disease. *International Journal of Alzheimer's Disease*, *2012*, 489456. https://doi.org/10.1155/2012/489456

Wilson, D. M., Cookson, M. R., Bosch, L. V. D., Zetterberg, H., Holtzman, D. M., & Dewachter, I. (2023). Hallmarks of neurodegenerative diseases. *Cell*, *186*(4), 693–714. https://doi.org/10.1016/j.cell.2022.12.032

Wu, D., Chen, Q., Chen, X., Han, F., Chen, Z., & Wang, Y. (2023). The blood–brain barrier: Structure, regulation, and drug delivery. *Signal Transduction and Targeted Therapy*, *8*(1), Article 1. https://doi.org/10.1038/s41392-023-01481-w

Xhima, K., Markham-Coultes, K., Hahn Kofoed, R., Saragovi, H. U., Hynynen, K., & Aubert, I. (2021). Ultrasound delivery of a TrkA agonist confers neuroprotection to Alzheimer-associated pathologies. *Brain*, *145*(8), 2806–2822. https://doi.org/10.1093/brain/awab460

Xia, F., Keep, R. F., Ye, F., Holste, K. G., Wan, S., Xi, G., & Hua, Y. (2022). The Fate of Erythrocytes after Cerebral Hemorrhage. *Translational Stroke Research*, *13*(5), 655–664. https://doi.org/10.1007/s12975-021-00980-8

Yoo, S.-S., Yoon, K., Croce, P., Cammalleri, A., Margolin, R. W., & Lee, W. (2018). Focused ultrasound brain stimulation to anesthetized rats induces long-term changes in somatosensory evoked potentials. *International Journal of Imaging Systems and Technology*, *28*(2), 106–112. https://doi.org/10.1002/ima.22262

Yoshino, S.-I., Fukushima, T., Hayashi, S., Nonaka, M., Ogawa, K., Sasaki, K., & Umemura, S.-I. (2009). Effects of Focused Ultrasound Sonodynamic Treatment on the Rat Blood-Brain Barrier. *Anticancer Research*, *29*(3), 889–895.

Yuan, T.-F., Liang, Y.-X., Peng, B., Lin, B., & So, K.-F. (2015). Local proliferation is the main source of rod microglia after optic nerve transection. *Scientific Reports*, *5*(1), Article 1. https://doi.org/10.1038/srep10788

Zanier, E. R., Fumagalli, S., Perego, C., Pischiutta, F., & De Simoni, M.-G. (2015). Shape descriptors of the "never resting" microglia in three different acute brain injury models in mice. *Intensive Care Medicine Experimental*, *3*(1), 7. https://doi.org/10.1186/s40635-015-0039-0

Zhang, Q., Chen, Y., Lai, M., Li, Y., Li, Q., Fu, C., Yao, Z., & Zhang, J. (2023). Magnetic Resonance Imaging-guided Focused Ultrasound Surgery in a Swine Adenomyosis Model. *Academic Radiology*. https://doi.org/10.1016/j.acra.2022.11.034

Zhang, Y., Wang, J., Ghobadi, S. N., Zhou, H., Huang, A., Gerosa, M., Hou, Q., Keunen, O., Golebiewska, A., Habte, F. G., Grant, G. A., Paulmurugan, R., Lee, K. S., & Wintermark, M. (2023). Molecular Identity Changes of Tumor-Associated Macrophages and Microglia After Magnetic Resonance Imaging-Guided Focused Ultrasound-Induced Blood-Brain Barrier Opening in a Mouse Glioblastoma Model. *Ultrasound in Medicine & Biology*, *49*(5), 1082–1090. https://doi.org/10.1016/j.ultrasmedbio.2022.12.006

Ziebell, J. M., Taylor, S. E., Cao, T., Harrison, J. L., & Lifshitz, J. (2012). Rod microglia: Elongation, alignment, and coupling to form trains across the somatosensory cortex after experimental diffuse brain injury. *Journal of Neuroinflammation*, *9*, 247. https://doi.org/10.1186/1742-2094-9-247